Doklady Physics, Vol. 48, No. 9, 2003, pp. 463–468. Translated from Doklady Akademii Nauk, Vol. 392, No. 1, 2003, pp. 31–37.
Original Russian Text Copyright © 2003 by Maĭer, Zabelok.

PHYSICS

Switching of Solitons in Tunnel-Coupled Optical Waveguides by a Weak Signal of a Different Frequency

A. A. Maĭer* and S. A. Zabelok

Presented by Academician K.A. Valiev December 27, 2002

Received January 20, 2003

The self-switching of unidirectional coupled shear waves was discovered in 1982 [1, 2], mathematically described in [3–6], and experimentally obtained first in [7, 8] and then in [9]. This phenomenon represents a sharp change in the ratio of the powers of these waves at the exit of the system, which is induced by a small change in the input power or phase of at least one of the waves [10, 11]. It can be also caused by a change in the power or phase of a weak optical signal at the entry of the system. In the latter case, optical pumping radiation of much higher power, along with the signal, is supplied to the entry. A new class of fully optical transistors was proposed on the basis of this phenomenon [1, 2]. Unidirectional coupled shear waves include the whole class of waves in optics, such as waves in tunnel-coupled optical waveguides, i.e., two parallel optical waveguides spaced by a short distance (usually from 1 to 10 μm), waves of different polarizations in an optical birefringent or magnetically active waveguide, waves under Bragg diffraction according to the Laue scheme, various modes in an optical waveguide, and waves of different frequency in a quadratically nonlinear crystal or optical waveguide [10, 11].

This phenomenon is of special practical importance for solitons used as unidirectional-coupled shear waves, because a soliton has the same phase over the entire time profile and therefore complete self-switching of its power is possible. This property is combined with the known possibility of transmission of solitons to large distances without distortion of their shape through fiber communication channels. The possibility of the switching of fundamental solitons in cubically nonlinear tunnel-coupled optical waveguides, when all waves have the same carrier frequency, was shown in [12]. The switching of orthogonally polarized fundamental solitons in a cubically nonlinear optical waveguide was analyzed in [13]. The possibility of the switching of solitons in quadratically nonlinear tunnel-coupled optical waveguides from one waveguide to another was demonstrated in [14].

In this work, we show the possibility of the fully optical switching of fundamental solitons in cubically nonlinear tunnel-coupled optical waveguides by a weak signal of a different carrier frequency from one waveguide to another. Such a different-frequency switching provides ultrafast, purely optical control by the flux of solitons (including their appearance in given time windows), which is very important for ultramodern soliton communication channels. It also allows the transformation (with high gain) of a weak modulation of signal pulses to strong modulation of a train of solitons at different desired carrier frequency. The amplitude of the signal is much lower than the amplitude of a soliton. Therefore, the modulation and control by the signal can be easily realized (even by means of electrooptics) with a much higher rate than the rate characteristic for ordinary control of a stream of solitons by electrooptical methods. Then, this very dense information from the signal wave (signal pulses) is automatically introduced to the soliton flux without loss in the speed of information transfer.

An important advantage of the different-frequency switching of solitons, which is considered in this work, over the same-frequency switching described previously in [12] is the elimination of the parasitic jitter effect and signal-phase drift, i.e., the elimination of the parasitic effect of both short-range and slow phase changes in the signal. Moreover, the effect of the input-soliton phase on the switching process is also excluded due to insensitivity of this switching to the input phase difference between the soliton and signal radiation.

If the carrier frequency of the signal differs significantly from the carrier frequency of the switched soliton, the group velocity and second-order dispersion of the signal pulse can differ substantially from the respective parameters of the switched soliton. For this reason, there is a natural question: Does optical switching occur in this case? If it does, is it stable under the deviation of the indicated signal parameters from the respective parameters of the soliton? This work gives positive answers to both questions.

General Physics Institute, Russian Academy of Sciences, ul. Vavilova 38, Moscow, 117942 Russia
** e-mail: maier@online.ru*

1028-3358/03/4809-0463$24.00 © 2003 MAIK “Nauka/Interperiodica”

We emphasize that the carrier frequency of signal pulses can differ significantly from the carrier frequency of solitons and can even be outside the region of the formation and propagation of solitons and/or transparency windows of a fiber light guide. This property enhances the practical value of this switching.

The electric field in a system of two cubically nonlinear tunnel-coupled optical waveguides can be represented in the form [15]

$$\mathbf{E} = \frac{1}{2}\sum_{j,k}\mathbf{e}_{jk}\tilde{A}_{jk}(z,t)E_{jk}(x,y) \times \exp\left(i\omega_j t + \frac{iz_a\beta_{jk}\omega_j}{c}\right) + \text{c.c.}, \qquad (1)$$

where β_{jk} is the effective index of refraction of the kth waveguide for the frequency ω_j, $\tilde{A}_{jk}(z,t)$ is the slowly varying amplitude of the wave in the kth waveguide for the frequency ω_j, $E_{jk}(x,y)$ is the transverse profile of the field in this waveguide, $\mathbf{e}_{jk}$ are the unit polarization vectors of the waves, z_a is the length-dimension (absolute) coordinate along the tunnel-coupled optical waveguides, $k = 0$ and 1 is the waveguide number, and $j = 1$ and 2 is the frequency number.

Let us substitute Eq. (1) into Maxwell's equations with allowance for cubic polarization, disregard the second derivatives with respect to the longitudinal coordinate, and consider transverse field profiles in waveguides as fixed. Equating coefficients of identical exponentials, we obtain the set of equations for electric fields corresponding to subscripts j and k. Multiplying both sides of each equation by $E^*_{jk}(x,y)$, integrating them over the cross-section, and going over to running time, we arrive at the following set of truncated equations for the amplitudes $A_{jk}(z,\tau)$, which describe in particular the interaction of the switched soliton at the carrier frequency ω_1 ($j = 1$) with the controlling signal pulse at the different carrier frequency ω_2 ($j = 2$) in tunnel-coupled optical waveguides with the numbers $k = 0$ and 1:

$$i\frac{\partial A_{10}}{\partial z} + i\upsilon_{10}\frac{\partial A_{10}}{\partial\tau} + D_{10}\frac{\partial^2 A_{10}}{\partial\tau^2} = -K_1A_{11}\exp(i\alpha_1 z) - \theta_{10}|A_{10}|^2A_{10} - 2\theta_{120}|A_{20}|^2A_{10}, \qquad (2.1)$$

$$i\frac{\partial A_{11}}{\partial z} + i\upsilon_{11}\frac{\partial A_{11}}{\partial\tau} + D_{11}\frac{\partial^2 A_{11}}{\partial\tau^2} = -K_1A_{10}\exp(-i\alpha_1 z) - \theta_{11}|A_{11}|^2A_{11} - 2\theta_{121}|A_{21}|^2A_{11}, \qquad (2.2)$$

$$i\frac{\partial A_{20}}{\partial z} + i\upsilon_{20}\frac{\partial A_{20}}{\partial\tau} + D_{20}\frac{\partial^2 A_{20}}{\partial\tau^2} = -fK_2A_{21}\exp(if\alpha_2 z) - f\theta_{20}|A_{20}|^2A_{20} - f2\theta_{210}|A_{10}|^2A_{20}, \qquad (2.3)$$

$$i\frac{\partial A_{21}}{\partial z} + i\upsilon_{21}\frac{\partial A_{21}}{\partial\tau} + D_{21}\frac{\partial^2 A_{21}}{\partial\tau^2} = -fK_2A_{21}\exp(-if\alpha_2 z) - f\theta_{21}|A_{21}|^2A_{21} - f2\theta_{211}|A_{11}|^2A_{21}. \qquad (2.4)$$

Here, K_j is the tunnel-coupling coefficient for the frequency ω_j, coefficients D_{jk} characterize the second-order dispersion and are inversely proportional to the dispersion length for the frequency ω_j, cubically nonlinear coefficients θ_{jk}, θ_{12k}, and θ_{21k} (proportional to convolutions of the cubic-nonlinearity tensor) determine the effect of the intensity of waves in the waveguide on the index of refraction of this waveguide and depend both on the nonlinearity of the waveguide material and on the transverse field profile in it [10, 11, 15], υ_{jk} are detunings of the group velocities, and $\alpha_j \backsim \beta_{j1} - \beta_{j0}$ is the differences of the effective indices of refractions of the waveguides for the frequency ω_j. Equations (2) are generalizations of equations from [15] to a dispersive medium.

The particular form of the coefficients in Eqs. (2) depends on the normalization. Taking into account the features of the problem under consideration, we take the soliton normalization of amplitudes for the frequency ω_1 such that $\theta_{10} = \theta_{11} = 1$, $D_{10} = D_{11} = 0.5$, $D_{2k} = 0.5\frac{l_{d1}}{l_{d2}} = 0.5\frac{\tilde{D}_{2k}\tau_{1\text{p}}^2}{\tilde{D}_{1k}\tau_{2\text{p}}^2}$. To this end, the coordinate along the tunnel-coupled optical waveguide is normalized by the dispersion length $l_{d1} = \frac{|D|}{\tau_\text{p}^2}$ for the frequency ω_1, i.e.,

$$z = \frac{z_a}{l_{d1}};\ D = \frac{\tilde{D}_{10} + \tilde{D}_{11}}{2},\ \tilde{D}_{jk} = \frac{\partial^2(\beta_{jk}\omega_j/c)}{\partial\omega_j^2};\ \tau = \frac{t - z_a/u}{\tau_\text{p}}$$

is the normalized running time; τ_p is the initial duration of the input pulse (soliton); $u = \frac{2u_{10}u_{11}}{u_{10} + u_{11}}$ is the average group velocity of pulses (solitons) in waveguides 0 and 1 for the frequency ω_1; $\upsilon_{jk} \approx \frac{1}{2}l_{d1}\tau_p^{-1}(u_{jk}^{-1} - u^{-1})$, $K_j = \frac{\tilde{K}_j \times 2\pi l_d}{\lambda\beta}$; $A_{jk} = \tilde{A}_{jk}\sqrt{\frac{\pi|\theta|\tau_\text{p}^2}{\lambda\beta D}}$, $\beta = \frac{1}{2}(\beta_{10} + \beta_{11})$, $\theta = \frac{1}{2}(\theta_{10} + \theta_{11})$; and the factor $f = \frac{\omega_2}{\omega_1}$ presents the difference between the carrier frequencies of the signal and solitons. Quantities with tilde are dimensional, i.e., unnormalized. We consider the most extensively used case of identical tunnel-coupled optical waveguides, i.e., $\alpha_j = 0$, $\upsilon_{1k} = 0$, $\theta_{j0} = \theta_{j1}$, and $\theta_{10} = \theta_{11} = \theta$.

We also assume that $\theta_{120} = \theta_{11} = \theta_{121} = \theta_{210} = \theta_{20} = \theta_{21} = 1$. As a rule, these relations can be at least approximately satisfied. For definiteness, the carrier frequency of the signal pulse is taken twice as high as the carrier frequency of the soliton, i.e., $f = 2$. In this case, since the field profiles for the signal frequency ω_2 overlap less with each other, the tunnel-coupling coefficient is much smaller than that for solitons. Specifically, we take the ratio $K_2 = 0.1K_1$ between these tunnel-coupling coefficients. Numerical experiments show that the results below hold qualitatively for other relations between frequencies of the signal and switched solitons (e.g., for the frequency ratio $f = 1.4/0.98$, important in practice), for different K_2/K_1 ratios, and for different relations between θ_{1k}, θ_{2k}, θ_{12k}, θ_{21k}.

The initial (input) conditions have the form

$$A_{10}(z = 0) \equiv A_{100}(t) = \frac{a_{10}\exp(i\varphi_{10})}{\cosh\tau}, \tag{3.1}$$

$$A_{11}(z = 0) \equiv A_{110}(t) = \frac{a_{11}\exp(i\varphi_{11})}{\cosh\tau}, \tag{3.2}$$

$$A_{20}(z = 0) \equiv A_{200}(t)$$
$$= a_{20}\exp(i\varphi_{20})\rho\left[\frac{\tau_{1p}}{\tau_{2p}}(\tau - \tau_d)\right], \tag{3.3}$$

$$A_{21}(z = 0) \equiv A_{210}(t)$$
$$= a_{21}\exp(i\varphi_{21})\rho\left[\frac{\tau_{1p}}{\tau_{2p}}(\tau - \tau_d)\right], \tag{3.4}$$

where τ_d is the shift of the maximum of the signal pulse from the maximum of the soliton.

We assume that $a_{2k}^2 \ll a_{1k}^2$ and take various shapes of the signal pulse $\rho(\tau - \tau_d)$, such as

$$\rho(\tau - \tau_d) = \frac{1}{\cosh(\tau - \tau_d)}, \tag{3.5.1}$$

$$\rho(\tau - \tau_d) = \exp\left[-\frac{(\tau - \tau_d)^{-2}}{2}\right]. \tag{3.5.2}$$

For simplicity, we consider signal pulses and solitons of the same duration; i.e., $\tau_{1p} = \tau_{2p} = \tau_p$. The results qualitatively hold for unequal durations. All fields at time infinity vanish; i.e., $|A_{jk}(z, \tau \to \pm\infty)| \to 0$.

Figures 1–4 illustrate the optical switching process.

Figure 1 shows pulses in tunnel-coupled optical waveguides: the switched soliton supplied to the entry of the zeroth waveguide and a very weak signal pulse, which is faintly visible and whose input power is approximately one hundredth of the input power of the soliton (signal pulses in Fig. 1 are multiplied by a factor of 50). Figures 1a and 1b show the switching of the soliton to the exits of the (point M_0) zeroth and (point M_1) first waveguides, respectively (see [3–8, 10–12] and Fig. 2). This switching is purely optical, because it is induced by the weak optical signal pulse supplied to the entry of either the zeroth (Fig. 1a) or first (Fig. 1b) waveguide.

According to our analysis, such a switching is highly stable to the detuning of the group velocities of the signal pulse and switched soliton (see Fig. 3), to the shift of the signal pulse maximum from the soliton maximum at the entry of tunnel-coupled optical waveguides (see Fig. 2), and to the deviation of the shape of the input signal pulse from soliton shape (3.5.1). However, switching proceeds most efficiently for a soliton shape (3.5.1) of the signal pulse. Figures 1–4 were obtained for this signal shape.

Moreover, switching is stable to the detuning of the second-order dispersion coefficients for different frequencies (Fig. 4): D_{20} and D_{21} can significantly differ from D_{10} and D_{11}, respectively. Stability of switching to the deviation of D_{20} and D_{21} from $D_{10} = D_{11} = 0.5$ is asymmetric as follows. In the region $D_{20} = D_{21} > 0.5$, switching holds and its depth decreases only by 5–10% with an increase in D_{20} and D_{21} even for $D_{20} = D_{21} = 10D_{10} = 10D_{11}$. In the region $D_{20} = D_{21} < 0.5$, the switching depth decreases much more strongly with a decrease in D_{20} and D_{21}.

Propagating through tunnel-coupled optical waveguides, the switched soliton virtually conserves its shape. Its amplitude even increases, while the signal pulse is slightly smeared and its amplitude decreases (Fig. 1). At the same time, most of the signal-pulse power is “attracted” to the switched soliton and propagates along with it; i.e., most of the energy of the weak signal pulse is captured by the switched soliton. Even if the maximum of the signal pulse is significantly shifted from the maximum of the introduced soliton by, e.g., $\tau_d = 3$, the power of the signal pulse “flows” to the soliton when pulses propagate through waveguides (Figs. 1c, 1d). Thus, the signal pulse is captured, and its shape as a result holds or almost holds in the waveguide to whose exit the soliton is switched (Fig. 1). However, for larger τ_d, the signal pulse loses its shape, smearing in time, and the depth of soliton switching decreases. For $\tau_d = 3$, the shape of the signal pulse at the exit of the first waveguide (under the soliton) becomes slightly asymmetric (Fig. 1c), while it is symmetric for $\tau_d = 0$. Unfortunately, the figure illustrating the case $\tau_d = 0$ cannot be presented in this short paper.

We think that this capture of the signal pulse is responsible for the high stability of switching to discrepancy (shift) between the maxima of the signal pulse and soliton in time, disagreement of group velocities, and difference in the second-order dispersion for the frequencies ω_1 and ω_2. Owing to capture, the signal pulse conserves sufficiently high power and accompa-

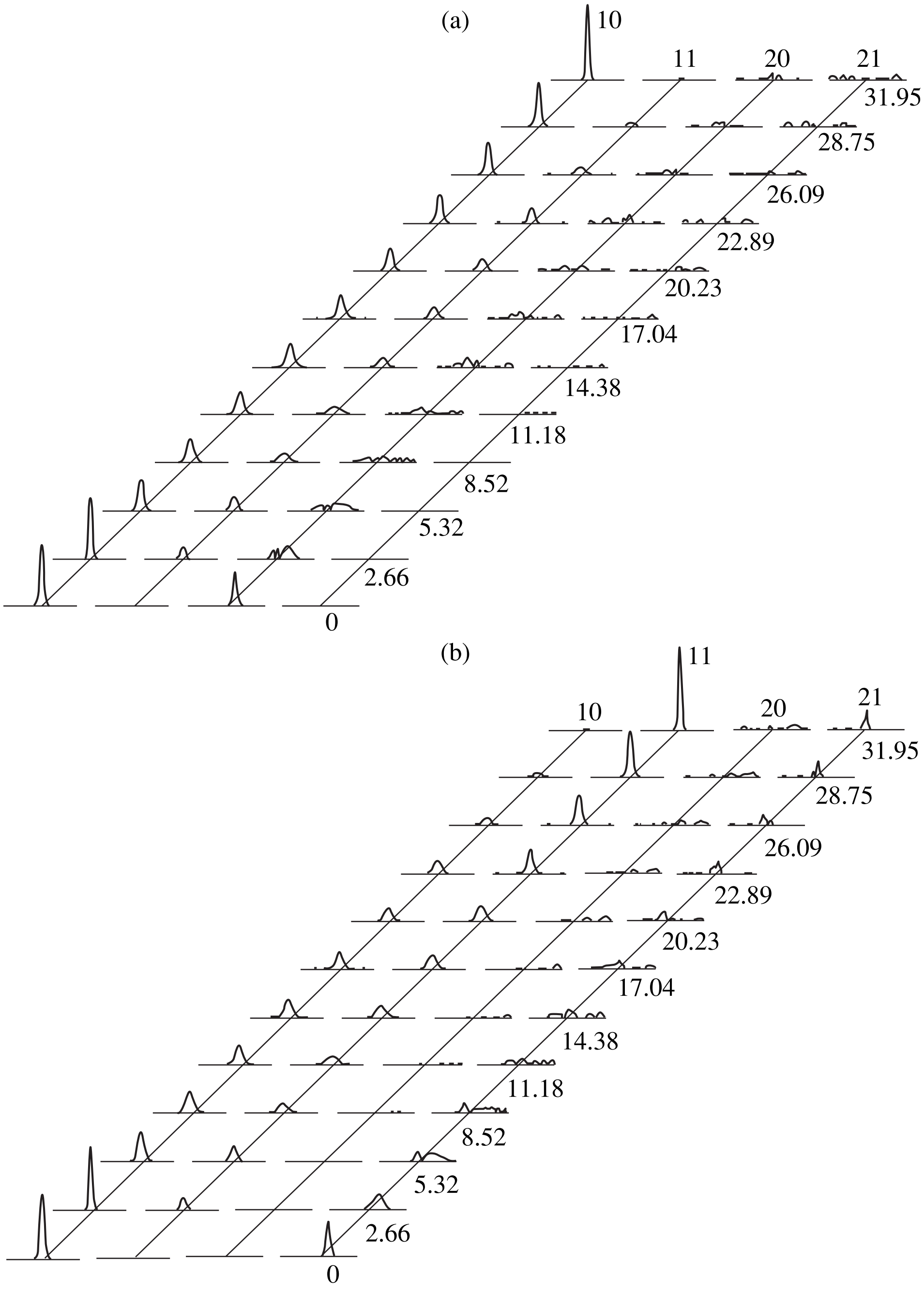

Fig. 1. Power time profiles $|A_{jk}(\tau)|^2$ of switchable soliton-like pulses at the frequency ω_1 ($j = 1$) and weak pulses of the control signal at the frequency ω_2 ($j = 2$) in the (a) zeroth and (b) first waveguides in cross-sections with various longitudinal coordinates z and in the (c) entry ($z = 0$) and exit (d) ($z = l = 31.95$) cross-sections, where the dashed lines are the power profile of the input soliton at the entry of the zeroth waveguide for $z = 0$; power profiles of all signal pulses are multiplied by a factor of 50; (e, f) energy of the switched solitons vs. the longitudinal coordinate z in the same waveguides. The parameters are a_{20} = (a) 0.12 and (b) 0, a_{21} = (a) 0 and (b) 0.12, $a_{10} = 1.15$, $a_{11} = 0$, $K_1 = 0.236175$, $K_2 = 0.0236175$, $\upsilon_{10} = \upsilon_{11} = 0$, $\upsilon_{20} = \upsilon_{21} = 0.2$, and $\tau_d = 3$.

nies the switched soliton on a sufficiently long path, which ensures the efficient switching even for large detuning indicated above. With an increase in the delay τ_d, the signal amplitude a_{21} necessary for achievement of the maximum switching depth increases (Fig. 2).

Figures 3 and 4 show the energy-transfer coefficient for solitons at the point M_1 of the switching curve (see [3–8, 10–12] and Fig. 2), when almost all the energy is switched to the exit of the first waveguide. Thus, Figs. 3 and 4 in fact characterize the depth of the optical switching of solitons. It decreases with an increase in the difference between both the group velocities of the signal pulse and switched soliton (Fig. 3) and the second-order dispersions of the signal

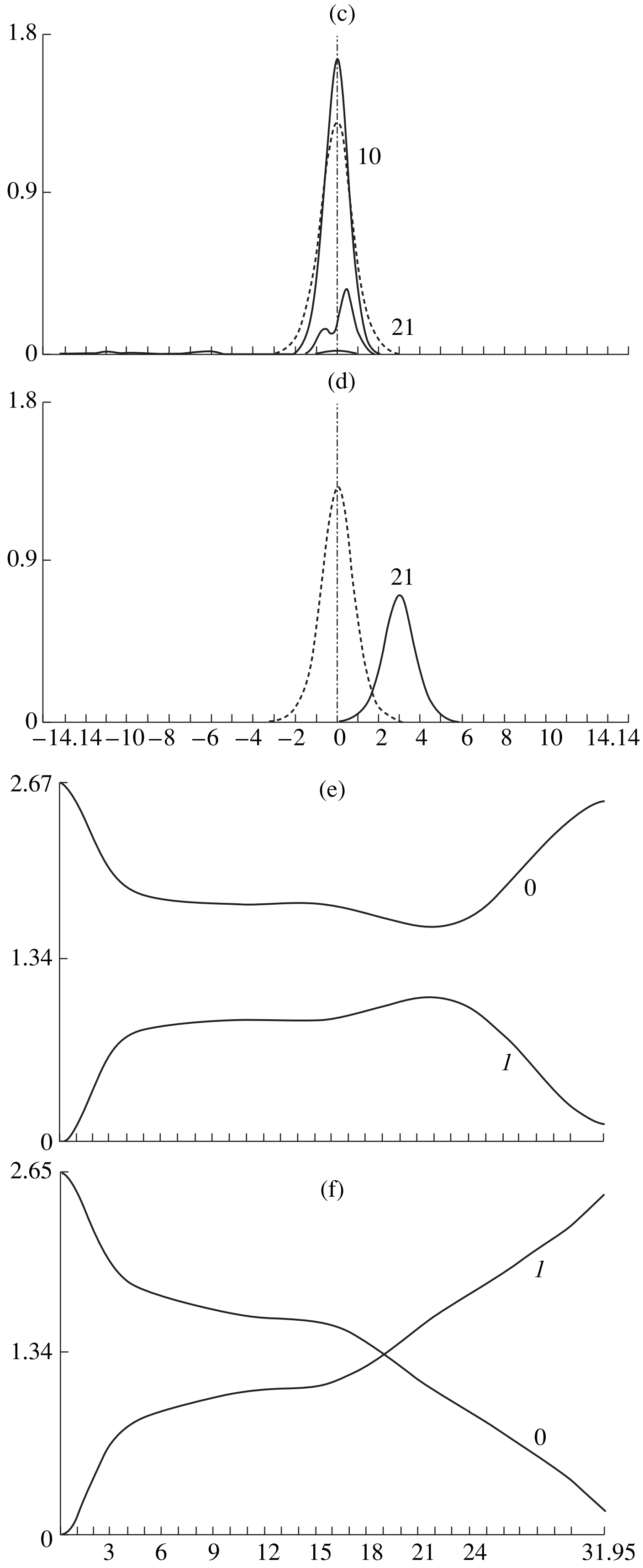
(c)
1.8
0.9
0
10
21
(d)
1.8
0.9
0
21
−14.14
−10
−8
−6
−4
−2
0
2
4
6
8
10
14.14
(e)
2.67
1.34
0
0
1
(f)
2.65
1.34
0
1
0
3
6
9
12
15
18
21
24
31.95

Fig. 1. (Contd.)

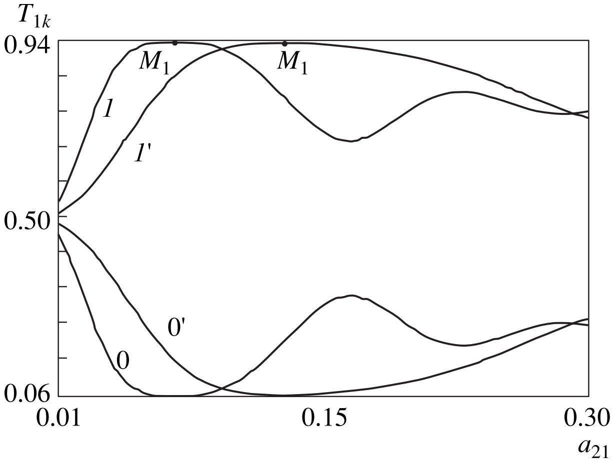

Fig. 2. Energy transfer coefficient T_{1k} for solitons vs. the signal pulse amplitude a_{21} for delay τ_d = (0, *1*) 0 and (0', *1'*); $\upsilon_{20} = \upsilon_{21} = \upsilon_{10} = \upsilon_{11} = 0$, and $D_{10} = D_{11} = D_{20} = D_{21} = 0.5$.

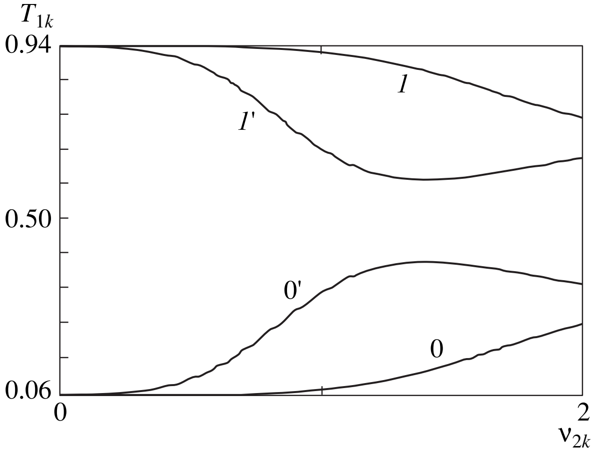

Fig. 3. Energy transfer coefficient T_{1k} for solitons at the frequency ω_1 vs. the detuning of the group velocities $\upsilon_{20} = \upsilon_{21}$ for $\upsilon_{10} = \upsilon_{11} = 0$, τ_d = (0, *1*) 0 and (0', *1'*) 3, and (at the point M_1) $a_{20} = 0$ and $a_{21} = 0.12$.

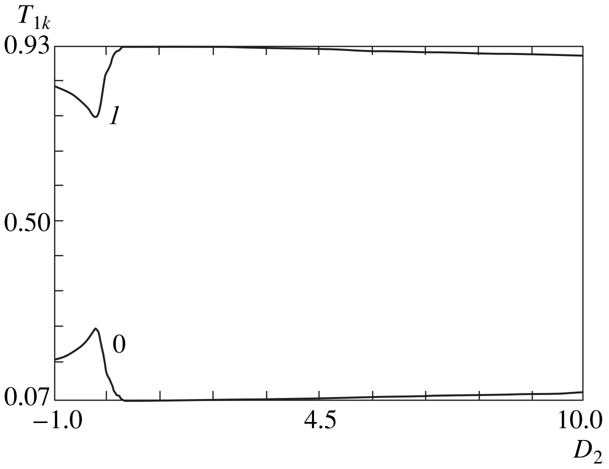

Fig. 4. Energy transfer coefficient T_{1k} for solitons at the frequency ω_1 vs. the second-order dispersion coefficient $D_{20} = D_{21} = D_2$ of the signal pulse for $\tau_d = 3$, and (at the point M_1) $a_{20} = 0$ and $a_{21} = 0.12$.

pulse and soliton (Fig. 4). In this case, the switching depth remains sufficiently high.

In numerical experiments, we check the conservation of both the energy integral and the integral

$$\int_{-\infty}^{\infty}\Bigg[\mathrm{Im}\bigg(f\nu_{10}A_{10}^*\frac{\partial A_{10}}{\partial t} + f\nu_{11}A_{11}^*\frac{\partial A_{11}}{\partial t} + \nu_{20}A_{20}^*\frac{\partial A_{20}}{\partial t} + \nu_{21}A_{21}^*\frac{\partial A_{21}}{\partial t}\bigg) + \bigg(fD_{10}\left|\frac{\partial A_{10}}{\partial t}\right|^2 + fD_{11}\left|\frac{\partial A_{11}}{\partial t}\right|^2 + D_{20}\left|\frac{\partial A_{20}}{\partial t}\right|^2 + D_{21}\left|\frac{\partial A_{21}}{\partial t}\right|^2\bigg) + f(\alpha_1|A_{11}|^2 + \alpha_2|A_{21}|^2) - \frac{f}{2}(\theta_{10}|A_{10}|^4 + \theta_{11}|A_{11}|^4 + \theta_{20}|A_{20}|^4 + \theta_{21}|A_{21}|^4) - f(\theta_{120}|A_{20}|^2|A_{10}|^2 + \theta_{121}|A_{21}|^2|A_{11}|^2) - f\,\mathrm{Re}(2K_1A_{10}A_{11}^* + 2K_2A_{20}A_{21}^*)\Bigg]dt = \mathrm{const}, \quad (4)$$

which is conserved if the equalities $\theta_{120} = \theta_{210}$ and $\theta_{121} = \theta_{211}$ are satisfied.

REFERENCES

1. A. A. Maĭer, Inventor’s Certificate USSR No. 1152397, Priority Sept. 22, 1982; Byull. Izobr., No. 46, 300 (1988).
2. A. A. Maĭer, Kvant. Élektron. **9** (11), 2296 (1982).
3. A. A. Maĭer, Kvant. Élektron. **11** (11), 157 (1984).
4. A. A. Maĭer, Izv. Akad. Nauk SSSR, Ser. Fiz. **48** (7), 1441 (1984).
5. A. A. Maĭer and K. Yu. Sitarskiĭ, Kvant. Élektron. **14** (11), 2369 (1987).
6. A. A. Maĭer and K. Yu. Sitarskiĭ, Dokl. Akad. Nauk SSSR **299** (6), 1387 (1988) [Sov. Phys. Dokl. **33** (2), 151 (1988)].
7. D. D. Gusovskiĭ, E. M. Dianov, A. A. Maĭer, *et al.*, Kvant. Élektron. **14** (6), 1144 (1987).
8. A. A. Maĭer, Yu. N. Serdyuchenko, K. Yu. Sitarskiĭ, *et al.*, Kvant. Élektron. **14** (6), 1157 (1987).
9. S. R. Friberg, A. M. Weiner, Y. Silberberg, *et al.*, Opt. Lett. **13**, 904 (1988).
10. A. A. Maĭer, Usp. Fiz. Nauk **165**, 1037 (1995) [Phys. Usp. **38**, 991 (1995)].
11. A. A. Maĭer, Usp. Fiz. Nauk **166**, 1171 (1996) [Phys. Usp. **39**, 1109 (1996)].
12. A. A. Maĭer and A. S. Lozinskiĭ, Dokl. Akad. Nauk **356**, 325 (1997) [Phys. Dokl. **42**, 483 (1997)].
13. A. A. Maĭer and A. S. Lozinskiĭ, Dokl. Akad. Nauk **358**, 470 (1998) [Dokl. Phys. **43**, 74 (1998)].
14. A. A. Maĭer and A. S. Lozinskiĭ, Dokl. Akad. Nauk **360**, 616 (1998) [Dokl. Phys. **43**, 333 (1998)].
15. A. A. Maĭer, Kvant. Élektron. **13** (7), 1360 (1986).

Translated by R. Tyapaev

Doklady Physics, Vol. 48, No. 9, 2003, pp. 469–473. Translated from Doklady Akademii Nauk, Vol. 392, No. 1, 2003, pp. 38–43.
Original Russian Text Copyright © 2003 by Urusov, Petrova, Eremin.

PHYSICS

Simulation of the Local Structure and Properties of the CaO–SrO and SrO–BaO Solid Solutions

Academician V. S. Urusov,* T. G. Petrova, and N. N. Eremin*****

Received March 13, 2003

As was mentioned in [1], phenomenological theory [2–4] has been used for a long time to calculate the thermodynamic functions of mixing and the stability limits of solid solutions extended in composition (continuous). According to this theory, the mixing enthalpy ΔH_{mix} of solid solutions such as MO–M'O with the NaCl-type structure can be determined by the formula

$$\Delta H_{\text{mix}} = \frac{9}{4}x_1x_2VK\left(\frac{\Delta R}{R}\right)^2 = \frac{1}{4}x_1x_2VK\left(\frac{\Delta V}{V}\right)^2. \quad (1)$$

Here, x_1 and x_2 are the molar fractions of the components; V is the molar volume; K is the compression modulus; $\Delta R = R_2 - R_1$ and $\Delta V = V_2 - V_1$ are the differences of the interatomic distances and molar volumes in the pure-component crystals, respectively; R is the average interatomic distance additively depending on the composition according to Vegard's rule

$$R = x_1R_1 + x_2R_2, \quad (2)$$

and V is the average molar volume satisfying the Retgers rule

$$V = x_1V_1 + x_2V_2. \quad (3)$$

In recent years, these characteristics have been intensively simulated on computers. Energy effects of mixing of high-concentration solid solutions are calculated both in the semiclassical approximation by minimizing energy found with semiempirical potentials of interatomic interaction and in various approximations of *ab initio* methods (Hartree–Fock method, density-functional theory). The first calculations of a semiclassical or atomistic type, along with *ab initio* calculations, were made for the intermediate compositions of solid solutions in the systems MnO–NiO, MgO–MnO, CaO–MnO [5], and CaO–MgO [6, 7]. Recently, we analyzed the latter system in detail [1]. The basic disadvantage of calculations of the structure and properties of oxide solid solutions by quantum mechanical methods and semiclassical method of interatomic potentials is the use of too small a cell (subcell) containing from 4 to 32 atoms. This disadvantage was overcome in [6, 7] (see also [8]).

The random distribution of atoms in the solid solution structure was simulated in [6] by the method of variation of clusters. Lavrentiev *et al.* [7] used the Exchange Bias Monte Carlo method, which made it possible to reduce the number of unsuccessful configurations in a 4 × 4 × 4 supercell containing 256 cations. Nevertheless, the method requires a long time for the computation of the stable configuration after 4×10^7 steps of variation in the atomic coordinates and cell sizes.

In [1], we used a large 4 × 4 × 4 supercell containing 256 cations of two types M and M' and estimated the short-range order degree for various configurations in the distribution of cations of different types. This enables us to find the properties of the disordered solid solution with the statistical distribution of cations over all structural positions. Here, we apply the same procedure to two other oxide systems with the NaCl-type structure to simulate the local structure and properties of mixing of the binary solid solutions CaO–SrO and SrO–BaO by the method of semiempirical pair potentials. These systems were previously considered in the phenomenological model [2, 8], studied experimentally both by calorimetry [9] and by measurement of the limits of the mixability of the components as functions of temperature [10, 11].

Following the method described in [1], short-range contributions to pair potentials were taken in the form of the algebraic sum of the Buckingham V_B and Morse V_M potentials given by Eqs. (4) and (5) in [1]. The energy minimum was sought by varying the atomic coordinates and lattice constants with using the GULP software package [13], which allows calculations of both the structural parameters and optimal interatomic potentials. The parameters of the Buckingham V_B and Morse V_M potentials were obtained by fitting the structure and properties of pure CaO, SrO, and BaO (Tables 1, 2) for the effective charges of cations and anions $zf = \pm 1.7$e, which corresponds to the ionic bond character $f = 0.85$. As in [1], this f value was found to provide the

---

Moscow State University, Vorob'evy gory, Moscow, 119899 Russia
* *e-mail: urusov@geol.msu.ru*
** *e-mail: t_petr@mail.ru*
*** *e-mail: neremin@mail.ru*

Table 1. Parameters for interatomic interaction potentials in CaO, SrO, and BaO crystals

Potential	λ, eV D, eV	ρ, Å β, Å^{-1}	C, eV Å^6 R_0, Å
V_B (Ca–O)	775.00	0.3437	0.000
V_M (Ca–O)	0.0515	2.27	2.5
V_B (Sr–O)	1002.20	0.3484	0.000
V_M (Sr–O)	0.014	2.87	2.6
V_B (Ba–O)	1477.39	0.3500	0.000
V_M (Ba–O)	0.0207	2.86	2.8

Table 2. Lattice constant a, unit-cell volume V, compression modulus K, and VK product for the pure CaO, SrO, and BaO crystals

Parameter	CaO		SrO		BaO	
	exp.	theor.	exp.	theor.	exp.	theor.
a, Å	4.810	4.810	5.114	5.114	5.522	5.522
K, GPa	115	115	87	88	71	74
V, cm^3/mol	16.76	16.75	20.45	20.45	25.35	25.35
VK, kJ/mol	1927	1927	1779	1800	1800	1876

best fit to the experimental data and testifies to a high ionic bond character in the oxides under consideration. We note that the potential for CaO was slightly modified compared to [1] to ensure virtually complete agreement with the experiment (Table 2).

According to our numerous computer experiments, it is virtually impossible to adequately approximate the statistical distribution of atoms replacing each other, which characterizes an ideal or regular solid solution, in $1 \times 1 \times 1$, $2 \times 2 \times 2$, and $3 \times 3 \times 3$ cells with small numbers of cation positions (4, 32, and 108, respectively). For this reason, as in [1], the structures and energy of solid solutions were calculated with the $4 \times 4 \times 4$ supercell with quadruple parameters of the NaCl-type structure, which consists of 512 atoms (256 cation positions). Restrictions due to symmetry were removed, because the formation of the solid solution accompanies by atomic displacements and corresponding distortion of the lattice constants. The properties of these displacements will be separately analyzed in this work.

The mixing enthalpy [ΔH_{mix}] is determined as

$$\Delta H_{\text{mix}} = U_{\text{ss}}(x) - xU_1 - (1-x)U_2, \tag{4}$$

where x is the molar fraction of the pure second component (CaO and SrO for the cases under consideration), and U_1 and U_2 are the structure energies of the pure first and second components of the mixture, respectively. The ΔH_{mix} values were obtained for three compositions $x = 0.25$, 0.5, and 0.75 by extrapolating $\Delta H_{\text{mix}}(\sigma)$ calculated for several tens of atomic configurations to the zero Bragg–Williams short-range order parameter

$$\sigma = \frac{\bar{q} - q_{\min}}{q_{\max} - q_{\min}}. \tag{5}$$

Here, $\bar{q}$ is the ratio of the number of the second neighbors of different types M–M' to the total number of cation pairs in the second coordination sphere as averaged for all 256 cations of the structure, $q_{\min}$ corresponds to the disordered solid solution with the minimum number of such pairs and is proportional to the double product of the concentrations of pure components $2x(1-x)$, and $q_{\max}$ is the maximally ordered solid solution corresponding to the hypothetical superstructures for $x/(1-x) = 1.0$, 0.25, and 0.75 (compositions 1:1, 1:3, and 3:1, respectively). Superstructures are chosen and the $q_{\max}$ value is estimated similarly to [1].

The energies ΔH_{mix} of the formation of the solid solution depend almost linearly on the short-range order degree σ for all three compositions. Therefore, $\Delta H_{\text{mix}}(\sigma)$ values can be linearly extrapolated to $\sigma = 0$ by the least squares method. These linear dependences for the two systems under consideration are not shown here, because similar dependences of the CaO–MgO system were presented in Fig. 1 in [1].

Moreover, ΔH_{mix} values can be found by seeking an almost random distribution of cations with the use of a random-number generator. Both the above approaches give close results. However, we preferred the latter method.

Figure 1 shows the ΔH_{mix} values obtained in our work and values calculated by Eq. (1) with the average value $VK_{\text{av}} = 1900(40)$ kJ/mol (see Table 2). In addition, Fig. 1 shows calorimetric data [9], which, within the large standard deviations presented in [9], agree satisfactorily with theoretical models.

Simulated ΔH_{mix} values exhibit asymmetry with respect to the axis of the compositions and can be represented analytically in the two-parameter form

$$\Delta H_{\text{mix}}(\text{CaO–SrO}) = x(1-x)[xW_1 + (1-x)W_2]$$
$$= x(1-x)[29.3x + 20.2(1-x)],$$
$$\Delta H_{\text{mix}}(\text{SrO–BaO}) = x(1-x)[xW_1 + (1-x)W_2]$$
$$= x(1-x)[45.8x + 23.6(1-x)].$$

Here, W_1 and W_2 are the Margules parameters for the mixing enthalpy (measured in kJ mol^{-1}) and x is the molar fraction of the first component in both systems.

These equations can be compared with empirical data obtained from measurements of the stability (decay) regions of the same solutions in [10, 11]:

$$\Delta H_{\text{mix}}(\text{CaO–SrO}) = x(1-x)[27.0x + 25.0(1-x)],$$
$$\Delta H_{\text{mix}}(\text{SrO–BaO}) = x(1-x)[33.4x + 29.3(1-x)].$$

Comparison of the respective Margules parameters shows that the computer simulation leads to a higher

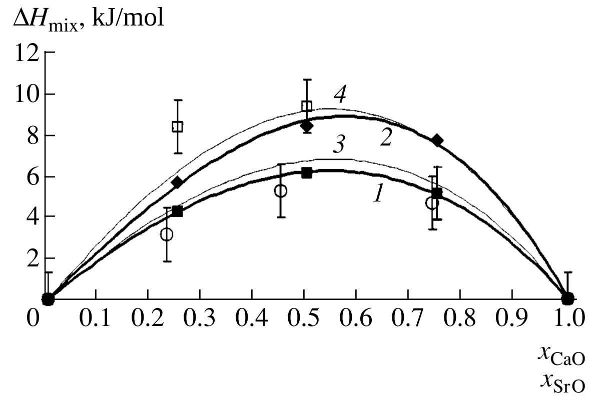

Fig. 1. Enthalpy of the formation of the CaO–SrO and SrO–BaO solid solutions vs. the composition. Thick and thin lines are computer simulation and calculation by Eq. (1), respectively. The upper and lower lines correspond to the (closed rhombs) SrO–BaO and (closed squares) CaO–SrO systems, respectively. The open circles and squares with estimated error bars are experimental data for the CaO–SrO and SrO–BaO systems, respectively.

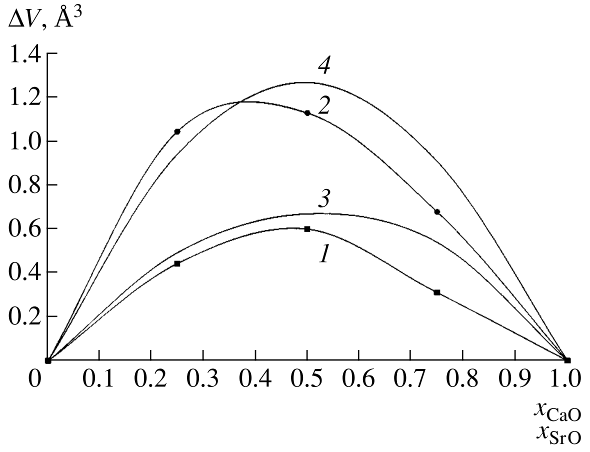

Fig. 2. Deviation of the unit-cell volume V from additivity. Lines *1* and *2* are computer simulation, while lines *3* and *4* are phenomenological calculation for a positive deviation form Vegard's rule (2) for the CaO–SrO and SrO–BaO systems, respectively.

asymmetry in mixing enthalpy, particularly for the SrO–BaO system.

In [1], computer simulation was applied for the first time to find the properties of a nonideal solid solution such as the deviation of the volume from Retgers rule (3) and compression modulus K from additivity for the CaO–MgO system taken as an example. Figures 2 and 3 show the functions $\Delta V_{mix}(x)$ and $\Delta K(x)$ for the two new systems CaO–SrO and SrO–BaO. As is seen in Fig. 2, the calculated $\Delta V_{mix}(x)$ values exhibit significantly smaller positive deviations from additivity than those obtained in phenomenological theory [Eq. (10) from [1]]. Measurements of the lattice constants for the CaO–SrO system [10] with an accuracy of 0.0001 Å correspond to a linear dependence on the composition; i.e., they satisfy Vegard's rule (2). This corresponds to a small negative deviation of the unit-cell volume from additivity, i.e., from Retgers rule (3):

$$\Delta V_{mix}(\text{CaO–SrO}) = -x(1-x)(a + a_1 + a_2)(\Delta a)^2,$$

where, $a = xa_1 + (1-x)a_2$ and $\Delta a = a_2 - a_1$. This formula yields –0.35 A^3 for the maximum ΔV_{mix} value for $x = 0.5$.

The lattice constants measured for the SrO–BaO system [11] with the same accuracy exhibit small positive deviation from Vegard's rule. Jacob and Varghese [11] considered that this deviation corresponds to Retgers rule (3) within experimental errors.

Figure 3 shows negative deviations of the compression modulus $\Delta K(x)$ from additivity for both systems in qualitative agreement with predictions of phenomenological model [Eqs. (11), (12) in [1]]. However, computer simulation implies that deviations can be much larger, particularly for compositions where the smaller component of the system prevails.

Information about the local structure of solid solutions can be obtained by calculating their various atomic configurations and compositions. Figure 4 shows the distributions of the M–O and M'–O distances, as well as the distances between oxygen atoms in linear O–M(M')–O chains and between metal atoms in linear M(M')–O–M(M') chains in the CaO–SrO system for the composition $x = 0.5$ and order degree $\sigma = 0.03$, i.e., in the almost fully disordered solid solution of the middle composition. It is seen that there are three most probable M–O distances corresponding to half the distances in Ca–O–Ca linear chains with a maximum at 2.425 Å, in Sr–O–Sr chains with a maximum at 2.540 Å, and in mixed Sr–O–Ca configurations with a double maximum around 2.48 Å. The last value is close to an average interatomic distance of 2.481 Å in the

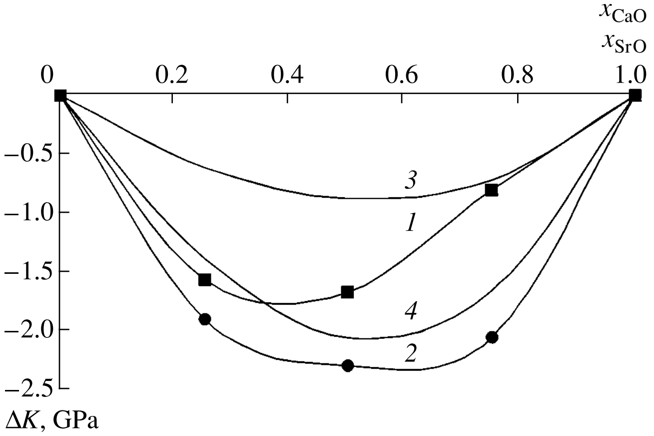

Fig. 3. Deviation of the compression modulus K from additivity. Lines *1* and *2* are computer simulation, while lines *3* and *4* are phenomenological calculation for the CaO–SrO and SrO–BaO systems, respectively.

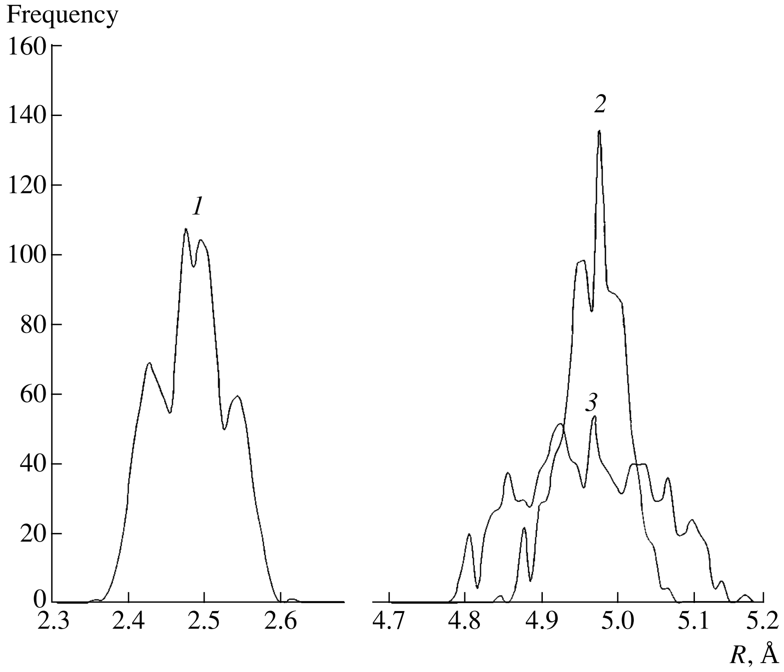

Fig. 4. Distribution of the (*1*) M–O, (*2*) M–M', and (*3*) O–O distances in the linear bond chains for the stoichiometric composition of the CaO–SrO system with an almost random distribution of cations over the sites of the solid solution structure.

$Ca_{0.5}Sr_{0.5}O$ solid solution. The Ca–O distance in Ca–O–Ca atomic triples is longer than the corresponding distance in pure CaO (2.405 Å) by 0.02 Å. The Sr–O distance in the Sr–O–Sr atomic triples is shorter than the corresponding distance in pure SrCaO (2.557 Å) by about the same value. These differences are most simply attributed to the superposition of neighboring peaks in the frequency diagram (line *1* in Fig. 4). However, they probably also indicate the general relaxation of the cation sublattice, which shortens all different distances.

The double middle peak in this diagram is most interesting. The maximum at the shortest distance 2.475 Å obviously corresponds to Ca–O distances in mixed atomic triples. The maximum at a distance of 2.495 Å corresponds to Sr–O distances in such linear chains. The first distance is longer than the distance in pure CaO by 0.07 Å, while the second distance is shorter than the distance in pure SrO by 0.06 Å. The phenomenological model [2–4] and Distance Least Squares method (fitting of distances by the least squares method) [14] predict that the bond lengths in the NaCl-like structure change by $\pm\Delta R/2$, where ΔR is the difference between interatomic distances in the pure components. This behavior corresponds to the structure-relaxation degree $\lambda = 0.5$ or, in terms of [14], the compliance factor $c_s = 1 - \lambda = 0.5$. For the system under consideration, the corresponding distances must change by ±0.076 Å, which is slightly larger than the change in both distances. This discrepancy can be partially attributed to the shift of maxima due to the superposition of all four peaks. Moreover, this discrepancy can testify to a lower relaxation degree of the solid solution than that expected in simpler models. These results can be compared with the EXAFS experimental data for acid–halide solid solutions with the NaCl-type structure [15], which also provide slightly smaller changes in the bond lengths in mixed configurations than those predicted in simple models. In particular, the changes measured in distances for (K, Rb)Br correspond to $\lambda = 0.45$.

Lines *2* and *3* in Fig. 4 are the distributions of the interatomic distances in the M–O–M' and O–M(M')–O linear chains. As is seen, the distribution in the metal sublattice contains three peaks. The highest middle peak is close to 4.97 Å, i.e., to the average cubic lattice constant. It is reasonable to attribute it to distances in mixed chains Ca–O–Sr (and Sr–O–Ca). Two lower side peaks are spaced from the middle peak by 0.02–0.03 Å to the right and left and can be attributed to the CA–O–Ca and Sr–O–Sr distances, respectively. The distribution of distances in the metal sublattice is generally characterized by a relatively low standard deviation (0.04 Å at half maximum).

In contrast, the distribution of the O–M–O distances in the oxygen sublattice (line *3* in Fig. 4) has at least triple standard deviation and complex structure. This distribution involves at least ten peaks, which can be identified with high probability by comparing with the geometric model of the displacement of the general atom from its standard position in solid solutions of the NaCl-like structure [2–4]. In this model, oxygen atoms displace from their standard positions at the centers of octahedrons by 0 (0.125), $\Delta R/2$ (0.375), $\sqrt{2}\left(\frac{\Delta R}{2}\right)$

(0.375), and $\sqrt{3}\left(\frac{\Delta R}{2}\right)$ (0.125) for various configurations of their mixed cation environment. The numbers in the parentheses are the probabilities of the respective displacements for the average composition of the disordered mixture.

Distribution *3* in Fig. 4 demonstrates that many distances between O atoms are close to the average lattice constant of the solid solution. Such distances always appear when either O atoms common to neighboring cation octahedrons do not displace from their standard positions or their displacements caused by neighboring cations have the same signs. The total probability of the appearance of such distances is equal to $2(0.125)^2 + 2(0.375)^2 = 0.312$. On the other hand, short and long O–M–O distances appear when both displacements $\sqrt{3}\frac{\Delta R}{2}$ are opposite and directed toward and outward the intermediate cation M, respectively. The probabilities of such displacements in the disordered mixture are proportional to $(0.125)^2 = 0.015$, and the full width of the distribution of the O–O distances must be close to $4\sqrt{3}\frac{\Delta R}{2}$. For the CaO–SrO system, this quantity must be equal to about 0.53 Å. The computer experiment yields a value of about 0.43 Å for the distribution width. Thus, the full width of the distribution of O–O distances is not apparently manifested in the diagram due to a low probability of the maximum displacements. The displacements in opposite directions with magnitudes $4\sqrt{2}\frac{\Delta R}{2} = 0.43$ Å, $2\sqrt{2}\frac{\Delta R}{2} + 2\frac{\Delta R}{2} = 0.37$ Å, and $4\frac{\Delta R}{2} = 0.30$ Å have a much higher identical probability of $(0.375)^2 = 0.141$. They are responsible for the visible width of the interatomic-distance distribution band in the oxygen sublattice and principal three peaks in the diagram. Other peaks within the band have lower probabilities (from 0.015 to 0.047) and are not pronounced. Thus, models agree quite well with each other, while the computer simulation provides much more detailed pattern of the atomic-displacement distribution.

ACKNOWLEDGMENTS

This work was supported by the Russian Foundation for Basic Research (project nos. 00-15–98582 and 99-05–65139) and INTAS (grant no. 97-32174). The work of N.N.E. was supported by the Foundation for Assistance to Russian Science.

REFERENCES

1. V. S. Urusov, T. G. Petrova, and N. N. Eremin, Dokl. Akad. Nauk **387**, 191 (2002) [Dokl. Phys. **47**, 811 (2002)].
2. V. S. Urusov, *Theory of Isomorphic Mixability* (Nauka, Moscow, 1977).
3. V. S. Urusov, V. L. Tauson, and V. V. Akimov, *Geochemistry of Solids* (GEOS, Moscow, 1997).
4. V. S. Urusov, in *Solid Solution in Oxides and Silicates. EMU Notes* (Eötvös Univ. Press, Budapest, 2001), Vol. 3, pp. 121–153.
5. M. Königstein, F. Kora, and C. R. A. Catlow, J. Solid State Chem. **37**, 261 (1998).
6. P. D. Tepesh, A. F. Kohan, G. D. Garbulsky, *et al.*, J. Am. Ceram. Soc. **79**, 2033 (1996).
7. M. Yu. Lavrentiev, N. L. Allan, G. D. Barrera, and J. A. Purton, J. Phys. Chem. B **105**, 3594 (2001).
8. V. S. Urusov, J. Solid State Chem. **153**, 357 (2001).
9. G. V. Flidlider, P. V. Kovtunenko, E. V. Kiseleva, and A. A. Bundel’, Zh. Fiz. Khim. **40**, 2474 (1966).
10. K. T. Jacob and Y. Waseda, J. Am. Ceram. Soc. **81**, 1065 (1998).
11. K. T. Jacob and V. Varghese, J. Mater. Chem. **5**, 1059 (1995).
12. V. S. Urusov and Dubrovinskiĭ, *Computer Simulation of the Structural Properties of Minerals* (Mosk. Gos. Univ., Moscow, 1989).
13. J. D. Gale, *GULP-User Manual* (R. Inst. and Imper. College, London, 1997).
14. W. A. Dollase, Phys. Chem. Miner. **6**, 295 (1980).
15. J. B. Boyce and J. C. Mikkelsen, Phys. Rev. B: Condens. Matter **31**, 6903 (1985).

Translated by R. Tyapaev

Doklady Physics, Vol. 48, No. 9, 2003, pp. 474–477. Translated from Doklady Akademii Nauk, Vol. 392, No. 1, 2003, pp. 44–47.
Original Russian Text Copyright © 2003 by Yalamov, Kuz'min.

PHYSICS

Effect of Kinetic Boundary Conditions on Unsteady Growth and Evaporation of Drops

Yu. I. Yalamov and M. K. Kuz'min

Presented by Academician R.F. Ganiev February 12, 2003

Received February 17, 2003

The phenomenon of evaporation and growth of liquid drops in a gaseous phase is important for processes occurring in nature and for vital human activities. Therefore, it has been extensively studied [1–3]. As was noted in [1], this phenomenon is very complex under real conditions, and its theory is complicated. For this reason, Fuks [1] suggested constructing this theory with a number of simplifying assumptions: one should start with an extremely idealized model and then correct the corresponding equations by taking into account different factors that have not been considered. In addition, he proposed considering the quasisteady regime of both evaporation of drops and heat transfer to them as a basis. Some papers published after review [1] (see, e.g., [4–6]) show the drawbacks of quasisteady solutions. Unfortunately, the inclusion of unsteady processes is not sufficiently advanced in this field of research, and there is a deficiency of experimental data concerning this problem (as was pointed out in [1]).

Both the evaporation and condensation-caused growth of a sufficiently large stationary drop occur mainly due to two oppositely directed transfer processes. These are vapor diffusion and heat conduction initiated by latent heat of vaporization or condensation. Therefore, only simultaneous consideration of the two mentioned unsteady processes provides more accurate description of the phenomenon under investigation (see [6–8]). These two transfer processes are coupled through boundary conditions. Therefore, the boundary conditions on the drop–environment interface must be correctly formulated; i.e., the effect of the Knudsen layer must be properly taken into account. The last problem has been investigated rather intensively during the last 30 years, but only for the quasisteady regime (see [2, 3] and references therein).

In this paper, simultaneously considering time-dependent equations of diffusion and heat conduction, we specify the gas-kinetic boundary conditions that are obtained by using mathematical methods of the kinetic theory of gases and include the jumps of concentration and temperature in the Knudsen layer [2]. We derive both the general expression for the concentration distribution and equations for temperature fields on the drop surface and in the surrounding medium. In addition, an expression for the rate of change in the drop radius at any time is derived and the ranges of applicability of some of the results obtained in the preceding theories are established.

In the case under consideration, the distribution of the relative concentration c_1 and the temperature T of the vapor–gas mixture are described by the system of equations (1) and (2) with initial and boundary conditions (3)–(7):

$$\frac{\partial c_1}{\partial t} = D\left(\frac{\partial^2 c_1}{\partial r^2} + \frac{2}{r}\frac{\partial c_1}{\partial r}\right), \tag{1}$$

$$\frac{\partial T}{\partial t} = a\left(\frac{\partial^2 T}{\partial r^2} + \frac{2}{r}\frac{\partial T}{\partial r}\right), \tag{2}$$

$$c_1(r, t)\big|_{t=0} = c_{1\infty}, \quad c_1(r, t)\big|_{r \to +\infty} = c_{1\infty}, \tag{3}$$

$$T(r, t)\big|_{t=0} = T_\infty, \quad T(r, t)\big|_{r \to +\infty} = T_\infty, \tag{4}$$

$$[c_1(r, t) - c_{1R}]\big|_{r=R} = \left(K_c^{(c)}\frac{\partial c_1}{\partial r} + K_c^{(T)}\frac{1}{T_\infty}\frac{\partial T}{\partial r}\right)\Bigg|_{r=R}, \tag{5}$$

$$[T(r, t) - T_R]\big|_{r=R} = \left(K_T^{(T)}\frac{\partial T}{\partial r} + K_T^{(c)}T_\infty\frac{\partial c_1}{\partial r}\right)\Bigg|_{r=R}, \tag{6}$$

$$Lnm_1 D\frac{\partial c_1}{\partial r}\bigg|_{r=R} = -\kappa\frac{\partial T}{\partial r}\bigg|_{r=R}. \tag{7}$$

Here, D is the coefficient of the diffusion of the vapor in a gas not condensing into the liquid phase; a and κ are the thermal diffusivity and the thermal conductivity of the vapor–gas mixture, respectively;

$$c_{1R} = c_1(T_R) = \frac{n_1(T_R)}{n};$$

$n_1(T_R)$ is the concentration of the saturated vapor of the drop substance at the temperature $T_R = T_R(t)$ on the

---

Moscow State Regional University, ul. Radio 10a, Moscow, 105007 Russia

drop surface; $n = n_1 + n_2$, where n_1 and n_2 are the concentrations of molecules of the first and second components, respectively; L is the heat of the phase transition; m_1 is the molecular mass of the volatile (first) component; R is the drop radius; r is the radial coordinate in the spherical coordinate system with the origin at the drop center; t is the time; and $K_c^{(c)}$, $K_c^{(T)}$, $K_T^{(T)}$, and $K_T^{(c)}$ are the gas-kinetic coefficients of the jumps of concentration and temperature.

To solve the problem, we use the Laplace transforms [9] and introduce the notation

$$S(r, p) = \int_0^\infty c_1(r, t)e^{-pt}dt, \tag{8}$$

$$\theta(r, p) = \int_0^\infty T(r, t)e^{-pt}dt. \tag{9}$$

Using initial conditions (3) and (4), we arrive at the following transforms of Eqs. (1) and (2):

$$DS'' + \frac{2D}{r}S' - pS + c_{1\infty} = 0,$$

$$a\theta'' + \frac{2a}{r}\theta' - p\theta + T_\infty = 0.$$

These are ordinary differential equations for the unknown functions $S(r, p)$ and $\theta(r, p)$, where r is the independent variable and p is the parameter. Solving these linear equations with variable coefficients with allowance for boundary conditions (3) and (4), we obtain

$$S(r, p) = \frac{c_{1\infty}}{p} + \frac{A}{r}\exp\left(-\sqrt{\frac{p}{D}}r\right), \tag{10}$$

$$\theta(r, p) = \frac{T_\infty}{p} + \frac{B}{r}\exp\left(-\sqrt{\frac{p}{a}}r\right), \tag{11}$$

where A and B are the integration constants. To write the Laplace transforms of the boundary conditions specified by Eqs. (5)–(7), we introduce the notation

$$\theta_R(p) = \int_0^\infty T_R(t)e^{-pt}dt. \tag{12}$$

This leads to the following system of algebraic equations for the unknowns A, B, and C:

$$\begin{gathered}(1 + K_c^{(c)}p_1)q_1A + \frac{K_c^{(T)}}{T_\infty}p_2q_2B = c_{1p}R,\\ K_c^{(c)}T_\infty p_1q_1A + (1 + K_T^{(T)}p_2)q_2B - RC = 0,\\ lp_1q_1A + \kappa p_2q_2B = 0,\end{gathered} \tag{13}$$

where

$$C = \theta_R(p) - \frac{T_\infty}{p}, \quad c_{1p} = \frac{c_{1R} - c_{1\infty}}{p},$$

$$p_1 = \frac{1}{R} + \sqrt{\frac{p}{D}}, \quad p_2 = \frac{1}{R} + \sqrt{\frac{p}{a}},$$

$$q_1 = \exp\left(-\sqrt{\frac{p}{D}}R\right), \; q_2 = \exp\left(-\sqrt{\frac{p}{a}}R\right), \; l = Lnm_1D.$$

Using the solution of system (13), we obtain the following expressions for functions (10), (11), and (12):

$$S(r, p) = \frac{c_{1\infty}}{p} + \frac{(c_{1R} - c_{1\infty})R\sqrt{D}}{\chi_c r}\frac{e^{-\alpha_c\sqrt{p}}}{p(\sqrt{p} + \beta)}, \tag{14}$$

$$\theta(r, p) = \frac{T_\infty}{p} + \frac{\eta R\sqrt{a}}{\chi_c r}\frac{\sqrt{p} + \frac{\sqrt{D}}{R}}{p(p + b_1\sqrt{p} + b_2)}e^{-\alpha_T\sqrt{p}}, \tag{15}$$

$$\theta_R(p) = \frac{T_\infty}{p} + \frac{\eta\chi_T}{\chi_c}\frac{p + a_1\sqrt{p} + a_2}{p(p + b_1\sqrt{p} + b_2)}, \tag{16}$$

respectively. Here,

$$\alpha_c = \frac{r - R}{\sqrt{D}}, \quad \beta = \frac{(R + \chi_c)\sqrt{D}}{\chi_c R}, \quad \alpha_T = \frac{r - R}{\sqrt{a}},$$

$$\eta = \frac{(c_{1\infty} - c_{1R})l}{\kappa},$$

$$a_1 = \frac{\chi_T\sqrt{D} + (R + \chi_T)\sqrt{a}}{\chi_T R}, \quad a_2 = \frac{(R + \chi_T)\sqrt{Da}}{\chi_T R^2},$$

$$b_1 = \frac{(R + \chi_c)\sqrt{D} + \chi_c\sqrt{a}}{\chi_c R}, \quad b_2 = \frac{(R + \chi_c)\sqrt{Da}}{\chi_c R^2};$$

while

$$\chi_c = K_c^{(c)} - \frac{l}{\kappa T_\infty}K_c^{(T)}, \quad \chi_T = K_T^{(T)} - \frac{\kappa T_\infty}{l}K_T^{(c)}$$

are the nonnegative composite coefficients of the jumps in concentration and temperature, respectively.

The inverse transforms are represented with the use of the functions

$$\varphi(\alpha, \beta, t) = e^{\beta^2 t + \alpha\beta}\operatorname{erfc}\left(\frac{\alpha}{2\sqrt{t}} + \beta\sqrt{t}\right),$$

$$\varphi(\beta, t) = \varphi(0, \beta, t),$$

$$\Phi(\alpha, \beta, t) = \operatorname{erfc}\left(\frac{\alpha}{2\sqrt{t}}\right) - \varphi(\alpha, \beta, t),$$

$$\Phi(\beta, t) = \Phi(0, \beta, t).$$

Then, in view of Eq. (8), the inverse transform of Eq. (14) yields the distribution of the relative concentration in the drop environment in the form

$$c_1(r, t) = c_{1\infty} + \frac{(c_{1R} - c_{1\infty})R^2}{(R + \chi_c)r}\Phi(\alpha_c, \beta, t). \qquad (17)$$

Calculating the inverse transforms of Eqs. (15) and (16), one should take into account that the roots z_1 and z_2 of the square trinomial $z^2 + b_1 z + b_2$ are real and differ from each other when

$$\Delta_b = (R + \chi_c)\sqrt{D} - \chi_c\sqrt{a} \neq 0,$$

or coincide with each other when $\Delta_b = 0$. If $\Delta_b \neq 0$, then, in view of Eqs. (9) and (12), the inverse transforms of Eqs. (15) and (16) are the functions

$$T(r, t) = T_\infty + \frac{\eta R\sqrt{a}}{\chi_c r}\sum_{j=1}^{2}\frac{B_j}{\beta_j}\Phi(\alpha_T, \beta_j, t), \qquad (18)$$

$$T_R(t) = T_\infty + \frac{\eta\chi_T}{\chi_c}\left[1 + \sum_{j=1}^{2}\frac{C_j}{\beta_j}\Phi(\beta_j, t)\right], \qquad (19)$$

describing temperature fields in the environment of the drop and on its surface, respectively. Here,

$$\beta_1 = -z_1 = \frac{(R + \chi_c)\sqrt{D}}{\chi_c R}, \quad \beta_2 = -z_2 = \frac{\sqrt{a}}{R};$$

$$B_1 = \frac{R\sqrt{D}}{\Delta_b}, \quad B_2 = \frac{\chi_c(\sqrt{D} - \sqrt{a})}{\Delta_b},$$

$$C_1 = -\frac{[\chi_T(R + \chi_c)\sqrt{D} - \chi_c(R + \chi_T)\sqrt{a}]\sqrt{D}}{\chi_c\chi_T\Delta_b},$$

$$C_2 = \frac{\chi_c(\sqrt{D} - \sqrt{a})\sqrt{a}}{\chi_T\Delta_b}.$$

For $\Delta_b = 0$, we use the notation $\beta_0 = -z_1 = -z_2$. Then, temperature fields in the environment of the drop and on its surface take the form

$$T_0(r, t) = T_\infty + \frac{\eta R\sqrt{a}}{\chi_c r}\frac{B_0}{\beta_0}$$

$$\times\left[\left(\frac{1}{B_0} + \frac{1}{\beta_0}\right)\Phi(\alpha_T, \beta_0, t) + (2\beta_0 t + \alpha_T)\varphi(\alpha_T, \beta_0, t)\right.$$

$$\left. - 2\sqrt{\frac{t}{\pi}}\exp\left(-\frac{\alpha_T^2}{4t}\right)\right], \qquad (20)$$

$$T_{0R}(t) = T_\infty + \frac{\eta\chi_T}{\chi_c}\left\{1 + \frac{C_{01}}{\beta_0}\Phi(\beta_0, t)\right.$$

$$\left. + \frac{C_{02}}{\beta_0}\left[\frac{1}{\beta_0}\Phi(\beta_0, t) + 2\beta_0 t\varphi(\beta_0, t) - 2\sqrt{\frac{t}{\pi}}\right]\right\}, \qquad (21)$$

respectively. Here,

$$B_0 = \frac{\sqrt{D} - \sqrt{a}}{R}, \quad C_{01} = -\frac{\chi_T\sqrt{D} - \chi_c\sqrt{a}}{\chi_c\chi_T},$$

$$C_{02} = \frac{(\sqrt{D} - \sqrt{a})\sqrt{a}}{\chi_T R}.$$

We note that expressions (17)–(21) are linear functions of the concentration difference $c_{1\infty} - c_{1R}$. Relations (17), (18), and (20) do not contain the composite coefficient of the temperature jump, while expressions (19) and (21) depend strongly on the ratio between the composite coefficients of the jumps of temperature and concentration.

According to [1], the rate of change in the drop radius is obtained from concentration distribution (17) as

$$\frac{dR}{dt} = \frac{\xi}{R + \chi_c}\left[1 + \frac{R}{\chi_c}\varphi(\beta, t)\right], \qquad (22)$$

where $\xi = \dfrac{D(c_{1\infty} - c_{1R})nm_1}{\gamma}$ and γ is the density of the drop substance. Expression (22) is valid for any time instant. Using asymptotic expansions of the function erfc(x) for small and large values of its argument, one can find individual expressions for the rate of change in the drop radius for small and large values of time t, respectively. In the latter case,

$$\frac{dR}{dt} = \frac{\xi}{R + \chi_c}\left\{1\right.$$

$$\left. + \frac{R}{\chi_c\beta\sqrt{\pi t}}\left[1 + \sum_{m=1}^{\infty}(-1)^m\frac{1 \times 3 \ldots \times (2m-1)}{(2\beta^2 t)^m}\right]\right\}. \qquad (23)$$

Retaining only the term free of t and then, in addition, the term containing $\dfrac{1}{\sqrt{t}}$ on the right-hand side of formula (23), we arrive at the following approximations of this formula:

$$\frac{dR}{dt} = \frac{\xi}{R + \chi_c}, \quad \frac{dR}{dt} = \frac{\xi}{R + \chi_c}\left[1 + \frac{R^2}{(R + \chi_c)\sqrt{\pi D t}}\right].$$

For $\chi_c = 0$, they go over to the known expressions [1, 4]

$$\frac{dR}{dt} = \frac{\xi}{R}, \quad \frac{dR}{dt} = \frac{\xi}{R}\left(1 + \frac{R}{\sqrt{\pi D t}}\right) \qquad (24)$$

for the rate of change in the drop radius.

We note that relations (24) were derived in the preceding theories from the solution of only one diffusion equation for steady or unsteady regimes, respectively, disregarding the concentration jump and were used at any time instant. In our more general approach, these formulas are the particular cases ($\chi_c = 0$) of approximate expressions (24) applicable only for large times t. Therefore, these expressions can lead to errors for small time values.

The second of formulas (24) yields $\lim\limits_{t \to 0_+} \frac{dR}{dt} = \infty$. At the same time, our formula (22), applicable at any time, provides the finite limit $\lim\limits_{t \to 0_+} \frac{dR}{dt} = \frac{\xi}{\chi_c}$.

Thus, the principal difference of our formula (22) from the one derived earlier for an unsteady rate of growth and evaporation [see the second of formulas (24)] is that formula (22) provides a finite limit at $t \to 0_+$, while the previous expression tends to infinity.

REFERENCES

1. N. A. Fuks, *Evaporation and Growth of Drops in a Gaseous Medium* (Akad. Nauk SSSR, Moscow, 1958; Pergamon Press, London, 1959).
2. Yu. I. Yalamov and V. S. Galoyan, *Dynamics of Drops in Heterogeneous Viscous Media* (Luĭs, Erevan, 1985).
3. I. V. Derevich, Teor. Osn. Khim. Tekhn. **32** (5), 536 (1998).
4. O. M. Todes, in *Problems of Evaporation, Burning, and Gas Dynamics of Disperse Systems* (Odessa, 1968), pp. 151–159.
5. Yu. I. Yalamov and I. Ya. Kolesnik, Kolloidn. Zh. **34** (2), 284 (1972).
6. N. Nix and N. Fukuta, J. Chem. Phys. **58** (4), 1735 (1973).
7. J. C. Carstens and J. T. Zung, J. Colloid Interface Sci. **33** (2), 299 (1970).
8. S. Stefan and D. Borsan, Rev. Roum Phys. **35** (3), 269 (1990).
9. G. Doetsch, *Anleitung zum Praktischen Gebrauch der Laplace Transformation* (R. Oldenbourg, München, 1961; Nauka, Moscow, 1965).

Translated by Yu. Verevochkin

Doklady Physics, Vol. 48, No. 9, 2003, pp. 478–480. Translated from Doklady Akademii Nauk, Vol. 392, No. 2, 2003, pp. 180–182.
Original Russian Text Copyright © 2003 by Altaĭsky.

PHYSICS

Langevin Equation with Scale-Dependent Noise

M. V. Altaĭsky

Presented by Academician D.V. Shirkov on February 14, 2003

Received March 21, 2003

The Langevin equation is one of the most general approximations for the evolution of a dynamic system in a fluctuating environment. It arises when describing a magnet in the presence of magnetic-field fluctuations, hydrodynamic turbulence, stochastic quantization, interface growth, and many other problems [1–4].

In the most general form, the Langevin equation is represented as

$$\frac{\partial\varphi(\mathbf{x},t)}{\partial t} = U[\varphi(\mathbf{x},t)] + \eta(\mathbf{x},t), \qquad \langle\eta(x)\eta(x')\rangle = D(x,x'), \tag{1}$$

where $U[\varphi]$ is the nonlinear interaction potential and $\eta(t,\mathbf{x})$ is Gaussian random noise describing fluctuations of the environment. The Minkowski-like $(d+1)$-dimensional notation $x \equiv (\mathbf{x}, t)$, $k \equiv (\mathbf{k}, \omega)$ is used hereafter. Langevin equation (1) is usually solved by introducing the small parameter λ in the interaction potential U and then solving the system by iterations in each order of the perturbative expansion. The averaging over the Gaussian random force η reduces to calculation of the pair correlation functions $\langle\eta\eta\rangle$. The procedure is simplified by assuming the Gaussian statistics of random noise. In this case, only even-order correlation functions of random noise are nonzero, while all terms containing odd numbers of η vanish. The diagram technique for the iterative solution of the Langevin equation is often called the Wyld diagram technique [5]. Similarly to quantum field theory, loop divergences must be eliminated by renormalization group methods [2, 3].

The structure of divergences arising in the perturbative solution of the Langevin equation depends on a particular type of the correlation function of the random force. Most approximations use the δ-correlated random force of the form

$$\langle\eta(k_1)\eta(k_2)\rangle = (2\pi)^{d+1}\delta(k_1+k_2)D(\mathbf{k}_2). \tag{2}$$

The spatial part of the correlation function $D(\mathbf{k})$ is assumed to be either a constant or a power function ($D(\mathbf{k}) \sim |\mathbf{k}|^{-\beta}$).

A random force acting in a limited range of scales is often physically desirable. For instance, forces inducing hydrodynamic turbulence, as well as a stochastic action on a growing interface, belong to such type of forces. In this paper, we propose a novel method of describing limited-band stochastic actions. It is shown that, for narrow-band noise, an appropriate choice of the correlation functions of the random force yields a theory free of loop divergences. The proposed method preserves the whole structure of the perturbation expansion, and only the space of functions changes. In the limiting case of random force (2), all ordinary results are reproduced.

To study the dynamic system separately at each scale, following [6], we turn from the usual space of random functions $f(x,\cdot) \in (\Omega, \mathcal{A}, P)$, where $f(x) \in L^2(R^d)$ for each given realization of the random process, to the multiscale representation of these functions by the continuous wavelet transform

$$W_\psi(a,\mathbf{b},\cdot) = \int |a|^{-\frac{d}{2}}\overline{\psi\left(\frac{\mathbf{x}-\mathbf{b}}{a}\right)} f(\mathbf{x},\cdot)d^d x. \tag{3}$$

The wavelet transform is performed here only in the *spatial* part, but not in the time part of the argument x, because the structure of divergences and other important properties of the processes under consideration are determined by their spatial localization.

The existence and uniqueness of the inverse wavelet transform

$$f(\mathbf{x},\cdot) = C_\psi^{-1}\int |a|^{-\frac{d}{2}}\psi\left(\frac{\mathbf{x}-\mathbf{b}}{a}\right)W_\psi(a,\mathbf{b},\cdot)\frac{da\,d\mathbf{b}}{a^{d+1}} \tag{4}$$

is ensured by the admissibility condition imposed on the basic wavelet

$$C_\psi = S_d^{-1}\int\frac{|\hat{\psi}(\mathbf{k})|^2}{|k|^d}d^d k = \int\frac{|\hat{\psi}(\mathbf{k})|^2}{a}da < \infty. \tag{5}$$

The area S_d of a unit sphere in d dimensions arises due to the simplifying assumption of the isotropic basis wavelet $\psi(\mathbf{x}) = \psi(|\mathbf{x}|)$.

Joint Institute for Nuclear Research, Dubna, Moscow oblast, 141980 Russia

Space Research Institute, Russian Academy of Sciences, ul. Profsoyuznaya 84/32, Moscow, 117997 Russia
e-mail: altaisky@jinr.ru; altaisly@mx.iki.rssi.ru

1028-3358/03/4809-0478$24.00 © 2003 MAIK “Nauka/Interperiodica”

The use of the wavelet images instead of the original stochastic processes provides extra analytical opportunities. For the case under consideration, the possibility of construction of more than one set of random functions $W(a, \mathbf{b}, \cdot)$, whose images have coinciding correlation functions in the space of $f(x, \cdot)$, is important.

It is easy to check that the correlation function of the image of the processes

$$\langle \hat{W}(a_1, k_1)\hat{W}(a_2, k_2)\rangle = C_\psi(2\pi)^d\delta^d(k_1 + k_2)a_1^{d+1}\delta(a_1 - a_2)D_0$$

coincides with that of white noise

$$\langle \hat{f}(k_1)\hat{f}(k_2)\rangle = (2\pi)^d D_0\delta^d(k_1 + k_2),$$

$$\langle \hat{W}(a_1, k_1)\hat{W}(a_2, k_2)\rangle = (2\pi)^d D_0\delta^d(k_1 + k_2)(a_1a_2)^{d/2}\overline{\hat{\psi}(a_1k_1)\hat{\psi}(a_2k_2)}.$$

Therefore, simulating the random force in the space of wavelet coefficients, we can provide a narrow-band pumping keeping all required properties in the ordinary space.

As an example, let us consider the well-known Kardar–Parisi–Zhang model of interface growth [3]:

$$\dot{Z} - \nu\Delta Z = \frac{\lambda}{2}(\nabla Z)^2 + \eta. \qquad (6)$$

Substituting the wavelet transform in the spatial argument

$$Z(x) = C_\psi^{-1}\int \exp(i(\mathbf{kx} - k_0t))a^{\frac{d}{2}}\hat{\psi}(a\mathbf{k})\hat{Z}(a, k) \times \frac{d^{d+1}k}{(2\pi)^{d+1}}\frac{da}{a^{d+1}} \qquad (7)$$

into Eq. (6), using the random force of the form

$$\langle\hat{\eta}(a_1, k_1)\hat{\eta}(a_2, k_2)\rangle = C_\psi(2\pi)^{d+1} \times\delta^{d+1}(k_1 + k_2)a_1^{d+1}\delta(a_1 - a_2)D(a_2, \mathbf{k}_2), \qquad (8)$$
$$\langle\hat{\eta}(a, k)\rangle = 0,$$

and making straightforward calculations, we arrive at the integral equation

$$(-i\omega + \nu\mathbf{k}^2)\hat{Z}(a, k) = \hat{\eta}(a, k) - \frac{\lambda}{2}a^{\frac{d}{2}}\overline{\hat{\psi}(a\mathbf{k})}C_\psi^{-2}\int(a_1a_2)^{\frac{d}{2}}\hat{\psi}(a_1\mathbf{k}_1)\hat{\psi}(a_2(\mathbf{k} - \mathbf{k}_1)) \times\mathbf{k}_1(\mathbf{k} - \mathbf{k}_1)\hat{Z}(a_1, k_1)\hat{Z}(a_2, k - k_1) \times\frac{d^{d+1}k_1}{(2\pi)^{d+1}}\frac{da_1}{a_1^{d+1}}\frac{da_2}{a_2^{d+1}}.$$

From this equation, we obtain the following expression for the Green's function in the one-loop approximation:

$$G(k) = G_0(k) - \lambda^2G_0^2(k) \times\int\frac{d^{d+1}k_1}{(2\pi)^{d+1}}\Delta(k_1)\mathbf{k}_1(\mathbf{k} - \mathbf{k}_1)|G_0(k_1)|^2\mathbf{kk}_1 \times G_0(k - k_1) + O(\lambda^4), \qquad (9)$$

where $G_0^{-1}(k) = -i\omega + \nu\mathbf{k}^2$ is the zeroth-order approximation for the Green's function and

$$\Delta(k) \equiv G_\psi^{-1}\int\frac{da}{a}|\hat{\psi}(a\mathbf{k})|^2D(a, \mathbf{k}) \qquad (10)$$

is the scale-averaged correlation function of the effective force. The Green's function obtained with random force (8) is independent of the scale $\hat{Z}(a, k) = G(k)\hat{\eta}(a, k)$.

Similarly, for the pair correlation function, we obtain the formula

$$C(a_i, a_f, k) = \frac{\lambda^2}{2}|G_0(k)|^2\overline{\hat{\psi}(a_i\mathbf{k})\hat{\psi}(-a_f\mathbf{k})} \times\int\frac{d^{d+1}k_1}{(2\pi)^{d+1}}|G_0(k_1)|^2|G_0(k - k_1)|^2 \times[\mathbf{k}_1(\mathbf{k} - \mathbf{k}_1)]^2\Delta(k_1)\Delta(k - k_1). \qquad (11)$$

For the scale-independent correlation function of the force, after the integration in Eq. (10), expressions (9) and (11) reduce to the known result [3].

Let us consider the single-band stirring

$$D(a, \mathbf{k}) = \delta(a - a_0)D(\mathbf{k}) \qquad (12)$$

and the basic wavelet in the form of the "Mexican hat"

$$\hat{\psi}(\mathbf{k}) = (2\pi)^{d/2}(-i\mathbf{k})^2\exp\left(-\frac{\mathbf{k}^2}{2}\right), \qquad (13)$$
$$C_\psi = (2\pi)^d.$$

Substituting Eqs. (12) and (13) into Eq. (9) and integrating with respect to the frequency, in the leading order in the small parameter $x = \frac{|\mathbf{k}|}{|\mathbf{k}_1|}$, we obtain the contribution to the Green's function ($d > 2$):

$$G(k) = G_0(k) + \lambda^2G_0^2(k)\frac{S_d}{(2\pi)^d}\frac{a_0^3k^2}{\nu^2}\frac{d-2}{8d} \times\int_0^\infty D(\mathbf{q})e^{-(a_0\mathbf{q})^2}q^{d+1}dq + O(\lambda^4). \qquad (14)$$

For constant $D(\mathbf{q}) = D_0$, this contribution to the Green's function is finite and does not require any further renormalization. In the limit ω, $\mathbf{k} \to 0$, the one-loop contribution to the surface tension ν, which follows from Eq. (14), is equal to

$$\nu_{\text{eff}} = \nu\left[1 - \frac{\lambda^2}{\nu^3 k^2}\frac{d-2}{16d}\frac{S_d}{(2\pi)^d}a_0^{1-d}D_0\Gamma\left(1+\frac{d}{2}\right) + O(\lambda^4)\right]. \quad (15)$$

We note that Eqs. (14) and (15) were derived from one-loop integral (9) after substitution $k_1 = q + \frac{k}{2}$ and perturbation expansion in the small parameter $x = \frac{k}{q}$ [7]. For particular correlation functions, the direct numerical estimate of integral (9) is more adequate. Similar calculations can be performed for other interaction potentials. For instance, for the quadratic interaction $\frac{\lambda^2}{2}Z^2$, the counterparts of Eqs. (9) and (11) differ from that obtained above only by the absence of the scalar products of the wave vectors in each vertex.

Concerning the contribution of higher orders of the perturbation expansion, we should say that, for the basic wavelets $\hat{\psi}(k)$ localized in the k space and limited-band noise $D(a, k)$, the effective coupling constant $\bar{\lambda}$, which is the actual parameter of the perturbation expansion [8], can be made small by decreasing the noise amplitude. For instance, for the basic wavelets from the family

$$\hat{\psi}(k) = (2\pi)^{d/2}(-ik)^n \exp\left(-\frac{k^2}{2}\right), n > 0,$$

and the noise correlation function $D(a, k) = D_0\delta(a - a_0)$, the effective coupling constant is equal to

$$\bar{\lambda}^2 = \frac{\lambda^2}{\nu^3}\frac{D_0}{a_0}.$$

ACKNOWLEDGMENTS

I am grateful to Profs. N. Antonov and V. Priezzhev for stimulating discussions.

REFERENCES

1. P. C. Martin, E. D. Sigia, and H. A. Rose, Phys. Rev. A **8**, 423 (1973).
2. L. Ts. Adzhemyan, A. N. Vasil’ev, and Yu. M. Pis’mak, Teor. Mat. Fiz. **57**, 268 (1983).
3. M. Kardar, G. Parisi, and Y.-C. Zhang, Phys. Rev. Lett. **56**, 889 (1986).
4. J. Zinn-Justin, Nucl. Phys. B **275**, 135 (1986).
5. H. W. Wyld, Ann. Phys. **14**, 143 (1961).
6. M. V. Altaisky, Eur. J. Phys. B **8**, 613 (1999).
7. E. Medina, M. Kardar, G. Parisi, and Y.-C. Zhang, Phys. Rev. A **39** (6), 3053 (1989).
8. D. Forster, D. R. Nelson, and M. J. Stephen, Phys. Rev. A **16**, 732 (1977).

Translated by M. Altaĭsky

Doklady Physics, Vol. 48, No. 9, 2003, pp. 481–486. Translated from Doklady Akademii Nauk, Vol. 392, No. 3, 2003, pp. 322–327.
Original Russian Text Copyright © 2003 by Alexandrov.

PHYSICS

On the Theory of the Formation of the Two-Phase Concentration-Supercooling Region

D. V. Alexandrov

Presented by Academician N.A. Vatolin March 19, 2003

Received March 31, 2003

Mathematical simulation of crystallization processes is extensively used in practice when obtaining castings and ingots with given properties [1, 2]. Problems with one or several labile interfaces of the solidification of melts in limited domains belong to the most difficult problems for analytical solutions by current methods of mathematical physics. Contrary to many other problems that are often of purely mathematical interest, such problems are inevitably interesting for practical predictions based on theoretical simulation. In addition, they are characterized by mathematical models of corresponding phenomena that are maximally close to reality. It is much very difficult to solve such problems analytically. For this reason, many researches works often analyze these problems numerically. Unfortunately, such a numerical analysis does not present the complete pattern of the process and does not cover all parametric dependences of the quantities in question.

The Stefan problem of the frontal crystallization of melts is one of the classical problems of this type (see, e.g., [3]). However, the front after the onset of the crystallization process is not necessarily an ideal plane. In particular, this idealized pattern is broken under the condition of concentration supercooling ahead of the plane solidification front [4]. This condition implies that the concentration gradient is higher than its temperature analogue at the solidification front, i.e.,

$$-m\frac{\partial\sigma}{\partial\xi} > \frac{\partial\theta_l}{\partial\xi}, \quad \xi = \Sigma(\tau) \tag{1}$$

and is responsible for the formation of a supercooled-melt region ahead of the plane front, where solid-phase crystals can grow and which promotes the appearance of the conditions of the dominate growth of random protrusions on the plane front. Here, σ is the impurity concentration, θ_l is the temperature of the melt, m is the liquidus-line slope, ξ is the spatial coordinate along the motion of the crystallization front, τ is time, and $\Sigma(\tau)$ is the position of the solidification front. In other words, a two-phase concentration-supercooling region is formed ahead of the phase front [5]. The description of the solidification process in the standard thermal diffusion model with the phase front is obviously inadequate to the physical conditions of crystallization. Therefore, for times exceeding the time τ_* of the formation of the two-phase region, it is appropriate to use one of a solidification models that takes into account the two-phase region (see, e.g., [6–9]). The directional crystallization including the formation of the two-phase region in a domain of length L was previously simulated numerically for the following two cooling regimes on its $\xi = 0$ wall (heat flux was specified on the second wall $\xi = L$): first, active regime smooth in time and, second, passive regime according to the Newton’s law of heat exchange with the environment [10–13]. The further discussion is devoted to analytical calculation of both the time of the formation of the two-phase region and accompanying parameters describing the crystallization process with the active cooling regime on the $\xi = 0$ wall.

We consider the crystallization process in a domain of length L. In the melt, where $\Sigma(\tau) < \xi < L$, and in the solid phase, where $0 < \xi < \Sigma(\tau)$, we have the heat conduction equations

$$\frac{\partial\theta_l}{\partial\tau} = a_l\frac{\partial^2\theta_l}{\partial\xi^2}, \quad \Sigma(\tau) < \xi < L, \tag{2}$$

$$\frac{\partial\theta_s}{\partial\tau} = a_s\frac{\partial^2\theta_s}{\partial\xi^2}, \quad 0 < \xi < \Sigma(\tau) \tag{3}$$

and impurity diffusion equation

$$\frac{\partial\sigma}{\partial\tau} = D\frac{\partial^2\sigma}{\partial\xi^2}, \quad \Sigma(\tau) < \xi < L, \tag{4}$$

where θ_s is the temperature of the solid phase; a_l and a_s are the thermal diffusivities of the liquid and solid phases, respectively; and D is the diffusion coefficient

Department of Mathematical Physics, Ural State University, pr. Lenina 51, Yekaterinburg, 620083 Russia
e-mail: dmitri.alexandrov@usu.ru

of the impurity (the diffusion of the impurity in the solid phase is traditionally disregarded).

At the phase-transition interface, crystallization front, the temperatures of both phases are equal to the phase transition temperature, and the balance conditions for heat and impurity mass are satisfied; i.e.,

$$\theta_l = \theta_s, \quad \xi = \Sigma(\tau), \tag{5}$$

$$\theta_l = \theta_* - m\sigma, \quad \xi = \Sigma(\tau), \tag{6}$$

$$\lambda_s \frac{\partial\theta_s}{\partial\xi} - \lambda_l \frac{\partial\theta_l}{\partial\xi} = L_V \frac{d\Sigma(\tau)}{d\tau}, \quad \xi = \Sigma(\tau), \tag{7}$$

$$(1-k)\sigma\frac{d\Sigma(\tau)}{\partial\tau} + D\frac{\partial\sigma}{\partial\xi} = 0, \quad \xi = \Sigma(\tau). \tag{8}$$

Here, θ_* is the phase transition temperature for the pure melt; λ_s and λ_l are the thermal conductivities of the solid and liquid phases, respectively; L_V is the latent heat of solidification; k is the impurity distribution coefficient equal to the ratio of the impurity concentration σ_s in the solid phase to the impurity concentration in the melt at the crystallization front, i.e.,

$$k = \frac{\sigma_s}{\sigma}, \quad \xi = \Sigma(\tau). \tag{9}$$

Since diffusion of the impurity in the solid phase is disregarded, formula (9) provides the impurity concentration absorbed by the plane solidification front at every time and thereby enables one to determine the concentration profile in the solid phase.

We consider that the right boundary $\xi = L$ is impenetrable for the impurity, i.e.,

$$\frac{\partial\sigma}{\partial\xi} = 0, \quad \xi = L \tag{10}$$

and specify the heat flux as

$$\frac{\partial\theta_l}{\partial\xi} = g_l, \quad \xi = L, \tag{11}$$

where g_l is the fixed temperature gradient.

We consider that the left boundary $\xi = 0$ is smoothly cooled in time, i.e.,

$$\lambda_s \frac{\partial\theta_s}{\partial\xi} = \lambda_l g_l + \alpha\tau, \quad \xi = 0, \tag{12}$$

where α is the cooling coefficient.

As the initial conditions, we specify the position of the crystallization front and the temperature and concentration profiles of the form

$$\Sigma(0) = \varepsilon L; \tag{13}$$

$$\begin{gathered} \theta_l = \theta_* - m\sigma_\infty + g_l(\xi - \Sigma(0)), \\ \tau = 0, \quad \Sigma(0) < \xi < L; \end{gathered} \tag{14}$$

$$\begin{gathered} \theta_s = \theta_* - m\sigma_\infty + \frac{\lambda_l}{\lambda_s} g_l(\xi - \Sigma(0)), \\ \tau = 0, \quad 0 < \xi < \Sigma(0); \end{gathered} \tag{15}$$

$$\sigma = \sigma_\infty, \quad \tau = 0, \quad \Sigma(0) < \xi < L, \tag{16}$$

where σ_∞ is the initial impurity concentration.

Thus, the crystallization front at the initial time is assumed to exist at a certain small distance ($\varepsilon \ll 1$ is the small parameter) from the left boundary of the domain under consideration. We specify a linear temperature profile with individual slopes on both sides from the crystallization front so that the difference between heat fluxes at the front is equal to zero at the initial time $\tau = 0$ and, therefore, the front velocity $\frac{d\Sigma}{d\tau}$ is also equal to zero according to boundary condition (7).

The time τ_* of the formation of the two-phase region is determined from the condition for concentration supercooling:

$$-m\frac{\partial\sigma}{\partial\xi} = \frac{\partial\theta_l}{\partial\xi}, \quad \xi = \Sigma(\tau). \tag{17}$$

The model specified by Eqs. (1)–(17) was numerically analyzed in [10–12], where, for the case of concentration supercooling, when inequality (1) is valid at the crystallization front, condition (17) corresponding to the approximation of the narrow quasi-equilibrium two-phase region [10, 14] was used instead of condition (8).

Figure 1 shows the calculation results for the iron–nickel alloy whose thermal physical characteristics are given in Table 1 for $\tau = 360$ s.

Calculations show that condition (17) is satisfied at time $\tau = \tau_* = 221.9$ s. Moreover, this corresponds to the maximum in the concentration profile in the solid phase [for times $\tau > \tau_*$, calculation was carried out with the replacement of condition (8) with condition (17), which corresponds to the model of a narrow quasi-equilibrium two-phase region]. Calculations also show that, even when the two-phase region between the solid phase and melt is quite short, its presence is responsible for certain differences in the impurity distribution in the solid phase compared to the standard formulation of the problem of solidification with the plane crystallization front, where the formation of the two-phase region is disregarded (in this case, the impurity concentration in the solid phase increases monotonically with the spatial coordinate, as is shown in Fig. 2). A slightly pronounced maximum appearing under solidification when the narrow quasi-equilibrium two-phase region ahead of the crystallization front is taken into account is explained as follows. Solidification proceeds through the frontal mechanism before the formation of the two-phase region. The solidification front penetrating through the melt removes the impurity ($k < 1$); i.e., the impurity concentration in the liquid phase near the front is higher than that deep in the melt. After the formation of the two-phase region ahead of the front (time of switching of the boundary condition), solid-phase elements in the two-phase region grow under the condition that the impurity concentration in the surrounding melt is lower than the concentration in the melt near the interface between the solid phase and two-phase region. Therefore, when such elements of the solid phase are absorbed by the solidified melt, the impurity concentration in the solid phase decreases compared to the concentration before the formation of the two-phase region. Such a behavior of the impurity concentration in the solid phase was previously observed in [15] for the Al–Cu and Sn–Pb alloys.

Calculations also show that the temperature profiles in both phases during crystallization remain almost linear functions of the spatial coordinate, as is clearly seen in Fig. 1. This occurs because the relaxation times of the temperature fields in both phases are shorter than the relaxation time for the diffusion field by several orders of magnitude.

One more conclusion obtained in [10–12] is that the crystallization rate $\frac{d\Sigma}{d\tau} = \mu\tau$ increases linearly with time when the formation of the two-phase region is taken into account for all calculation times of the processes (both for times $\tau < \tau_*$, when crystallization proceeds with the phase front, and for times $\tau > \tau_*$, when crystallization proceeds in the presence of the two-phase concentration-supercooling region). In this case, the proportionality coefficient μ remains unchanged both before and after the formation of the two-phase region.

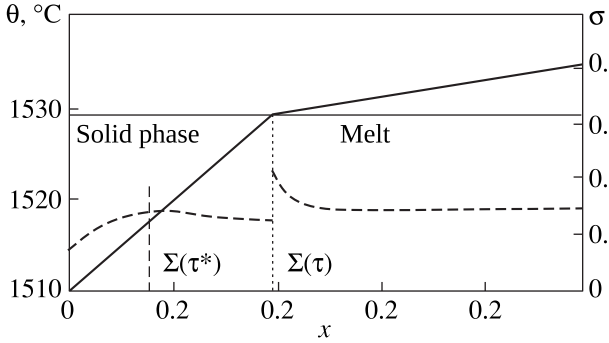

Fig. 1. (Dashed lines) Concentration and (solid lines) temperature profiles, (horizontal straight line) phase transition temperature, and the position $\Sigma(\tau)$ of the crystallization front for the solidification of the iron–nickel melt for τ = 360 s. The position of the crystallization front for $\tau = \tau_*$, as well as the corresponding maximum $x = \xi/L$ of the impurity concentration in the solid phase, is indicated.

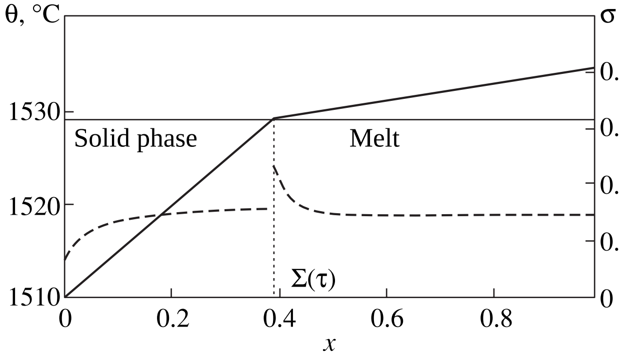

Fig. 2. Same as Fig. 1, but for calculations disregarding the formation of the two-phase region at time $\tau = \tau_*$ = 221.9 s.

We emphasize one more circumstance. As follows from [10, 11], at the time of the formation of the two-phase region, the impurity concentration reaches its maximum not only at the crystallization front but at any melt point spaced by a certain fixed distance h either from the solid phase–melt interface before the formation of the two-phase region or from two-phase region–melt after that time but with allowance for the thickness δ of the two-phase region, i.e., at the distance $h + \delta$. This occurs because the crystallization front removes the impurity before the formation of the two-phase region and thereby increases the impurity concentration in the melt at a fixed distance h from the front. After the formation of the two-phase region, the distance h must be measured from the two-phase region–melt interface (shift by the thickness of the two-phase region), which corresponds to a lower concentration than that before the formation time because this quantity is shifted by δ and h is replaced by the distance $h + \delta$ measured from the melt–two-phase region interface. The two-phase region itself is simulated by the discontinuity surface, where condition (8) is replaced by condition (17) [10, 11]. Considering the impurity concentration in the melt and taking into account the above discussion, we conclude that, at any melt point spaced either by a fixed distance h from the melt–solid phase interface for $\tau < \tau_*$ or by distance $h + \delta$ from the melt–two-phase region interface for $\tau > \tau_*$, the impurity concentration is lower than the impurity concentration at $\tau = \tau_*$.

Since temperature profiles are linear at any time (see Figs. 1, 2), Eqs. (2) and (3) can be approximated by their time-independent analogues

$$\frac{\partial^2\theta_l}{\partial\xi^2} = 0, \quad \Sigma(\tau) < \xi < L; \quad \frac{\partial^2\theta_s}{\partial\xi^2} = 0, \quad 0 < \xi < \Sigma(\tau),$$

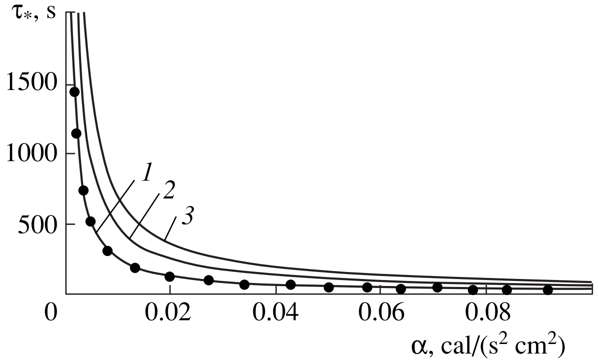

Fig. 3. Time τ_* of the formation of the two-phase region as a function of the cooling parameter α as calculated by formula (27) for the temperature gradient g_l = (*1*) 5, (*2*) 10, and (*3*) 15°C/cm. The points are the results of the numerical solution according to [12].

whose solutions have the form

$$\begin{aligned} \theta_l(\tau, \xi) &= A_1(\tau) + A_2(\tau)\xi, \\ \theta_s(\tau, \xi) &= B_1(\tau) + B_2(\tau)\xi. \end{aligned} \tag{18}$$

Substituting solutions (18) into conditions (11), (12), and (5), we determine the coefficients A_2 and B_2 and the linear combination of the coefficients A_1 and B_1:

$$A_2 = g_l, \quad B_2(\tau) = \frac{\lambda_l}{\lambda_s} g_l + \frac{\alpha}{\lambda_s}\tau, \tag{19}$$

$$A_1(\tau) = B_1(\tau) + \left(\frac{\lambda_l}{\lambda_s} g_l - g_l + \frac{\alpha}{\lambda_s}\tau\right)\Sigma(\tau). \tag{20}$$

Thermal physical properties of the Fe–Ni alloy and parameters used in calculations

k	0.68
θ_*	1529.5°C
m	2.65°C/wt %
L_V	3398.5 cal/cm^3
D	5×10^{-5} cm^2/s
λ_l	0.1 cal/(s cm °C)
λ_s	0.177 cal/(s cm °C)
a_l	0.14 cm^2/s
a_s	0.25 cm^2/s
σ_∞	0.3 wt %
g_l	10°C/cm
α	0.02 cal/(s^2 cm^2)
ε	0.01
L	1 cm

Then, substituting distributions (18) into boundary condition (7) and taking into account relations (19), we obtain

$$\frac{d\Sigma}{d\tau} = \frac{\alpha}{L_V}\tau = \mu\tau. \tag{21}$$

This condition, which is the linear law for the crystallization rate, agrees well with the numerical calculations made in [10, 11]. The second relation between the coefficients A_1 and B_1 can be obtained by constructing the solution of the concentration problem specified by Eqs. (4), (8), (10), and (16) and then substituting it into boundary condition (6). The resulting relation, together with expression (20), enables one to determine both A_1 and B_1.

We now pass to the determination of the time τ_* of the formation of the two-phase region. Going over to the reference frame $\eta = \xi - \Sigma(\tau)$ moving with velocity $\mu\tau$ [see Eq. (21)], disregarding the effect of the first wall on the impurity distribution (tending the coordinate η on this wall to infinity), and introducing the new variable $q(\tau, \eta) = \sigma(\tau, \eta) - \sigma_\infty$, we arrive at the following formulation of the problem:

$$\frac{\partial q}{\partial \tau} = \mu\tau\frac{\partial q}{\partial \eta} + D\frac{\partial^2 q}{\partial \eta^2}, \quad 0 < \eta < \infty, \tag{22}$$

$$(1-k)\mu\tau q + (1-k)\mu\tau\sigma_\infty + D\frac{\partial q}{\partial \eta} = 0, \quad \eta = 0, \tag{23}$$

$$\frac{\partial q}{\partial \eta} = 0, \quad \eta \longrightarrow \infty, \tag{24}$$

$$q = 0, \quad \tau = 0. \tag{25}$$

Further, taking into account that the impurity concentration at any point (any coordinate η) of the liquid phase is maximal at time τ_*, we equate the left-hand side of Eq. (22) to zero and integrate the result with respect to η form 0 to ∞. Using conditions (24) and the limit $q \longrightarrow 0$ for $\eta \longrightarrow \infty$, which represents the condition of the constant impurity concentration at the right boundary formally shifted to infinity, we obtain

$$q = \frac{Dg_l}{m\mu\tau_*}, \quad \eta = 0, \quad \tau = \tau_*. \tag{26}$$

Here, we also take into account that $\frac{\partial q}{\partial \eta} = -\frac{g_l}{m}$ for $\eta = 0$ and $\tau = \tau_*$ according to Eqs. (17)–(19). Combining Eqs. (23) and (26), we determine both the time of the formation of the two-phase region and impurity concentration at the crystallization front on the melt side at this time:

$$\tau_* = \frac{kDg_l}{(1-k)\mu m\sigma_\infty}, \quad \sigma = \frac{\sigma_\infty}{k}, \quad \eta = 0, \quad \tau = \tau_*. \tag{27}$$

It is interesting that the resulting concentration $\frac{\sigma_\infty}{k}$ coincides with the impurity concentration at the crystallization front under the frontal solidification of the melt with the constant rate.

Taking into account that $\mu = \frac{\alpha}{L_V}$ [see Eq. (21)], we show (see Fig. 3) the formation time of the two-phase region that is calculated by formula (27) as a function of the cooling parameter α. As is easily seen, expression (27) agrees well with the numerical solution [12] of the problem (to avoid overcrowdingloading of the figure, formula (27) compares with numerical calculations [12] only for line *1*; other lines exhibit virtually the same complete agreement between theory under development and numerical solution of the problem).

We now construct the solution of the concentration problem specified by Eqs. (22)–(25) for quite small times after the onset of the crystallization process. Since the impurity concentration profile at initial times is an almost linear function over the entire liquid phase, the derivative $\frac{\partial\sigma}{\partial\xi}$ presenting the slope of this function to the coordinate axis is small. Moreover, the concentration deviates slightly from the σ_∞ value for these times. The above circumstances allow the linearization of the concentration problem with the perturbative inclusion of terms omitted in the zeroth approximation.

Substituting the concentration q in the form of the expansion

$$q = q_0 + q_1 + q_2 + \ldots, \tag{28}$$

where each subsequent term is assumed much less than the preceding term. Taking into account the above discussion and expansion terms up to the first order, we represent the problem specified by Eqs. (22)–(25) in the form of a problem split into the following two subproblems for q_0 and q_1:

$$\begin{gathered}\frac{\partial q_0}{\partial\tau} = D\frac{\partial^2 q_0}{\partial\eta^2}, \quad 0 < \eta < \infty;\\ (1-k)\mu\tau\sigma_\infty + D\frac{\partial q_0}{\partial\eta} = 0, \quad \eta = 0;\end{gathered} \tag{29}$$

$$\begin{gathered}\frac{\partial q_1}{\partial\tau} = \mu\tau\frac{\partial^2 q_0}{\partial\eta^2} + D\frac{\partial^2 q_1}{\partial\eta^2}, \quad 0 < \eta < \infty;\\ (1-k)\mu\tau q_0 + D\frac{\partial q_1}{\partial\eta} = 0, \quad \eta = 0.\end{gathered} \tag{30}$$

In this case, Eqs. (24) and (25) take the form

$$\frac{\partial q_i}{\partial\eta} = 0, \quad \eta \to \infty; \quad q_i = 0, \quad \tau = 0 \tag{31}$$

valid for all q_i, $i = 0, 1, \ldots$. Solving the problems specified by Eqs. (29)–(31) and substituting the solutions into Eq. (28), one can determine the impurity concentration at the initial stages of melt solidification in an ingot mould.

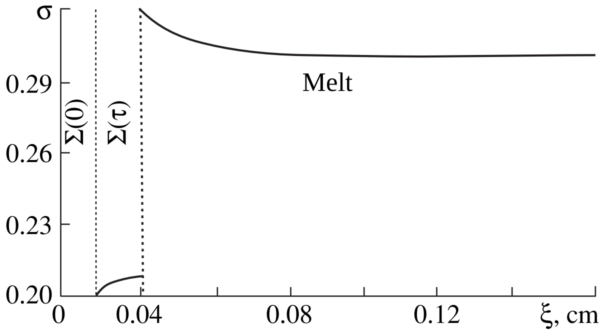

Fig. 4. Impurity distribution in the solid and liquid phases at time $\tau = 10$ s for the test alloy for $\alpha = 0.2$ cal/(s^2 cm^2) according to formula (28). Zero-approximation lines q_0 and numerical solution of the problem almost completely lie on the displayed graphs. The vertical dotted straight lines are the positions of the crystallization front. The impurity concentrations in the liquid and solid phase at the front at a time of 10 s are equal to 0.319 and 0.217, respectively, and the position of the crystallization front is equal to 0.013 cm. According to Eq. (27), the two-phase region nucleates at $\tau = \tau_* = 22.7$ s.

Each of subproblems (29)–(31) can be solved by the Laplace transform. Omitting simple but cumbersome manipulations, we represent write the result

$$q_0(\tau,\eta) = \frac{\sigma_\infty(1-k)\mu}{\sqrt{\pi D}}\int_0^\tau \exp\left[-\frac{\eta^2}{4Dt}\right]\frac{\tau-t}{\sqrt{t}}dt,$$

$$q_1(\tau,\eta) = \frac{\sigma_\infty(1-k)\mu^2}{2D\sqrt{\pi}}\left(\frac{5}{2}(1-k) - \frac{9}{8} - \frac{9\eta}{8\sqrt{D}}\right)$$

$$\times\int_0^\tau \exp\left[-\frac{\eta^2}{4Dt}\right]\frac{(\tau-t)^2}{\sqrt{t}}dt$$

$$-\frac{\sigma_\infty(1-k)\mu^2\eta^2}{192D^2\sqrt{\pi}}\int_0^\tau \exp\left[-\frac{\eta^2}{4Dt}\right]\frac{(\tau-t)^4}{\sqrt{t}}dt.$$

The above successive approximation procedure can be continued and always allows the refinement of the solution of the problem. Figure 4 shows the calculations of the impurity concentration in the liquid and solid phases by Eq. (28) for the iron–nickel alloy [impurity concentration in the solid phase at each time is determined by Eq. (9)]. We emphasize that the found solution makes it possible to completely determine and the temperature field according to boundary condition (6) and Eqs. (18)–(20).

Thus, if the solidification process proceeds with large cooling coefficients (which correspond to small times τ_* according to Fig. 3), the resulting solution completely determines the solution of the frontal problem up to the time of the formation of the two-phase region, which generally determines the application limits of the phase front model.

ACKNOWLEDGMENTS

This work was supported by the Russian Foundation for Basic Research (project nos. 01-02-96430Ural and 02-03-96437Ural), the Ministry of Education of the Russian Federation (project no. E02-4.0-86), and the US Civilian Research and Development Foundation for the Independent States of the Former Soviet Union (grant no. REC-005).

REFERENCES

1. M. Flemings, *Solidification Processing* (McGraw-Hill, New York, 1974; Mir, Moscow, 1977).
2. B. Chalmers, *Principles of Solidification* (Wiley, New York, 1964; Metallurgiya, Moscow, 1968).
3. N. A. Avdonin, *Mathematical Description of Crystallization Processes* (Zinatne, Riga, 1980).
4. G. P. Ivantsov, Dokl. Akad. Nauk SSSR **81** (2), 179 (1951).
5. V. T. Borisov, *Theory of the Two-Phase Region of a Metallic Ingot* (Metallurgiya, Moscow, 1987).
6. R. N. Hills, D. E. Loper, and P. H. Roberts, Q. J. Mech. Appl. Math. **36**, Part 4, 505 (1983).
7. Yu. A. Buevich, L. Yu. Iskakova, and V. V. Mansurov, Prikl. Mekh. Tekh. Fiz., No. 4, 46 (1990).
8. D. V. Aleksandrov, Dokl. Akad. Nauk **375**, 172 (2000) [Dokl. Phys. **45**, 569 (2000)].
9. D. V. Alexandrov, Acta Mater. **49**, 759 (2001).
10. Yu. A. Buyevich, D. V. Alexandrov, and V. V. Mansurov, *Macrokinetics of Crystallization* (Begell House, New York, 2001).
11. D. V. Alexandrov, A. G. Churbanov, and P. N. Vabishchevich, Int. J. Fluid Mech. **26** (2), 248 (1999).
12. D. V. Aleksandrov and M. E. Komarovskiĭ, in *Proceedings of 19th Russian Conference on Structure and Properties of Metallic and Slag Melts* (Yuzhno-Ural. Gos. Univ., Chelyabinsk, 2001), Vol. 4, p. 98.
13. P. N. Vabishchevich, V. V. Mansurov, and A. G. Churbanov, Khim. Prom., No. 10, 39 (1994).
14. Yu. A. Buevich, L. Yu. Iskakova, and V. V. Mansurov, Teplofiz. Vys. Temp. **29** (2), 286 (1991).
15. A. L. Maples and D. R. Poirier, Metall. Trans. B **15**, 163 (1984).

Translated by R. Tyapaev

Doklady Physics, Vol. 48, No. 9, 2003, pp. 487–489. Translated from Doklady Akademii Nauk, Vol. 392, No. 3, 2003, pp. 328–331.
Original Russian Text Copyright © 2003 by Babich, Il'kaev, Loĭko, Pavlovskaya.

PHYSICS

Structure of Electron and Ion Beams Generated by High-Voltage Nanosecond Discharge in Deuterium and Air

L. P. Babich, Academician R. I. Il'kaev, T. V. Loĭko, and N. G. Pavlovskaya

Received April 15, 2003

In [1, 2], a complicated spatial structure of electron beams generated by high-voltage discharges in high vacuum was discovered. The beam patterns beyond the anode, which had been produced by the high-energy part of the electron spectrum, consisted of ordered bands. This fact testifies to the existence of self-organization in beam formation processes. The regular beam structure was with the formation of an ordered distribution of centers of explosive electron emission (ectons [3]) on the cathode due to the Rayleigh–Taylor instability of explosive plasma on the cathode surface [1] or suppression of emission in a certain vicinity of the existing ecton [2]. In the present study, we observed the same ordered structure of electron beams generated by high-voltage nanosecond discharges in rather dense gases at high overvoltages. We have performed direct registration of accelerated-ion beams generated by high-voltage nanosecond discharges. This has also demonstrated the existence of the same characteristic ordered structure.

In the case of multiple overvoltages, the high-voltage nanosecond discharges in dense gases develop in the mode of generation of intense flows of runaway electrons [4]. The high-voltage nanosecond discharges in deuterium at pressures $P = 0.01$–20 Torr generate nanosecond neutron pulses in a tritium-containing target located on the cathode [5, 6]. A maximum yield of 10^6 neutrons per pulse was observed at $P = 0.3$ Torr [6]. The production of neutrons indicates that D^+ and D_2^+ ions are accelerated up to energies providing a noticeable efficiency of nuclear fusion reactions. For example, the maximum of the cross section for the ${}_1H^3({}_1d^2, {}_0n^1){}_2He^4$ reaction is attained at the deuteron energy 109 keV. As far as the dependence of the neutron yield on the deuterium pressure has a pronounced maximum, the generation of accelerated ion beams is a gas-discharge effect [5]. Nuclear fusion is a process of the second kind of smallness with respect to both formation of gas plasma and acceleration of ions. Therefore, ion acceleration up to lower energies, where nuclear fusion is inefficient, is realized in the region of much higher pressures [5].

In the present study, we investigated the structure of charged-particle beams generated in a diode in which a hollow cylinder 7 mm in diameter and made of 50-μm tantalum foil played the role of a high-voltage electrode. The cylinder axis was orthogonal to the grounded plane electrode. The interelectrode spacing d was varied within the limits of 2 to 5 mm. High-voltage pulses having an amplitude of about 800 kV, front duration of 1 ns, and total duration of 30 ns were applied to the diode [7]. At $P = 0.05$–0.5 Torr, voltage pulses with an amplitude of 400–800 kV arise in the diode. These pulses correspond to multiple overvoltages, since the static breakdown voltage does not exceed 20 kV in the Pd region under investigation. Currents with the amplitude of 2–4 kA and duration of 15–20 ns flow in the diode. The beams were recorded by the TsVID-0.1-1 dosimetric films with the mass thickness of 10 mg cm^{-2}, which were placed outside of the diode on the plane electrode.

The electron-beam structure was studied in a diode with a plane anode made of aluminum foil of the thickness $\Delta = 15$ μm. Figure 1 exhibits single-pulse beam patterns for discharges in deuterium. A stack of four films was placed beyond the anode. After passing the beam through the stack, the beam intensity decreased so that in each next film a portion consisting of electrons of higher energies was recorded. Filtration by the films allowed us to reveal a fine space–energy structure of the beam, which appeared to be extremely inhomogeneous. We observed bands directed perpendicularly to the edge of the cylindrical cathode. The bands converged to the cathode center, where the beam density was so high that the film locally melted. In the case of the weak filtration, the diameter of the beam pattern exceeds the cathode diameter by approximately a factor of two. The beam structure was observed most clearly in the fourth film after filtration of low-energy electrons by preceding films. These electrons are subjected to

Russian Federal Nuclear Center All-Russia Research Institute of Experimental Physics, pr. Mira 37, Sarov, Nizhegorodskaya oblast, 607188 Russia

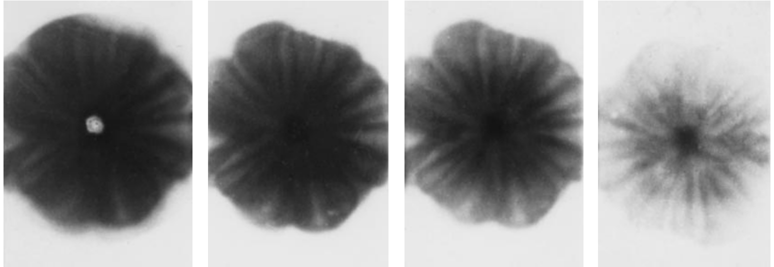

Fig. 1. Patterns of electron beams generated by discharges in deuterium at $P = 0.3$ Torr and $d = 2.5$ mm. The anode is a hollow thin-wall cylinder.

strong scattering and to the action of the space charge field. Owing to these factors, the initial structure in the low-energy region is eroded. The fourth film is available only for electrons of energies exceeding 150 keV. The size beam patterns for electrons of such energies negligibly exceeds the cathode diameter.

The structure of ion beams was investigated in the diode whose high-voltage electrode (cylinder) was used as an anode. A nickel mesh 4 μm thick and with a cell size of 18 × 18 μm served as a cathode. The patterns formed by ion beams generated by discharges in deuterium also demonstrate bands directed perpendicularly to the anode edge. (Fig. 2). The ion-beam structure is similar to that of electron beams observed strong filtration. This is natural, since ions appear along the ionization tracks of electrons in gas.

The ion energy measured with a wedge consisting of micron-size Mylar films is close to 300 keV. In accordance with the data of [8] on the neutron yield from a tritium target as a function of the energy of accelerated deuterons, an electric current of accelerated deuterium ions of the order of 10 A corresponds to the neutron yield of 10^6 neutrons and of 2.5-ns pulse duration. This intensity of the electric-current is much lower than the total discharge current, which attains 2.5 kA. Direct measurements of deuterium ion-beam electric-current intensity were performed with a collector located at 1.7 cm from the mesh cathode. The 3-μm Mylar film decreasing the ion-beam intensity by a factor of five isolated the evacuated collector chamber from the diode gas gap. We recorded an ion-beam electric-current pulse having an amplitude of ~1.5 A and duration of 3 ns. With allowance for the beam absorption in the cathode and in the Mylar film, we can expect that the ion-beam current does not exceed 10 A. The delay time of the ion arrival at the collector compared to the time corresponding to the voltage pulse maximum attains 6–7 ns. This is caused by both the delay of the discharge development with respect to the moment of the voltage application and passage by ions of the distance between the anode and the collector. The measured delay time agrees with the estimate of the deuterium-ion energy of 300 keV corresponding to a velocity of $\sim 4 \times 10^8$ cm s^{-1} and the 4-ns time of flight between the cathode and collector.

The structure of electron and ion beams and time characteristics of ion beams in the case of discharges in air turned out similar to those in deuterium. The patterns of electron beams produced by discharges in air at $P = 0.04$–1 Torr were obtained for a single pulse. The only exclusion corresponds to $d = 5$ mm and $P = 1$ Torr. It took 10 pulses in order to obtain this pattern, since the voltage on the diode and, hence, the electron energy decrease with the rise of Pd. The diameter D of patterns formed by the beam considerably exceeds the cathode diameter of 7 mm. D increases with d and decreases with P. For example, at $P = 0.04$ Torr and $d = 5$ mm, $D \approx 25$ mm, whereas for $d = 9$ mm, $D \approx 45$ mm. The clear radiant structure is observed up to $P = 0.3$ Torr. At $P > 1$ Torr, this structure is eroded due to scattering of electrons on gas molecules.

The characteristic feature of high-voltage electrodes used in the present study and in [1, 2] is the presence of a sharp emitting edge. In order to reveal the correlation of the band structure formed by charged-particle beams with this feature, we performed experiments with the diode, in which a smooth massive steel hemisphere was used as a high-voltage electrode (cathode). The diameter of the hemisphere was 28 mm, and its edges were rounded off (the rounding radius was 3 mm). The pat-

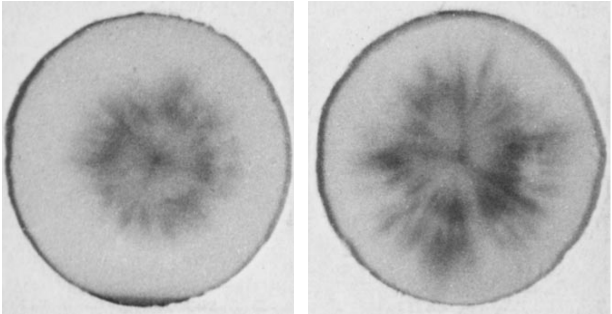

Fig. 2. Patterns of ion beams generated as a result of discharges in deuterium at $P = 0.3$ Torr and (left) $d = 2.5$ mm (20 pulses) and (right) $d = 5$ mm (35 pulses). The anode is a hollow thin-wall cylinder.

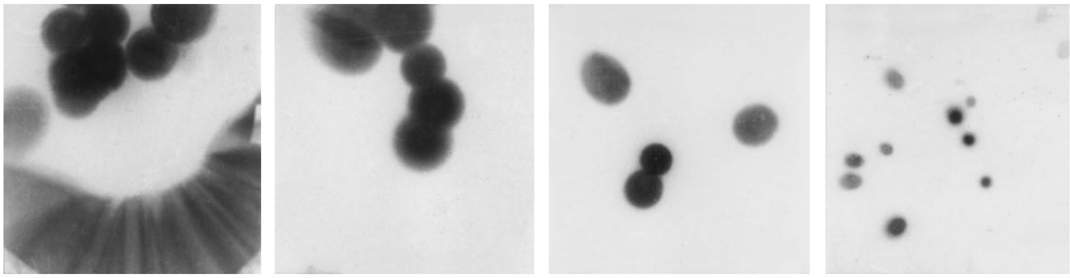

Fig. 3. Patterns of electron beams in the case of a cathode with the developed emitting surface (hemisphere 28 mm in diameter) for P = (from left to right) 0.04, 0.04, 0.3, and 1 Torr and Δ = (from left to right) 15, 30, 30, and 15 μm. The interelectrode spacing is d = 5 mm.

terns formed by electron beams for two values of aluminum-anode thickness Δ are shown in Fig. 3. In the case of $\Delta = 15$ and 30 μm, the film can be penetrated by electrons with an energy exceeding 50 and 80 keV, respectively. Several ectons spaced from each other arise on the spherical surface of the cathode, which are separated from each other by a certain distance. At P = 0.04 Torr, the diameter of the pattern formed by the electron beam emitted by one ecton is 5–6 mm, the beam angular divergence being close to 60°. With increasing P, this diameter decreases, which is caused by the gas focusing and attains 1–2 mm at P = 1 Torr. The pattern observed for the electron beam emitted from the rounded cathode edge exhibits a pronounced band structure. The electron energy in the beam does not exceed 80 keV, since this beam is absent beyond the anode with the thickness of 30 μm. It is possible that the pattern under discussion corresponds to the distribution of a set of ectons at the cathode edge. A similar distribution of ectons was observed for discharges in vacuum in the presence of an external magnetic field [3].

We can estimate the characteristic size r of plasma for the instant when the magnetic pressure of the explosive-emission electric current is equal to the gas-dynamic pressure of metal vapor: $r^5 \approx \dfrac{6M_1 t_{\mathrm{del}} kT}{\pi\mu_0 m_{\mathrm{n}} AC}$. Here, $M_1 \approx 10^{-11}$ g is the mass of metal evaporated from a single microscopic asperity [3] for the pulse duration ~10 ns [3]; $t_{\mathrm{del}} \sim 1$–10 ns is the explosion delay time; k is Boltzmann's constant; $T \approx 10^4$ K is the plasma temperature; μ_0 is the magnetic permittivity of vacuum; m_{n} is the nucleon mass; $A = 181$ is the tantalum atomic mass; and $C \approx 4 \times 10^{17}$ A^4 s m^{-4} [3]. The quantity r depends weakly on the empirical quantities M_1, t_{del}, T and is close to the characteristic size of about 1 μm of a single microscopic asperity. This implies the impossibility of the confluence of the explosive plasma into a unified layer at the cathode edge.

High-voltage nanosecond gas discharges at high overvoltages generate beams of accelerated electrons and ions. These beams have the same complicated ordered space–energy distribution as discovered previously for electron beams generated in high vacuum. It is possible that, in accordance with [1, 2], the spatial structure of the electron beams originates from ordered distribution of ectons along the emitting cathode edge. However, according to the above estimate, a mechanism that implies [1] the confluence of plumes of explosive plasma into a unified layer, which then breaks, seems to be nonphysical. The discovery of the ion-beam structure casts doubts on mechanisms of electron-beam formation, which are based on a regular distribution of ectons [1, 2]. Since the gas ionized by electrons is an ion source, the ion-beam structure is a consequence of the structure of the electron beams. However, the formation of an ordered distribution of ectons on the mesh cathode possessing high geometric transparency seems to be improbable. Most likely, the regular structure of charged-particle beams is a result of the filamentation of electron beams themselves. In addition, this filamentation is accompanied by the transformation of filaments into plane layers because of electrostatic expansion.

REFERENCES

1. A. J. Toepfer and L. P. Bradley, J. Appl. Phys. **43**, 3033 (1972).
2. L. P. Babich, N. G. Pavlovskaya, and S. L. Él'yash, Izv. Vyssh. Uchebn. Zaved., Radiofiz. **18** (5), 769 (1975).
3. G. A. Mesyats, *Ectons in Vacuum Discharge: Breakdown, Spark, Arc* (Nauka, Moscow, 2000).
4. L. P. Babich, T. V. Loĭko, and V. A. Tsukerman, Usp. Fiz. Nauk **160** (7), 49 (1990) [Sov. Phys. Usp. **33**, 521 (1990)].
5. L. P. Babich and T. V. Loĭko, Dokl. Akad. Nauk SSSR **313**, 846 (1990) [Sov. Phys. Dokl. **35**, 750 (1990)].
6. V. Ya. Averchenkov, L. P. Babich, T. V. Loĭko, *et al.*, Zh. Tekh. Fiz. **65** (5), 156 (1995) [Tech. Phys. **40**, 493 (1995)].
7. L. P. Babich, T. V. Loĭko, E. N. Donskoĭ, *et al.*, Prib. Tekh. Éksp., No. 4, 82 (2000).
8. G. I. Kir'yanov and S. V. Syromukov, Vopr. Atom. Nauki i Tekh., Ser. Radiats. Tekh., No. 2 (24), 53 (1982).

Translated by G. Merzon

Doklady Physics, Vol. 48, No. 9, 2003, pp. 490–494. Translated from Doklady Akademii Nauk, Vol. 392, No. 1, 2003, pp. 48–53.
Original Russian Text Copyright © 2003 by Kaplun, Meshalkin.

TECHNICAL PHYSICS

Equation of State for Dense Gases of One-Component Substances

A. B. Kaplun and A. B. Meshalkin

Presented by Academician V.E. Nakoryakov February 26, 2003

Received January 9, 2003

The thermodynamic properties of rarefied, low-density, and (in part) moderately dense gases are frequently described by the equations of state in the virial form [1–3]

$$Z = \frac{P\mu}{\rho RT} = 1 + B(T)\rho + C(T)\rho^2 + \dots . \qquad (1)$$

Here, Z is the compressibility factor; T is the temperature; P is the pressure; $\rho = \frac{1}{V}$ is the density, where V is the specific volume; R is the universal gas constant; μ is the molar mass of the substance; and $B(T)$, $C(T)$, etc., are the virial coefficients depending only on temperature. In principle, the virial coefficients can be calculated by the methods of statistical physics when the potentials of intermolecular interaction are known. However, since the actual interaction potentials are unknown (moreover, mathematical difficulties appear when realizing this approach), the exact equation of state with a reasonable number of virial coefficients can hardly be obtained. Purely empirical approaches without physical and theoretical concepts (see, e.g., [3–5]) also provide limited possibilities for obtaining the exact equations of state with a small number of parameters, because the described thermodynamic surface is intricate.

We prefer the approach where the functional form and structure of the equation of state can be obtained from physical concepts, while the particular form of analytical expressions and the numerical values of the parameters entering into these equations can be established from experimental data.

In this study, using the relationships and dependences found earlier in [6–8], we derive the equation of state that describes the thermal and caloric properties of rarefied, moderately dense, and dense gases of many “normal” substances within the experimental accuracy.

In [7], using a spherically symmetric step potential of intermolecular interaction, we derived the equation for the second virial coefficient $B(T)$ of nonpolar substances. Within the experimental accuracy, this equation reproduces the experimental data for numerous substances over the entire temperature interval under study [6, 7]. Therefore, one can hope that the use of such a potential to obtain the equation of state for gases in a wide interval of the state parameters can be successful.

This potential has the form (Fig. 1)

$$U(r) = \begin{cases} +\infty, & \text{for} \quad 0 < r < \sigma_0 \\ \beta, & \text{for} \quad \sigma_0 < r < \sigma \\ -\varepsilon, & \text{for} \quad \sigma < r < d \\ -\dfrac{c}{r^6}, & \text{for} \quad d < r, \end{cases} \qquad (2)$$

where r is the intermolecular distance. An interparticle interaction potential similar in form was previously

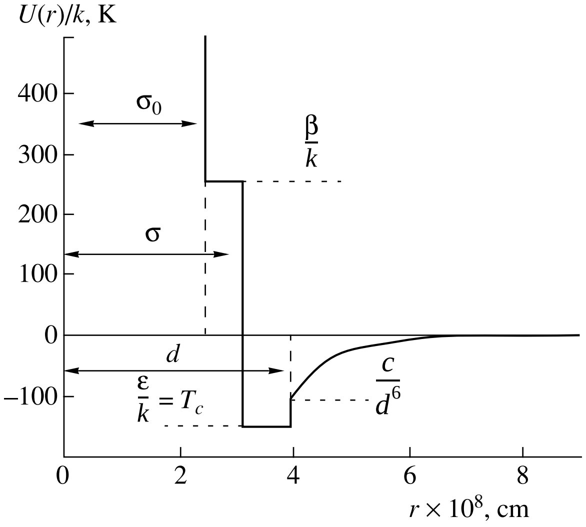

Fig. 1. Schematic representation of a combined model potential of the interparticle interaction.

Institute of Thermal Physics, Siberian Division, Russian Academy of Sciences, pr. Akademika Lavrent’eva 1, Novosibirsk, 630090 Russia
e-mail: kaplun@itp.nsc.ru

1028-3358/03/4809-0490$24.00 © 2003 MAIK “Nauka/Interperiodica”

proposed by Kreglewski [9]. Potential (2) can be represented as the sum of simple potentials:

$$U(r) = U_1(r) + U_2(r) + U_3(r) + U_4(r), \tag{3}$$

where

$$U_1(r) = \begin{cases} +\infty, & \text{for} \quad 0 < r < \sigma_0 \\ 0, & \text{for} \quad r > \sigma_0, \end{cases}$$

$$U_2(r) = \begin{cases} 0, & \text{for} \quad r < \sigma_0 \\ +\beta, & \text{for} \quad \sigma_0 < r < \sigma \\ 0, & \text{for} \quad r > \sigma, \end{cases}$$

$$U_3(r) = \begin{cases} 0, & \text{for} \quad r < \sigma \\ -\varepsilon, & \text{for} \quad \sigma < r < d \\ 0, & \text{for} \quad r > d, \end{cases} \tag{4}$$

$$U_4(r) = \begin{cases} 0, & \text{for} \quad r < d \\ -\dfrac{c}{r^6}, & \text{for} \quad r > d. \end{cases}$$

Of course, the equation of state could be found by the direct calculation of the partition function of the thermodynamic system, where the intermolecular interaction is described by potential (2), and subsequent passage to the thermodynamic quantities by using the known equations of statistical physics [1]. However, the realization of such an approach is rather complicated, requires a number of additional assumptions about the spatial distribution of particles, can hardly provide accurate results, and, for these reasons, is beyond the scope of this work.

In [7], using potential (3) and the known relationship

$$B(T) = -2\pi N_A \int_0^\infty \left(\exp\left(-\frac{U(r)}{kT}\right) - 1 \right) r^2 dr, \tag{5}$$

where N_A is the Avogadro constant and k is Boltzmann's constant, we obtained the equation

$$B(T) = b - c_2\left(\exp\left(-\frac{\beta}{kT}\right) - 1\right) - c_1\left(\exp\left(\frac{\varepsilon}{kT}\right) - 1\right) - \frac{A}{T} \tag{6}$$

for the second virial coefficients. Thus, as follows from Eqs. (5) and (6), the compressibility factor for low densities ($\rho \to 0$) as calculated by Eqs. (3) and (5) is equal to

$$Z_B = 1 + B(T)\rho = 1 + \sum_{i=1}^{4} B_i(T)\rho = 1 + \sum_{i=1}^{4} [Z_i(U_i) - 1]. \tag{7}$$

Similarly to Eq. (7), the compressibility factor of a gas in a wide density range can be written as

$$Z = 1 + \sum_{i=1}^{4} [Z_i(U_i) - 1] + \Delta Z(U). \tag{8}$$

The term $\Delta Z(U)$ can appear in the equation of state (8) after the determination of the partition function, which, after the calculation of the irreducible higher order (above second) integrals [1, 2] and subsequent calculations of the virial coefficients, can contain "crossed terms" from the interaction potentials $U_i(r)$ specified by Eqs. (4).

When calculating the compressibility factor by Eq. (8), one can assign a certain conventional thermodynamic subsystem to each $Z_i(U_i)$. Our calculation of the compressibility factor in a wide density range was based on the following concepts.

(i) A conventional thermodynamic subsystem where intermolecular interaction is represented by the potential $U_1(r)$ specified by the first of Eqs. (4) is a system of hard spheres where the compressibility factor is a function only of density ρ: $Z_1 = Z_{hs}(\rho)$. The explicit expression for $Z_{hs}(\rho)$ was given, e.g., in [5]. However, taking into account that molecules in the first approximation can represent hard ("impermeable") but nonspherical particles, one can generally write $Z_1 = f(\rho)$. As was shown in [8], the presence of such a term in the equation of state agrees with the preferred form of the equation of state resulting from the rigorous equations of thermodynamics.

(ii) When calculating the compressibility factor $Z_2 = Z_2(U_2)$, we took into account that the repulsive branch in the actual potential is very steep so that the width of an approximating step in Eq. (4) can be considered very small. In addition, one can assume that, in the range of distances $\sigma_0 < r < \sigma$ for moderate densities, no more than one or two particles can be simultaneously present near a chosen particle. This assumption makes it possible to calculate only the second and third virial coefficients when evaluating the compressibility factor $Z_2 = Z_2(U_2)$. The explicit expressions for these virial coefficients with the interaction potential $U_2(r)$ specified by the second of Eqs. (4) were given in [1, 2]. Thus, $Z_2 = Z_2(U_2)$ can be represented in the form

$$Z_2(U_2) = 1 - a_1\left(\exp\left(-\frac{\beta}{kT}\right) - 1\right)\rho - a_2\left(\exp\left(-\frac{\beta}{kT}\right) - 1\right)^2\rho^2. \tag{9}$$

(iii) To calculate the compressibility factor resulting from the intermolecular attraction forces $Z_3 = Z_3(U_3)$ and $Z_4 = Z_4(U_4)$, which are specified by the square-well potential and the dispersion London forces in the interaction potential (2), for densities at which it is impossible to neglect multiple collisions, we use the concept proposed in [3, 10]. According to this concept, the compressibility factor, according to generalization of the virial equation of state (1), is representable in terms of "elementary functions":

$$Z(T, \rho) = A_0(\rho) + \frac{A_1(\rho)}{T} + A_2(\rho)\Psi(T) + A_3(\rho)\Phi(T) + \dots. \tag{10}$$

Such a representation of the compressibility factor means that the temperature functions are independent of the spatial (density) functions and vice versa. When describing the third and fourth conventional thermodynamic subsystems, one can try to identify the temperature functions $\Psi(T)$, $\Phi(T)$, etc., in Eq. (10) with the second, third, etc., virial coefficients, respectively. Then, retaining only the term with the second virial coefficient in the equation of state, one can represent the compressibility factor in the form

$$Z_3(U_3) = 1 - a_3\left(\exp\left(\frac{\varepsilon}{kT}\right) - 1\right)\rho\varphi(\rho). \tag{11}$$

On the basis of the same argumentation, the compressibility factor Z_4 is written as

$$Z_4(U_4) = 1 - \frac{a_4}{T}(1 - b\psi(\rho))\rho = 1 - \frac{a_4}{T}\rho + \frac{a_5}{T}\rho\psi(\rho). \tag{12}$$

The representation of $Z_3 = Z_3(U_3)$ and $Z_4 = Z_4(U_4)$ in the form of Eqs. (11) and (12) provides the passage to the equation of state for a rarefied gas with the second virial coefficient if $\lim(\lim_{\rho \to 0}(\varphi(\rho)) = 1$ and $\lim(\lim_{\rho \to 0}(\psi(\rho)) = 1$.

Thus, in view of Eqs. (8), (9), (11), and (12), the equation of state of a real gas where the intermolecular interaction is described by potential (2) has the form [it is taken that $\Delta Z = 0$ in Eq. (8)]

$$Z = 1 + f(\rho) - a_1\left(\exp\left(-\frac{\beta}{kT}\right) - 1\right)\rho - a_2\left(\exp\left(-\frac{\beta}{kT}\right) - 1\right)^2\rho^2 - a_3\left(\exp\left(\frac{\varepsilon}{kT}\right) - 1\right)\rho\varphi(\rho) - \frac{a_4}{T}\rho + \frac{a_5}{T}\rho\psi(\rho). \tag{13}$$

The detailed analysis of the equation of state (13) using the experimental P–V–T data for numerous substances (in our calculations, we used the data from the series of monographs on the thermodynamic properties of materials published by GSSSD, Publishing House of Standards, Moscow) provide the following conclusions.

(i) In the temperature-dependent terms in Eq. (13), the optimum description of the experimental data is reached for

$$\beta = \varepsilon, \quad \frac{\beta}{k} = \frac{\varepsilon}{k} = T_c; \tag{14}$$

(ii) The function $f(\rho)$ has the form

$$f(\rho) = a_6\rho e^{\gamma\rho}; \tag{15}$$

(iii) The functions $\varphi(\rho)$ and $\psi(\rho)$ are equal to each other, i.e., $\varphi(\rho) = \psi(\rho)$; the function $\varphi(\rho)$ in the dimensionless form can be represented as a function of the reduced density $\omega = \frac{\rho}{\rho_c}$ and the compressibility factor at the critical point $Z_c = \frac{\mu P_c}{RT_c\rho_c}$ (P_c, T_c, and $\rho_c = \frac{1}{V_c}$ are the parameters of a material at the critical point) and has one fitting parameter c_0:

$$\varphi(\omega) = 1 - 2\omega + 3\left(\frac{1}{2} - Z_c\right)\omega^2 + 4\left(Z_c - \frac{1}{6} - Z_c^2\right)\omega^3 - c_0\omega^5. \tag{16}$$

Then, taking into account the above discussion, the equation of state (13) can be written in terms of the reduced variables $\omega = \frac{\rho}{\rho_c}$ and $\tau = \frac{T}{T_c}$ as

$$Z(\omega, \tau) = 1 - c_1\left(\exp\left(-\frac{1}{\tau}\right) - 1\right)\omega - c_2\left(\exp\left(-\frac{1}{\tau}\right) - 1\right)^2\omega^2 - c_3\left(\exp\left(\frac{1}{\tau}\right) - 1\right)\omega\varphi(\omega) - \frac{c_4}{\tau}\omega + \frac{c_5}{\tau}\omega\varphi(\omega) + c_6\omega e^{c_7\omega}, \tag{17}$$

where $\varphi(\omega)$ is determined by Eq. (16).

Detailed analysis shows that Eq. (17) describes the thermal properties of many normal materials in the density range $\rho = 0$–$1.5\rho_C$ ($\omega = 0$–1.5) within the accuracy of experimental (reference) data except the critical domain. In these calculations, we considered pressures from 1 to 500 bar and temperatures from the triple point to 500 K (for carbon dioxide and water, the upper limits were 1000 bar and 1000 K, respectively), because experimental data are either absent or not quite reliable beyond these intervals. It is interesting that Eq. (17) describes the thermal properties of water vapor (as is known, water is an anomalous substance) within the accuracy presented in the skeleton tables [11].

As an example, the critical parameters of some materials and the coefficients of Eq. (17) obtained by the processing of tabular (averaged) experimental data on the thermal properties of these materials are listed in Table 1. This table also presents the standard deviations σ_Z of the calculated values of the compressibility factor Z from the tabular values. In addition, Table 1 contains the standard deviations calculated by the eight-parameter Benedict–Webb–Rubin equation (σ_Z^{BWR}) [1, 3]. This equation is considered as one of the best equations of state with a small number of parameters and is often used to describe the thermal properties of many materials [12]. As is seen in Table 1, Eq. (17) reproduces the thermal properties of materials better than the Benedict–Webb–Rubin equation of state.

It is evident that the equation of state (17) for low densities goes over to the equation of state with the second virial coefficient [Eq. (6), see also [6, 7]]. As is seen in Fig. 2, Eq. (17) with the coefficients evaluated from the tabular data in the wide range of the state parameters reproduces the experimental data concerning the second virial coefficient of gases much better than the Benedict–Webb–Rubin equation.

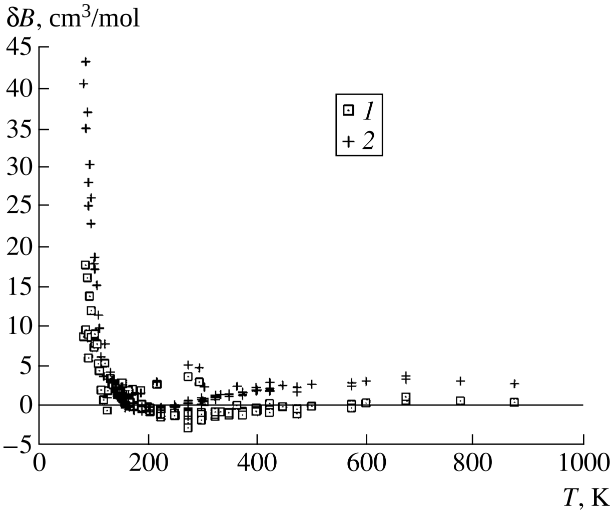

Fig. 2. Deviations $\delta B = B_{\text{calcd}} - B_{\text{exp}}$ of the calculated values of the second virial coefficient from the experimental values for argon [13]. The coefficients of equations are found from the thermal data for a dense gas [14] by (squares) Eq. (17) and (crosses) the Benedict–Webb–Rubin equation.

Using the known thermodynamic equations (see, e.g., [15]), one can obtain the equations describing the caloric properties of materials from the thermal equation of state if the properties in the ideal-gas state are known. Analysis shows that enthalpy and entropy calculated with the coefficients of Eq. (17) that are listed in Table 1 agree with the tabular data within the reference accuracies except the critical range (see Table 2). We emphasize again that enthalpy and entropy were calculated without data concerning the caloric properties of dense gases.

We think that the above approach has significant potential for further development and will possibly be

Table 1. Critical constants and parameters of Eq. (17) for some materials

Material	T_C, K	ρ_C, kg/m^3	Z_C	c_0	c_1	c_2	c_3	c_4	c_5	c_6	c_7	$\sigma_Z\times100$ by Eq. (17)	$\sigma_Z^{\text{BWR}}\times100$
Argon	150.86	531.0	0.2938	0.0473	1.0481	0	0.5022	2.0731	0.7089	0.4095	0.4718	0.126	0.216
Nitrogen	126.20	313.1	0.2899	0.0352	1.1590	0	0.5230	2.1896	0.7498	0.4409	0.4648	0.180	0.283
Oxygen	154.581	436.2	0.2878	0.0355	1.0287	0	0.5542	2.1159	0.7908	0.4449	0.4620	0.128	0.183
Methane	190.77	163.5	0.2862	0.0438	1.0309	0	0.5712	2.1103	0.7973	0.4381	0.4570	0.197	0.229
Carbon dioxide	304.20	467.99	0.2745	0.0472	1.6868	0.4410	0.9068	2.4576	1.2203	0.4377	0.5467	0.156	0.208
Tetrafluoromethane	227.5	629.7	0.2767	0.0471	1.0932	0.3319	0.7737	2.2728	1.0844	0.5774	0.4688	0.137	0.133
Water	647.27	317.763	0.2330	0.0367	1.5394	0	1.7296	2.6066	2.4723	0.5591	0.3291	0.314	0.329

Table 2. Calculated and tabular values of enthalpy and entropy for carbon dioxide

T, K	H, kJ/kg						S, kJ/(kg K)					
	10 bar	30 bar	70 bar	100 bar	200 bar	400 bar	10 bar	30 bar	70 bar	100 bar	200 bar	400 bar
280	$\frac{783.0}{782.5}$	$\frac{754.7}{754.2}$	– –	– –	– –	– –	$\frac{7.344}{4.337}$	$\frac{4.061}{4.055}$	– –	– –	– –	– –
305	$\frac{805.9}{805.5}$	$\frac{784.9}{783.9}$	$\frac{706.4}{709.6}$	– –	– –	– –	$\frac{4.422}{4.417}$	$\frac{4.165}{1.158}$	$\frac{3.791}{3.797}$	– –	– –	– –
350	$\frac{847.5}{847.2}$	$\frac{833.0}{832.2}$	$\frac{799.1}{797.7}$	$\frac{767.3}{766.1}$	$\frac{670.3}{669.5}$	– –	$\frac{4.548}{4.547}$	$\frac{4.310}{4.308}$	$\frac{4.077}{4.074}$	$\frac{3.937}{3.935}$	$\frac{3.589}{3.588}$	– –
400	$\frac{895.1}{894.8}$	$\frac{884.4}{883.9}$	$\frac{861.8}{860.9}$	$\frac{843.8}{842.7}$	$\frac{784.3}{782.9}$	$\frac{729.6}{728.3}$	$\frac{4.674}{4.676}$	$\frac{4.446}{4.448}$	$\frac{4.244}{4.244}$	$\frac{4.142}{4.142}$	$\frac{3.894}{3.894}$	$\frac{3.664}{3.664}$
600	$\frac{1100.4}{1100.3}$	$\frac{1096.2}{1096.0}$	$\frac{1087.9}{1087.8}$	$\frac{1081.9}{1081.7}$	$\frac{1063.4}{1063.0}$	$\frac{1036.1}{1035.4}$	$\frac{5.091}{5.086}$	$\frac{4.877}{4.872}$	$\frac{4.705}{4.699}$	$\frac{4.629}{4.623}$	$\frac{4.470}{4.464}$	$\frac{4.294}{4.288}$
1000	$\frac{1567.8}{1568.0}$	$\frac{1567.0}{1567.2}$	$\frac{1565.4}{1565.7}$	$\frac{1564.2}{1564.6}$	$\frac{1560.8}{1561.5}$	$\frac{1556.3}{1557.8}$	$\frac{5.682}{5.684}$	$\frac{5.473}{5.474}$	$\frac{5.310}{5.311}$	$\frac{5.240}{5.103}$	$\frac{5.102}{5.103}$	$\frac{4.957}{4.960}$

Note: Reference values [15] and calculation results are given above and under the horizontal bars, respectively.

able to considerably extend the described range of state parameters of one-component materials.

REFERENCES

1. J. O. Hirschfelder, C. F. Curtiss, and R. B. Bird, *Molecular Theory of Gases and Liquids* (Wiley, New York, 1954; Inostrannaya Literatura, Moscow, 1961).
2. E. A. Mason and T. H. Spurling, *The Virial Equation of State* (Pergamon Press, New York, 1969; Mir, Moscow, 1972).
3. G. A. Spiridonov and I. S. Kvasov, *Reviews on Thermophysical Properties of Substances* (Inst. Vys. Temp., Akad. Nauk SSSR, Moscow, 1986), No. 1 (57), pp. 45–117.
4. *Equations of State of Gases and Liquids*, Ed. by I. I. Novikov (Nauka, Moscow, 1975).
5. *Physics of Simple Liquids*, Ed. by H. Temperby, J. Roulinson, and G. Rushbrooke (North-Holland, Amsterdam, 1968; Mir, Moscow, 1971).
6. A. B. Kaplun and A. B. Meshalkin, High Temp., High Pressures **31**, 253 (1999).
7. A. B. Kaplun and A. B. Meshalkin, Russ. J. Eng. Thermophys. **10** (1), 65 (2000).
8. A. B. Kaplun and A. B. Meshalkin, Dokl. Akad. Nauk **376**, 624 (2001) [Dokl. Phys. **46**, 92 (2001)].
9. A. Kreglewski, *Equilibrium Properties of Fluids and Fluid Mixtures* (A&M Univ. Press, College Station (Tex.), 1984).
10. A. A. Vasserman, Ya. Z. Kazavchinskiĭ, and V. A. Rabinovich, *Thermophysical Properties of Air and Its Components* (Nauka, Moscow, 1966).
11. S. L. Rivkin and A. A. Aleksandrov, *Thermodynamic Properties of Water and Water Vapor* (Atomizdat, Moscow, 1984).
12. G. S. Soave, Fluid Phase Equilib. **164**, 157 (1999).
13. J. H. Dymond and E. B. Smith, *The Virial Coefficients of Gases: A Critical Compilation* (Clarendon Press, Oxford, 1969).
14. B. A. Rabinovich, A. A. Vasserman, V. I. Nedostup, and L. S. Veksler, *Thermal Properties of Neon, Argon, Krypton, and Xenon* (Izd. Standartov, Moscow, 1976).
15. V. V. Altunin, *Thermal Properties of Carbon Dioxide* (Izd. Standartov, Moscow, 1975).

Translated by Yu. Vishnyakov

Doklady Physics, Vol. 48, No. 9, 2003, pp. 495–498. Translated from Doklady Akademii Nauk, Vol. 392, No. 1, 2003, pp. 54–58.
Original Russian Text Copyright © 2003 by Myagkov.

TECHNICAL PHYSICS

Ultrafast Solid-State Reactions and Martensitic Transformations in Thin Films

V. G. Myagkov

Presented by Academician V.V. Osiko February 25, 2003

Received February 25, 2003

Ultrafast transformations and solid-state reactions are attracting constant current interest. In particular, shock-induced solid-state synthesis is responsible for the formation of reaction products with sizes d = 10–100 μm in $\tau = 10^{-5}$–10^{-7} s [1–4]. This corresponds to the extremely overestimated effective diffusion coefficient $D_{\text{eff}} \sim \dfrac{d^2}{4\tau} = 10^{-1}$–$10^{-5}$ m^2/s and contradicts the slow diffusion mechanism, which is the single explanation of mass transfer in the solid state. Various concepts in the framework of the diffusion mechanism were proposed to explain a high mobility of atoms in ultrafast synthesis. Disregarding the structure mechanism, Thadhani *et al.* [4] assumed for the first time that diffusionless cooperative processes must dominate in synthesis during the action of a shock wave. This assumption implies that mutual mass transfer responsible for the mixing of reagent atoms proceeds with velocity $V_r \sim 1$–1000 m/s.

Ultrafast (explosive) reactions also accompany solid-state synthesis in thin films [5–7]. The explosive behavior of the reaction in Ni/Si and Rh/Si substrate-free films was first thought to be determined by the explosive crystallization of Si amorphous layers. These reactions are initiated by local heating (due to mechanical impact, spark, or laser pulse) at room temperature. They propagate on the film surface as self-propagating self-similar waves. However, explosive reactions also proceed in fully polycrystalline Ni/Al films, which indicates that explosive reactions result from synthesis of Al and Ni layers. The front velocity in Ni/Al film samples is estimated as $V_r \sim 4$ m/s [7]. Ultrafast solid-state reactions include reactions initiated by nanosecond ($\tau \sim 10$ ns) laser annealing of thin films on substrates [8]. In this case, a reaction proceeds only in the irradiated area and does not propagate on the film surface. The typical thickness of films used in experiments is d = 10–100 nm. The effective diffusion coefficient is equal to $D_{\text{eff}} \sim \dfrac{d^2}{4\tau} = 10^{-8}$–$10^{-6}$ m^2/s for these reactions and is much higher than the diffusion coefficient in the solid phase. The velocity of reagents must be $V_r \sim 1$–10 m/s under the assumption of their diffusionless directed motion.

Since the mechanisms of solid-state synthesis are not clearly understood, it is impossible to predict the phase composition of reaction products and reagent pairs with which ultrafast synthesis can be realized.

The following two properties were found in [10–12].

(i) The first phase formed at the film interface is a phase with the minimum temperature T_K of the structural phase transition in the phase diagram.

(ii) The initiation temperature T_0 of a solid-phase reaction in thin films coincides with the minimum temperature of the solid-state structural phase transition of the first phase ($T_0 = T_K$).

In particular, a solid-state reaction in an S/Fe bilayer film starts at the temperature of the metal–dielectric phase transition in iron monosulphide (FeS), i.e., T_0(S/Fe) = T_K(FeS) [9]. For the Au–Cu system, which is classical in ordering, the initiation temperature in bilayer Cu/Au thin films was shown to be equal to the temperature of the order–disorder transition in a CuAu alloy, i.e., T_0(Au/Cu) = T_K(AuCu) [10].

Contrary to other solid-state transformations, martensitic transformations proceed through the diffusionless cooperative displacement of the high-symmetry austenite phase to the low-symmetry martensite phase. For this reason, it was surprising that martensitic transformations can determine solid-state reactions in thin films. In particular, NiTi and AuCd martensitic phases are formed by solid-state synthesis in Ni/Ti [11] and Cd/Au [12] bilayer films, respectively. The initiation temperature T_0 in these systems coincides with the martensitic transformation temperature T_K in NiTi and AuCd alloys, respectively, i.e., T_0(Ni/Ti) = T_K(NiTi) = 400 K and T_0(Cd/Au) = T_K(AuCd) = 340 K. However, up to a heating rate of 20 K/s, solid-state synthesis proceeds in Ni/Ti bilayer films and Cd/Au samples in the

*Kirenskiĭ Institute of Physics, Siberian Division,
Russian Academy of Sciences, Akademgorodok,
Krasnoyarsk, 660036 Russia
e-mail: miagkov@iph.krasn.ru*

reaction-diffusion mode and in the mode of self-propagating high-temperature synthesis (SHS), respectively. The above argumentation and analysis, made in [12], imply that solid-state reactions determined by martensitic transformations have common chemical and structural mechanisms with the diffusionless cooperative character of martensitic transformations. It is well known that martensitic transformations can be initiated at low temperatures, induced by external stresses, and proceed with high rates. These features suggest that solid-state reactions determined by martensitic transformations can change kinetics under the action of mechanical stresses, have the explosive mode, and proceed at cryogenic temperatures. As was shown in [12], solid-state reactions in Cd/Au layers proceed in the SHS mode and are determined by martensitic transformations in an AuCd alloy. Therefore, these samples are candidates for the initiation of ultrafast reactions.

In this paper, analyzing nanosecond ($\tau \sim 10$ ns) laser synthesis in Cd/Au(111) films, we show that the martensitic mechanism of atom transfer must dominate in ultrafast solid-state reactions in thin films.

The experiments were carried out with Cu/Au bilayer film samples obtained by sequential vacuum deposition on a freshly spalled MgO(001) surface. The typical thicknesses of Au and Cd layers were in the ranges 50–100 and 200–300 nm, respectively. To create good adhesion and form oriented layers on the MgO(001) surface, the first Au layer was deposited at 500–520 K in 10^{-4} Pa vacuum. To prevent a reaction, the upper Cd layer was deposited at room temperature. Figure 1a shows the diffraction pattern of the original Cd(200 nm)/Au(80 nm)/MgO(001) bilayer film samples. It exhibits reflections from the predominant Au(111) orientation and polycrystalline Cd layer. A sample can also contain negligible amounts of the Au(311) and Au(200) orientations. The original sample was heated at a rate of no less than 10 K/s until the appearance of an SHS wave, which was visually observed. Then, the sample was cooled at a rate of about 5 K/s. Figure 1b shows the diffraction pattern of Cd(200 nm)/Au(80 nm)/MgO(001) after the passage of the SHS wave. Reflections from the Cd layer disappear, and strong reflections corresponding to interplane spacings $d_1^1 = 0.229$ nm and $d_2^1 = 0.1145$ nm appear. Study of SHS in polycrystalline Cd/Au film samples [14] shows that these reflections can be attributed to the $\gamma'_2(111)$ and $\gamma'_2(222)$ martensitic peaks with the interplane spacings $d_1 = 0.2314$ nm and $d_2 = 0.11562$ nm (JCPDS card 26-0256), respectively. The difference between interplane spacings and tabulated values presents the dependence of the lattice constants of the γ'_2 martensite on the nonequilibrium synthesis conditions.

Samples of this set were also subjected to laser treatment in 10^{-4} Pa vacuum. Gaussian pulses with duration $\tau = 10$ ns and an energy of 0.15 J from an LTI-207 laser with $\lambda = 1.06$ μm, energy density $E_0 = 5$ J/cm^2, and an irradiation spot diameter of 1.7 mm were used. To analyze X-ray diffraction, the 8 × 8-mm film surface was scanned by a laser beam. The partial ablation and separation of the film from the substrate were observed after irradiation. Figure 2a shows the diffraction reflections after a single-pulse ($n = 1$) laser action. The diffraction pattern after $n = 4$ does not change. However, the intensities of reflections increase due to the growth of the layer of reaction products (Fig. 2b). Diffraction reflections from the reaction products after laser synthesis include only two peaks from (111) and (222) belonging to the γ'_2 martensite with interplane spacings $d_1^2 =$ 0.233 nm and $d_2^2 = 0.1165$ nm, respectively. The identity of diffraction patterns after the passage of the SHS wave (Fig. 1b) and after laser treatment (Fig. 2b) implies the same structural scenarios of atom transfer in both synthesis modes. The same conclusion was obtained when studying the formation of the $TiSi_2$ phase in Ti/Si(100) samples subjected to thermal annealing and nanosecond laser pulses [8]. The diffraction patterns from reacted samples (Figs. 1b, 2b) exhibit epitaxial relations $\gamma'_2(111) \parallel$ Au(111) of the γ'_2 martensite with the Au(111) film surface. The nonequilibrium synthesis process and epitaxial growth imply directional atom transfer during the reaction. Study of solid-state synthesis in polycrystalline Cd/Au samples shows that synthesis proceeds in the solid state [12]. This implies that synthesis on the oriented Au(111) surface is also solid-state synthesis. Either the shock wave or high temperature, which are induced by a laser pulse, can initiate synthesis in a Cd/Au(111) sample. The penetration depth δ_T of the thermal front can be estimated as $\delta_T \sim 2(\chi\tau)^{0.5}$, where $\chi(\mathrm{Cd}) = 0.5 \times 10^{-4}$ m^2/s is the thermal conductivity of cadmium. This estimate yields $\delta_T \approx 140$ nm, which is comparable with the thickness of the Cd layer in the original film. Under the assumption that the shock wave velocity is no less than the speed of sound, the depth of the shock wave action is estimated as $\delta > 10$ μm. The thickness of the reacted layer under the action of the temperature factor must be independent of the number of laser pulses. Therefore, the reaction initiation by the shock wave is more probable.

It is known (see, e.g., [13]) that the loss of the stability of the austenite β phase with a decrease in the sample temperature T_S to the start temperature M_S of the martensitic transformation is attributed to a decrease in the shear modulus $G' = \frac{1}{2}(C_{11} - C_{12}) \to 0$, which determines the stability of the structure under the $\{110\}\langle 110\rangle$ shear. The original interface of the Cd/Au sample is a two-dimensional reaction product (γ'_2 martensite). With an increase in temperature above the temperature A_S of the inverse martensitic transformation or under the action of a shock wave, the γ'_2 martensite transits to the β phase. Strong stresses cause reagent

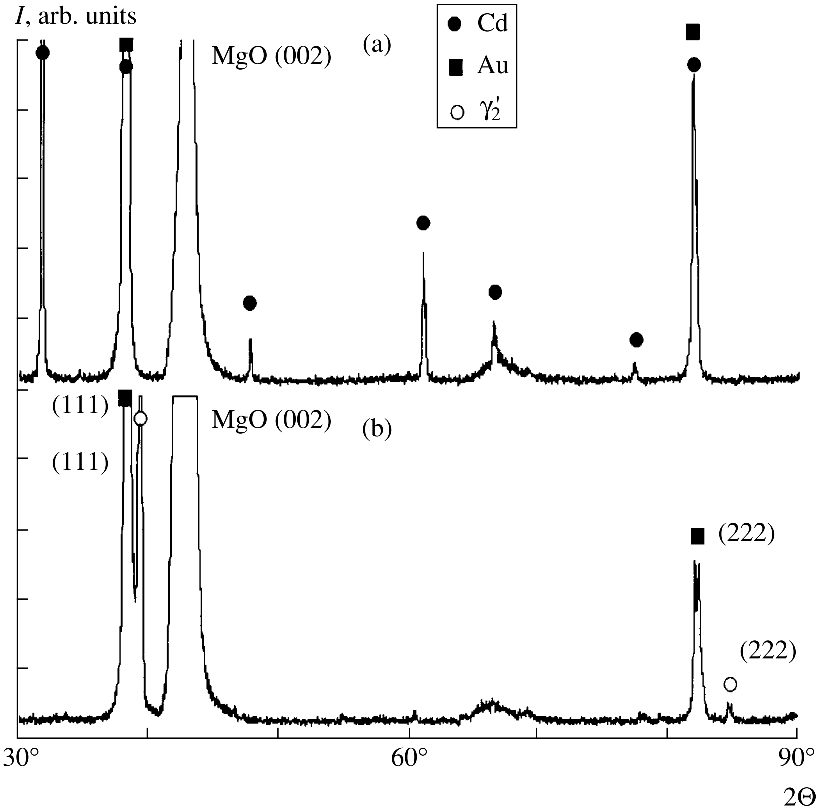

Fig. 1. Diffraction patterns of the Cd(200 nm)/Au(80 nm)/MgO(001) bilayer film system (a) before the reaction and (b) after the passage of the SHS wave through the original sample.

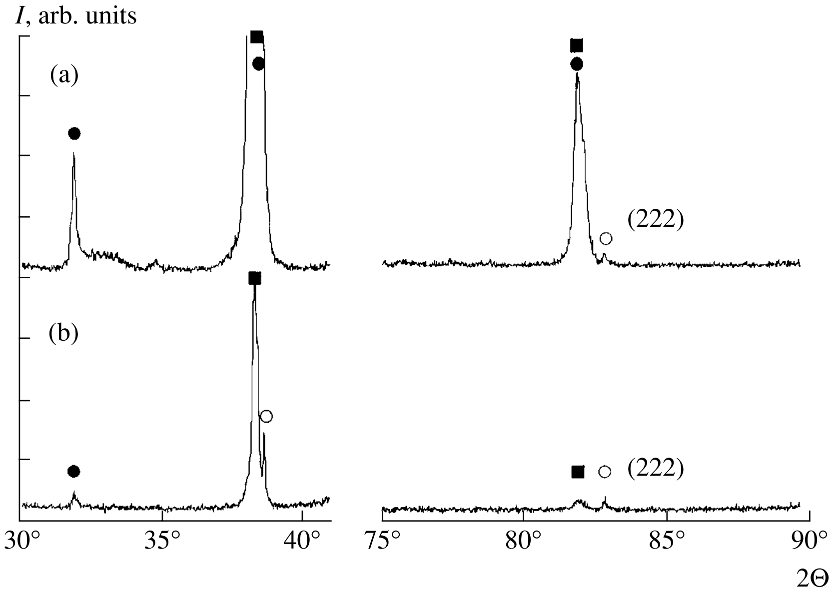

Fig. 2. Same as in Fig. 1 but after (a) single-pulse nanosecond (10 ns) laser action and (b) quadruple laser irradiation.

atoms to approach each other, reduce the activation energy, and promote the initiation of the reaction. Mass transfer in solid-state synthesis must proceed so that atoms cooperatively displace perpendicularly to the film plane in the nearest $\{110\}\langle 110\rangle$ direction of the β phase. Since the shear modulus G' is extremely low, the synthesis activation energy must be low, and the reaction must proceed in the ultrafast mode.

Since the classical works by Bridgman, it has been known that, under the simultaneous action of static pressure and shear deformation, chemical reactions can proceed in the explosive mode. In this case, the activation energy E_a is close to zero, the effective diffusion coefficient exceeds the diffusion coefficient in the solid state by a factor of 10^{10}–10^{12}, and temperature in the reaction zone does not considerably increase. The termination of the action of shear deformations gives rise to the sharp termination of many reactions [14]. This suggests that shear deformations are important in micromechanisms of reactions and their initiation. The determining role of shear deformations in the transition of reactions to the explosive mode was attributed by Teller [15] to low shear stresses compared to the compressive stresses, which is manifested as the smallness of shear modulus G compared to the elastic modulus E. Allowing $G \to 0$ at the martensitic point, our results strengthen the assumption made in [15] and justify the martensitic mechanism of ultrafast reactions.

In conclusion, we note that the proposed martensitic mechanism of synthesis suggests a method of prediction of ultrafast solid-state reactions. Shock-induced synthesis must first be realized with powder systems that have martensitic phases with a low martensitic point in the phase diagram. Therefore, shock synthesis in Ni–Al powder mixtures, which was observed in [3], must be determined by the martensitic transformation in the NiAl alloy ($M_S \sim 500$ K). In particular, synthesis under shock compression can be expected in powder systems Cd–Au ($M_S \sim 340$ K), Cd–Ag ($M_S \sim 300$ K), Ni–Ti ($M_S \sim 360$ K), etc.

ACKNOWLEDGMENTS

I am grateful to A.I. Poznyakov and V.S. Zhigalov for assistance in the laser annealing of the samples. This work was supported by the OAO MMK Foundation, Ausferr Engineering Center, and Intels Foundation for Science and Education (project no. 10-03-02).

REFERENCES

1. A. N. Dremin and O. N. Breusov, Usp. Khim. **37** (5), 898 (1968).
2. S. S. Batsanov, M. F. Gogulya, M. A. Brazhnikov, *et al.*, Khim. Fiz. **10** (12), 1699 (1991).
3. N. N. Thadhani, J. Appl. Phys. **76** (4), 2129 (1994).
4. N. N. Thadhani, R. A. Graham, T. Royal, *et al.*, J. Appl. Phys. **82** (3), 1113 (1997).
5. J. A. Floro, J. Vac. Sci. Technol. A **4** (3), 631 (1986).
6. L. A. Clevenger, C. V. Thomson, R. C. Cammarata, and K. N. Tu, Appl. Phys. Lett. **52** (10), 795 (1988).
7. E. Ma, C. V. Thomson, L. A. Clevenger, and K. N. Tu, Appl. Phys. Lett. **57** (12), 1262 (1990).
8. R. Larciprete, M. Danailov, A. Barinov, *et al.*, J. Appl. Phys. **90** (9), 5361 (2001).
9. V. G. Myagkov, L. E. Bykova, G. N. Bondarenko, *et al.*, Dokl. Akad. Nauk **371**, 763 (2000) [Dokl. Phys. **45**, 157 (2000)].
10. V. G. Myagkov, L. E. Bykova, G. N. Bondarenko, *et al.*, Pis'ma Zh. Éksp. Teor. Fiz. **71** (5), 268 (2000) [JETP Lett. **71** (5), 183 (2000)].
11. V. G. Myagkov, L. E. Bykova, L. A. Li, *et al.*, Dokl. Akad. Nauk **382**, 463 (2002) [Dokl. Phys. **47**, 95 (2002)].
12. V. G. Myagkov, L. E. Bykova, and G. N. Bondarenko, Dokl. Akad. Nauk **388**, 844 (2003) [Dokl. Phys. **48**, 30 (2003)].
13. H. Warlimont and L. Delaey, *Martensite Transformations in Cupper-, Silver- and Gold-Based Alloys* (Pergamon Press, Oxford, 1974; Nauka, Moscow, 1980).
14. N. S. Enikolopyan, Zh. Fiz. Khim. **63** (9), 2289 (1989).
15. E. Teller, J. Chem. Phys. **36** (4), 901 (1962).

Translated by R. Tyapaev

Doklady Physics, Vol. 48, No. 9, 2003, pp. 499–500. Translated from Doklady Akademii Nauk, Vol. 392, No. 2, 2003, pp. 183–184.
Original Russian Text Copyright © 2003 by Kharrasov, Kyzyrgulov, Iskhakov.

TECHNICAL PHYSICS

Exchange Enhancement of the Magnetoelastic Interaction in a LaMnO$_3$ Crystal

M. Kh. Kharrasov, I. R. Kyzyrgulov, and F. A. Iskhakov

Presented by Academician A.F. Andreev April 4, 2003

Received March 24, 2003

Investigation of the magnetoelastic interaction in perovskite structures is of both fundamental and applied interest. In these investigations, the effect of exchange enhancement of magnetoelastic coupling is particularly important. The essence of this effect consists in the fact that the relativistic magnetoelastic coupling in ferromagnets with a certain magnetocrystalline symmetry can be enhanced for some branches of phonon and spin excitations by the exchange interaction parameter and can considerably exceed the spin–phonon coupling in ferromagnets [1]. In addition, the study of the exchange enhancement due to the magnetoelastic interaction is of crucial importance for signal transformations.

In this study, we investigate a LaMnO$_3$ perovskite crystal (*Pnma* symmetry group). In the absence of an external magnetic field, the ground state of an antiferromagnetic subsystem of the crystal under consideration is determined by four magnetic sublattices (Fig. 1).

The magnetic moments of the crystal do not lie in the basal plane, because LaMnO$_3$ has a distorted perovskite structure [2–7]. The rotation of the magnetic moments because of the lattice distortion is shown in Fig. 2.

Let us consider the interaction between spin and elastic waves in a LaMnO$_3$ orthorhombic crystal with long-range antiferromagnetic order and find the conditions under which the magnetoelastic coupling can be enhanced due to the exchange interaction of magnetic moments in sublattices. We take a phenomenological Hamiltonian representing a sum of the energies of the magnetic and elastic parts of the system, as well as the energy of their interaction [8, 9]:

$$H = H_{\mathrm{m}} + H_{\mathrm{e}} + H_{\mathrm{me}}. \qquad (1)$$

Here, the uniform exchange interaction, anisotropy, nonuniform exchange interaction, and magnetostriction are taken into account.

The secondary quantization method and Bogoliubov canonical transformations [10] reduce Hamiltonian (1) to the diagonal form

$$H_M = \sum_{k\gamma} \varepsilon^M_{k\gamma} \overset{+}{c}_{k\gamma} c_{k\gamma} + \sum_{ks} \varepsilon^U_{ks} \overset{+}{b}_{ks} b_{ks} + \left[\sum_{ks,\,\gamma'} \Psi_{k\gamma' s} c_{k\gamma'} (b_{-ks} - \overset{+}{b}_{ks}) + \mathrm{H.c.} \right], \qquad (2)$$

where $\varepsilon^M_{k\gamma}$ and ε^U_{ks} are the energies of the spin and sound waves, respectively, and $\Psi_{k\gamma s}$ is the magnetoelastic interaction parameter ($\gamma = 1, 2, 3$, and 4 and $s = l, t_1$, and t_2). It is seen in Fig. 3 (dashed lines) that the spin and sound waves have four and three branches, respectively.

Investigations of the magnetoelastic interaction show that the parameters Ψ_{k1t1}, Ψ_{k1t2}, Ψ_{k2t1}, Ψ_{k2t2}, Ψ_{k3l}, Ψ_{k4t1}, and Ψ_{k4l} for a wave propagating in the z-axis direction are equal to zero. The coupling Ψ_{k3t1} between the third and fourth spin branches, as well as the coupling Ψ_{k4t2} between the first and second transverse branches, is enhanced by the exchange interaction [11, 12].

For $\mathbf{k} \parallel \mathbf{Y}_0$, the coupling parameters Ψ_{k1t1}, Ψ_{k2t1}, Ψ_{k2t2}, Ψ_{k3t2}, Ψ_{k3l}, Ψ_{k4t2}, and Ψ_{k4l} are equal to zero. In this case, the coupling between the first spin branch and the second transverse sound branch Ψ_{k1t2} is enhanced by the exchange interaction.

For $\mathbf{k} \parallel \mathbf{X}_0$, the coupling parameters Ψ_{k1t2}, Ψ_{k2t1}, Ψ_{k2t2}, Ψ_{k3t1}, Ψ_{k3l}, Ψ_{k4t1}, Ψ_{k4t2}, and Ψ_{k4l} are equal to zero.

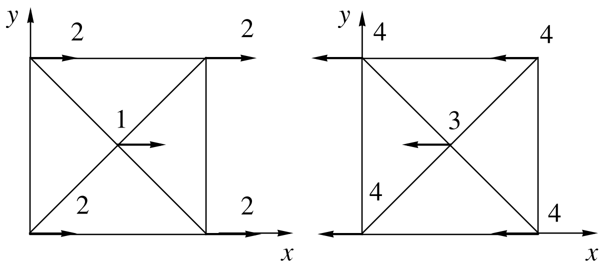

Fig. 1. Direction of the magnetic moments.

Faculty of Physics, Bashkortostan State University,
ul. Frunze 32, Ufa, 450074 Bashkortostan, Russia
e-mail: iafanur@mail.ru

1028-3358/03/4809-0499$24.00 © 2003 MAIK “Nauka/Interperiodica”

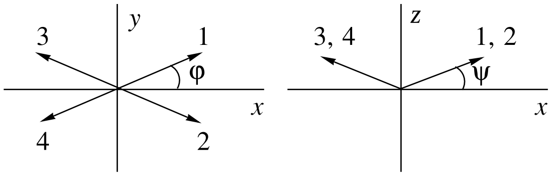

Fig. 2. Rotation of the magnetic moments.

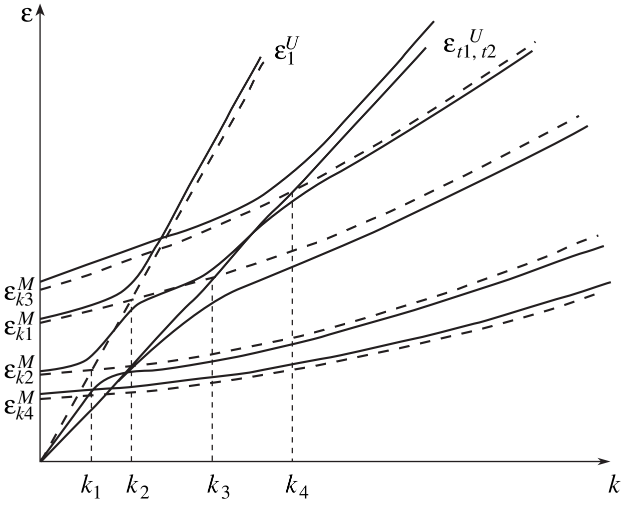

Fig. 3. Spectrum of the coupled magnetoelastic waves.

In this case, the coupling between the first spin branch and the first transverse sound branch Ψ_{k1t1} is enhanced by the exchange interaction.

To find the natural frequencies (coupled magnetoelastic waves), we use the equations of motion for the secondary quantization operators. Retaining the terms up to the second power in the coupling coefficients, we arrive at the dispersion relation

$$\prod_{\gamma}\prod_{s}(\omega^2-\varepsilon_{k\gamma}^{M^2})(\omega^2-\varepsilon_{ks}^{U^2})$$

$$-4\sum_{\gamma s}|\Psi_{k\gamma s}|^2\varepsilon_{k\gamma}^M\varepsilon_{ks}^U\prod_{\substack{\gamma'\neq\gamma\\ s'\neq s}}(\omega^2-\varepsilon_{k\gamma'}^{M^2})(\omega^2-\varepsilon_{ks'}^{U^2}) = 0.$$

The spectrum of coupled magnetoelastic waves propagating along the x axis is shown in Fig. 3, where $k_i \simeq 10^6$ m^{-1} and $\varepsilon_{k\gamma}^M \simeq 10^{12}$ s^{-1}.

Our calculations indicate that the variations in the spectral gap that are attributed to the distortion of the perovskite structure are equal to

$$\frac{\left|\varepsilon_1^{M(\mathrm{dist})}-\varepsilon_1^{M(\mathrm{undist})}\right|}{\varepsilon_1^{M(\mathrm{dist})}} = 0.03,$$

$$\frac{\left|\varepsilon_2^{M(\mathrm{dist})}-\varepsilon_2^{M(\mathrm{undist})}\right|}{\varepsilon_2^{M(\mathrm{dist})}} = 0.18,$$

$$\frac{\left|\varepsilon_3^{M(\mathrm{dist})}-\varepsilon_3^{M(\mathrm{undist})}\right|}{\varepsilon_3^{M(\mathrm{dist})}} = 0.11,$$

$$\frac{\left|\varepsilon_4^{M(\mathrm{dist})}-\varepsilon_4^{M(\mathrm{undist})}\right|}{\varepsilon_4^{M(\mathrm{dist})}} = 0.02,$$

i.e., the distortion of the perovskite structure considerably affects the gap in the spin-wave spectrum.

Thus, we have developed the theory of the magnetoelastic interaction in perovskite structures with orthorhombic symmetry. The dispersion relation for determining the spectrum of coupled magnetoelastic waves has been derived. The magnetoelastic interaction has been analyzed as a function of the wave-propagation direction. The effect of structure distortion on the parameters of the magnetoelastic interaction was considered. It was shown that the dynamic magnetoelastic interaction between low-lying magnon modes and some phonon modes can be enhanced under certain conditions by the exchange-interaction parameter, which is important for signal transformations.

REFERENCES

1. M. A. Savchenko, Fiz. Tverd. Tela (Leningrad) **6**, 864 (1964) [Sov. Phys. Solid State **6**, 666 (1964)].
2. G. Matsumoto, J. Phys. **29**, 606 (1970).
3. E. O. Wollan and W. C. Koehler, Phys. Rev. **100**, 545 (1955).
4. F. Moussa, M. Hennion, J. Rodriguez-Carvajal, *et al.*, Phys. Rev. B **54**, 15149 (1996).
5. P. Norby, I. G. K. Andersen, and E. K. Andersen, J. Solid State Chem. **119**, 191 (1995).
6. J. Rodriguez-Carvaja, M. Hennion, F. Moussa, *et al.*, Phys. Rev. B **57**, 3189 (1995).
7. L. E. Gonchar, A. E. Nikiforov, and S. É. Popov, Zh. Éksp. Teor. Fiz. **118**, 1411 (2000) [JETP **91**, 1221 (2000)].
8. S. V. Tyablikov, *Methods in the Quantum Theory of Magnetism* (Plenum, New York, 1967; Nauka, Moscow, 1975).
9. T. Holstein and H. Primakoff, Phys. Rev. **58**, 1098 (1940).
10. N. N. Bogolyubov, Jr., B. I. Sadovnikov, and A. S. Shumovskiĭ, *Mathematical Methods in Statistical Mechanics of Model Systems* (Nauka, Moscow, 1975).
11. M. Kh. Kharrasov and A. U. Abdullin, Dokl. Akad. Nauk **336**, 335 (1994) [Phys.-Dokl. **39**, 346 (1994)].
12. M. Kh. Kharrasov and I. R. Kyzygulov, Dokl. Akad. Nauk **373**, 188 (2000) [Dokl. Phys. **45**, 327 (2000)].

Translated by Yu. Vishnyakov

Doklady Physics, Vol. 48, No. 9, 2003, pp. 501–504. Translated from Doklady Akademii Nauk, Vol. 392, No. 3, 2003, pp. 332–335.
Original Russian Text Copyright © 2003 by Afanas'ev, Pustovoĭt.

TECHNICAL PHYSICS

Wave Diffraction on a Periodic Structure with an Arbitrary Spatial Variation of the Medium's Properties

Corresponding Members of the RAS A. M. Afanas'ev and V. I. Pustovoĭt

Received April 22, 2003

High-contrast wave filters are urgently required for solving many problems of optics, radio engineering, acoustics, and X-ray spectral analysis. These filters must strongly suppress incident radiation beyond a certain given frequency band and, vice versa, possess a maximum radiation transmission within this band.

Nowadays, methods of spectral selection, which are based on the phenomenon of wave diffraction in media with spatially periodic variation of their properties, are widely used. Problems related to wave propagation and diffraction on periodic structures have been thoroughly investigated in the literature for acoustic waves (see monograph [1]) and visible light [2, 3]. In the latter publications, various types of optical filters based on such periodic structures were also considered. The simplest acoustic medium is realized just in acousto-optical filters. The acoustic wave causes modulation of the medium permittivity $\varepsilon(x, t)$. The modulation period is determined by the wave vector q of the sound wave, and the Fourier expansion of $\varepsilon(x)$ contains only one component [2]:

$$\varepsilon(x, t) = \varepsilon_0 + \Delta\varepsilon(x)\cos(\Omega t - qx), \qquad (1)$$

where Ω is the sound-wave frequency. The correction factor $\Delta\varepsilon(x)$ is determined in terms of photo-elasticity coefficients and is proportional to the sound-wave amplitude. At the same time, if $\Omega = 0$ and $q \neq 0$, then formula (1) describes a usual static stratified structure.

Diffraction filters make it possible to realize a high reflection factor on the order of unity in an extremely narrow spectral region (Fig. 1), which forms a base for their wide application. However, alongside the evident advantages of these spectrometers, there exist a number of undesirable properties whose elimination could qualitatively improve the characteristics of diffraction filters. First of all, there is the presence of far-propagating oscillations on the reflection curve tails, in which a noticeable portion of incident radiation energy is contained. As is easy to understand, this hampers analysis of weak spectral lines.

In the present paper, we demonstrate that it turns out to be possible to substantially improve the situation at the expense of smooth variation of the quantity $\Delta\varepsilon(x)$ as a function of x (apodization). In this case, we manage not only to avoid the oscillations but to suppress to a great extent the tails of the diffraction reflection curves, a high reflection coefficient in the central part of the filter being preserved. In other words, the requirements on the function $\Delta\varepsilon(x)$ are formulated, which allows filters for acoustic and visible-light waves, which have an almost Π-shaped characteristic, to be realized.

Substituting expression (1) for $\varepsilon(x, t)$ into Maxwell's equations and taking into account the synchronism conditions, we arrive at the well-known system of shortened equations for amplitudes of the incident (E_1) and diffracted backward (E_2) waves (see, e.g., [2]):

$$\frac{dE_1}{dx} = ik_0\Delta\varepsilon(x)e^{-i\Delta kx}E_2,$$
$$\frac{dE_2}{dx} = -ik_0\Delta\varepsilon(x)e^{i\Delta kx}E_1. \qquad (2)$$

Here, $E_1(x)$ and $E_2(x)$ are the amplitudes of incident

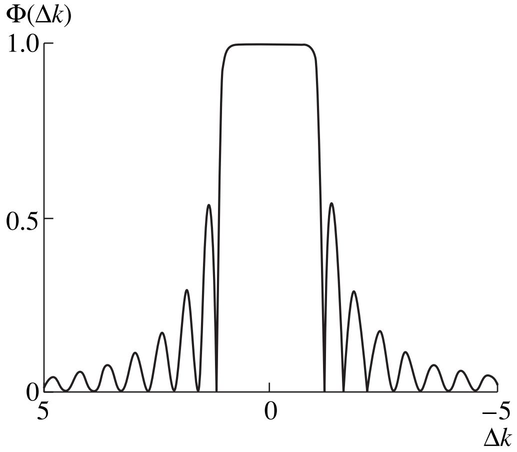

Fig. 1. Reflection coefficient for an ideal periodic structure of a finite size ($\Gamma = 0.5$ cm^{-1}; $L = 10$ cm).

Institute of Physics and Technology,
Russian Academy of Sciences,
Nakhimovskiĭ pr. 34, Moscow, 117218 Russia

Research and Technology Center of Unique Instrumentation,
Russian Academy of Sciences,
ul. Butlerova 15, Moscow, 117342 Russia

and diffracted waves, respectively; k_0 is the radiation wave number for which the condition of the exact synchronism is valid; and Δk determines the deviation from the Bragg synchronism condition. If $\Delta\varepsilon(x)$ is independent of x, then system of equations (2) has the following solution:

$$\Phi(\Delta k) = \left|\frac{E_2(0)}{E_1(0)}\right|^2$$
$$= \left|\frac{\sinh\left(\frac{\Gamma L}{2}\sqrt{1-\xi^2}\right)}{(1-\xi^2)\cosh\left(\frac{\Gamma L}{2}\sqrt{1-\xi^2}\right) + i\xi\sinh\left(\frac{\Gamma L}{2}\sqrt{1-\xi^2}\right)}\right|^2, \tag{3}$$

$$\Gamma = k_0\Delta\varepsilon, \quad \xi = \frac{\Delta k}{\Gamma}. \tag{4}$$

Here, $E_1(0)$ and $E_2(0)$ are, respectively, the amplitudes of incident and diffracted waves on the input surface of a crystal, and L is the interaction length. In Fig. 1, the function $\Phi(\Delta k)$ is presented for a filter with a constant $\Delta\varepsilon(x)$ and with parameters $\Gamma = 0.5$ cm^{-1} and $L = 10$ cm in accordance with formula (3).

In [4–6], indications were obtained that the existence of the dependence of polarizability $\Delta\varepsilon(x)$ on the x coordinate resulted in a decrease in the magnitude of subsidiary maxima. However, all these cases were restricted by a dependence $\Delta\varepsilon(x)$ such that analytical solutions to Eqs. (2) could be found. In these cases, noticeable suppression of undesirable oscillations was possible. Nevertheless, rather extended tails remained on the reflection curve, so it is still unclear whether methods of their efficient elimination do exist.

As is easy to immediately obtain from Eqs. (2) for the tails of the reflection curves, in the case that

$$|\Delta k| \gg \Gamma, \quad \Gamma = k_0\max(\Delta\varepsilon(x)), \tag{5}$$

there exists the following simple expression for the amplitude $R(\Delta k) = \dfrac{E_2(0)}{E_1(0)}$ of the reflected wave:

$$R(\Delta k) = k_0\int_0^L \Delta\varepsilon(x)\exp(i\Delta kx)dx. \tag{6}$$

Integral (6) can be taken by parts. As a result of this procedure, we have

$$R(\Delta k) = \frac{k_0(\Delta\varepsilon(L)\exp(i\Delta kL) - \Delta\varepsilon(0))}{i\Delta k}$$
$$- \frac{k_0}{i\Delta k}\int_0^L \frac{d\Delta\varepsilon(x)}{dx}\exp(i\Delta kx)dx. \tag{7}$$

Continuing the procedure of integrating by parts, we easily obtain

$$R(\Delta k) = F(L)\exp(i\Delta kL) - F(0), \tag{8}$$

where

$$F(x) = k_0\sum_0^{\infty}\frac{\Delta\varepsilon^{(n)}(x)}{(-i\Delta k)^{n+1}}, \quad \Delta\varepsilon^{(n)}(x) \equiv \frac{d^n\Delta\varepsilon(x)}{dx^n}. \tag{9}$$

Formulas (7)–(9) make it possible to formulate the necessary conditions for suppressing influence function wings, as well as for eliminating the oscillations. As follows from formula (7), first of all, it is necessary to form the profile of the function $\Delta\varepsilon(x)$ in such a manner that

$$\Delta\varepsilon(0) = 0, \quad \Delta\varepsilon(L) = 0. \tag{10}$$

If even one of conditions (10) is invalid, then, at high values of $|\Delta k|$, the reflection amplitude drops according to the law

$$R(\Delta k) \propto \frac{\Gamma}{\Delta k}. \tag{11}$$

In this case, the reflection coefficient decreases as

$$\Phi(\Delta k) \propto \frac{\Gamma^2}{(\Delta k)^2}. \tag{12}$$

As immediately follows from formulas (8) and (9), in the case that conditions (10) are valid, a considerably sharper decrease of the reflection coefficient occurs. In this case, instead of formula (12), we arrive at

$$\Phi(\Delta k) \propto \frac{\Gamma^2}{(\Delta k)^2}\frac{1}{(\Delta kL)^2}. \tag{13}$$

If, alongside the validity of conditions (12), we provide that the first derivatives of $\Delta\varepsilon(x)$ vanish, then $\Phi(\Delta k) \propto \dfrac{1}{(\Delta k)^6}$. Additional vanishing of the second derivatives leads to the dependence $\Phi(\Delta k) \propto \dfrac{1}{(\Delta k)^8}$. Thus, choosing the profile of the function $\Delta\varepsilon(x)$, we can suppress the reflection coefficient wings as strongly as is wished.

Formula (6) describes the reflection amplitude only at high values of $|\Delta k|$. Therefore, for calculating the main peak, i.e., for $|\Delta k| \leq \Gamma$, we should return to the initial set of equations (2). In the case of $\Delta k = 0$, there is a simple solution for an arbitrary dependence of $\Delta\varepsilon(x)$:

$$\Phi(0) = \left(\frac{1 - e^{-\bar{\Gamma}L}}{1 + e^{-\bar{\Gamma}L}}\right)^2, \tag{14}$$

where

$$\bar{\Gamma} = \Gamma\frac{1}{L}\int_0^L \Delta\varepsilon(x)dx. \tag{15}$$

As follows from relationship (15), choosing the interaction length L and the averaged (with respect to L) value of $\Delta\varepsilon(x)$, we can provide relatively large values of the product $\bar{\Gamma} L$. Thereby, in accordance with formula (14), we can have the reflection coefficient $\Phi(0)$ as close to unity as is wished. Large values of the product $\bar{\Gamma} L$ by no means contradict conditions (10). Hence, we can obtain the function $\Phi(\Delta k)$, whose values are close to unity at the center of the curve, and the wings are strongly suppressed.

For an arbitrary function $\Delta\varepsilon(x)$, set of equations (2) has no analytical solution; therefore, it is necessary to use numerical methods for calculating $\Phi(\Delta k)$. In the case under consideration, it is convenient to employ the so-called recurrence method, widely used in the physics of X-ray diffraction (see, e.g., [7] and references therein). According to this method, the crystal is divided into N layers (Fig. 2), and, in accordance with Eqs. (2), the amplitude $R^{(k)}$ of the reflection from first k layers is associated with the amplitude $R^{(k-1)}$ of the reflection from preceding $k - 1$ layers:

$$R^{(k)} = r_k + \frac{R^{(k-1)}}{1 - r_k^* R^{(k-1)}}. \qquad (16)$$

Here,

$$r_k = -i\Delta\varepsilon(x_k) e^{-i\Delta k x_k}\Delta x, \quad x_k = \frac{k}{N}L, \qquad (17)$$
$$k = 0, 1, \ldots, N,$$

is the amplitude of reflection by the separate kth layer, and $\Delta x = \frac{L}{N}$. This is the amplitude $R^{(N)}$ that corresponds to the desired quantity determining the reflection coefficient

$$\Phi(\Delta k) = \left|R^{(N)}\right|^2. \qquad (18)$$

In Fig. 3, the reflection curve calculated according to recurrence formulas (16), (17) is presented. This curve is calculated for the case

$$\Delta\varepsilon(x) = 2\Delta\varepsilon \sin^2\frac{\pi x}{L}. \qquad (19)$$

Function (19) satisfies conditions (10) and also conditions

$$\Delta\varepsilon'(0) = \Delta\varepsilon'(L). \qquad (20)$$

Therefore, for this dependence, we can expect a strong suppression of the reflection curve wings. As is seen in Fig. 3, these expectations are fully confirmed by direct calculations. The response function $\Phi(\Delta k)$ has an almost Π-shaped form.

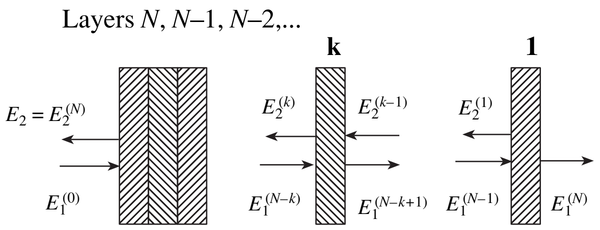

Fig. 2. Scheme clarifying the derivation of recurrence relationships.

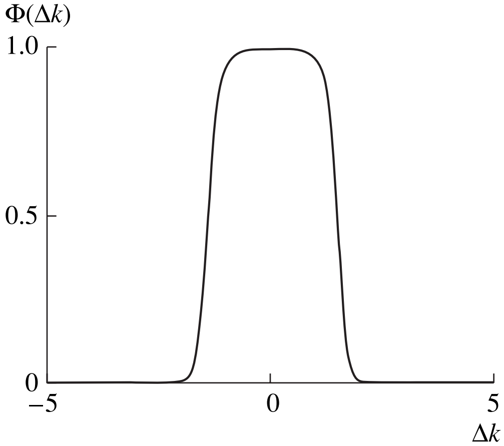

Fig. 3. Reflection curves for periodically apodizied structures with the function $\Delta\varepsilon(x) = 2\Delta\varepsilon \sin^2\frac{\pi x}{L}$; $\Gamma = 0.7$; $L = 10$ cm.

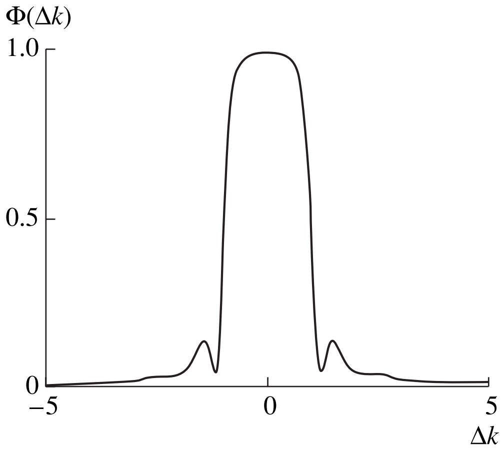

Fig. 4. Reflection curves for the functions $\Delta\varepsilon(x) = \left(\frac{\sin y}{y}\right)^2$; $\Gamma = 0.9$; $L = 10$ cm.

Figure 4 exhibits the results of calculations of $\Phi(\Delta k)$ for another case when

$$\Delta\varepsilon(x) = \left(\frac{\sin y}{y}\right)^2, \quad y = 2\pi\left(\frac{x}{L} - \frac{1}{2}\right). \qquad (21)$$

For such a dependence of $\Delta\varepsilon(x)$, conditions (10) and (18) are also valid, and suppression of the reflection curve wings is also observed. However, the comparison of curves in Figs. 3 and 4 shows that the wing suppression is not so strong in the latter case.

We can be simply convinced that the functions described by formulas (19) and (21) differ negligibly within the interval from 0 to L. However, we reveal the significant difference between them by turning to the series generated by these functions (9). As can be easily shown for function (19), the series $F(x)$ converges as $|\Delta k|L > 2\pi$. At the same time, the series $F(x)$ generated by function (21) diverges at an arbitrary Δk, and we should understand formula (9) only as an asymptotic series, i.e.,

$$F(x) = k_0 \sum_0^n \Delta\varepsilon^{(n)}(x) \frac{1}{(-i\Delta k)^n} + O\left(\frac{1}{k^{n+1}}\right). \qquad (22)$$

Thus, for strong suppression of the wings, alongside the validity of conditions (10) and (18), it is desirable to choose the function $\Delta\varepsilon(x)$ in such a manner that series (9) converges in a certain region $|\Delta k| > \Delta k_0$.

In the present paper, we gave the basic attention to optical filters, for which the permittivity has the simplest form (1). However, there are arguments in favor of the possibility of applying the results obtained to other types of radiation, which include radio waves in the microwave region, acoustic waves, and X-rays, as well as visible light propagating in optical waveguides. The last case is of special interest from the standpoint of application in practice.

REFERENCES

1. L. M. Brekhovskikh, *Waves in Layered Media* (Akad. Nauk SSSR, Moscow, 1957; Academic, New York, 1960).
2. P. Yeh, A. Yariv, and C. S. Hong, J. Opt. Soc. Am. **67**, 423 (1977).
3. A. Yariv and P. Yeh, *Optical Waves in Crystals. Propagation and Control of Laser Radiation* (Wiley, New York, 1984; Mir, Moscow, 1986), Chap. 6.
4. E. G. Anan'ev and V. I. Pustovoĭt, Fiz. Tverd. Tela (Leningrad) **29**, 1214 (1987) [Sov. Phys. Solid State **29**, 692 (1987)].
5. S. K. Yao and C. S. Tsai, Appl. Opt. **16** (11), 3032 (1997).
6. V. I. Pustovoĭt, Dokl. Akad. Nauk **365**, 39 (1999) [Dokl. Phys. **44**, 132 (1999)].
7. A. M. Afanas'ev, M. A. Chuev, R. M. Imamov, *et al.*, Kristallografiya **42** (3), 514 (1997) [Crystallogr. Rep. **42**, 467 (1997)].

Translated by G. Merzon

Doklady Physics, Vol. 48, No. 9, 2003, pp. 505–508. Translated from Doklady Akademii Nauk, Vol. 392, No. 3, 2003, pp. 336–339.
Original Russian Text Copyright © 2003 by Golovin, Iunin, Tyurin.

TECHNICAL PHYSICS

Strain-Rate Sensitivity of the Hardness of Crystalline Materials under Dynamic Nanoindentation

Yu. I. Golovin*, Yu. L. Iunin, and A. I. Tyurin***

Presented by Academician Yu.A. Osip'yan February 5, 2003

Received March 28, 2003

The coefficients of the strain-rate sensitivity of plastic characteristics (including microhardness) carry useful information concerning the nature of elementary carriers of plastic deformation and their mobility in a solid. In macrotests of various ductile materials (see, e.g., [1]), a wide range of strain rates $\dot{\varepsilon}$ (between 10^{-8} and 10^{6} s^{-1}) was investigated. However, fracture of many brittle materials (in particular, single crystals with covalent bonds, ceramics, glasses, etc.) begins before noticeable plastic strain. The plastic properties of such materials are usually studied by the methods of local deformation or microindentation. In recent years, the method of nanoindentation has also been extensively used in this field [2–4]. Famous firms (MTS, Micromaterials, CSEM, Hysitron, etc.) produce commercial nanotesters only for small $\dot{\varepsilon}$ values (10^{-3}–10^{-1} s^{-1}). At the same time, very high rates of local deformation in submicron areas ($\geqslant 10^{-1}$ s^{-1}) are characteristic for many processes, including dry friction between rough surfaces, abrasive and erosive wear, atomic-force microscopy, nanolithography by the methods of imprinting and scribing, and fine grinding [5]. Thus, the area of the mechanical properties of materials that is characterized by both short loading time intervals and small deformation zones is little studied. Under these conditions, the ordinary mechanisms (in particular, dislocation mechanisms) of plastic flow can be strongly impeded or suppressed.

Some authors (see, e.g., [6, 7]) attempted to find the strain-rate dependences of dynamic hardness, fracture toughness, and the coefficient of recovery of some ionic crystals (NaCl, LiF, and MgO), glasses, and ceramics in the range $\dot{\varepsilon} \sim 10^{4}$–$10^{5}$ s^{-1} by the method of shock loading. Thus, a rather narrow $\dot{\varepsilon}$ range (about one order of magnitude) was covered. In addition, one of two parameters (force and indentation size) needed for determining hardness, as well as the actual shape and duration of a loading pulse, was only estimated (from indirect data) rather than measured. The strain-rate range 10^{-1} s^{-1} < $\dot{\varepsilon}$ < 10^{4} s^{-1}, which is of great importance in practice, still remains poorly studied. Moreover, it should be noted that the strain-rate dependences of the mechanical properties of the same material can be different in different $\dot{\varepsilon}$ ranges. Therefore, it is advisable to investigate them in as wide a range of $\dot{\varepsilon}$ as possible.

The aim of this study is to find the strain-rate sensitivity of microhardness H for a number of both ionic and covalent crystals for $\dot{\varepsilon}$ values from 3×10^{-3} to 10^{2} s^{-1} that covers approximately five orders of magnitude (for an indentation depth of about 1 μm). To this end, using a device designed at the Laboratory of Nanoindentation, Tambov State University [8], we carried out the indentation of the sample surface by a diamond Berkovich pyramid under the action of a triangular force pulse with the same amplitude $P_{\max} = 0.42$ N and various durations $\tau = 10$ ms – 300 s of the loading-pulse front. A force pulse was formed by an electrodynamic computer-controlled drive. Its shape $P(t)$, as well as the time dependence of the indentation depth $h(t)$, was recorded with a time resolution of 50 μs and stored by the computer. Next, using these data, we constructed the P–h diagram of the complete loading–unloading cycle (Fig. 1). This ensured fully controlled and identical test conditions for various average strain rates $\dot{\varepsilon} \approx \frac{dh}{dt}\frac{1}{h} \sim \frac{1}{\tau}$. The ratio of $P_{\max}$ to the corresponding indentation area $S = 24.5h^2$ was taken to be dynamic hardness $H_d = \frac{P_{\max}}{S}$.

The main results are summarized in Fig. 2, which shows the relative variation of H_{d} as a function of $\dot{\varepsilon}$ on

---

* *Tambov State University, ul. Internatsional'naya 33, Tambov, 392622 Russia*
e-mail: golovin@tsu.tmb.ru

** *Institute of Solid State Physics, Russian Academy of Sciences, Chernogolovka, Moscow oblast, 142432 Russia*

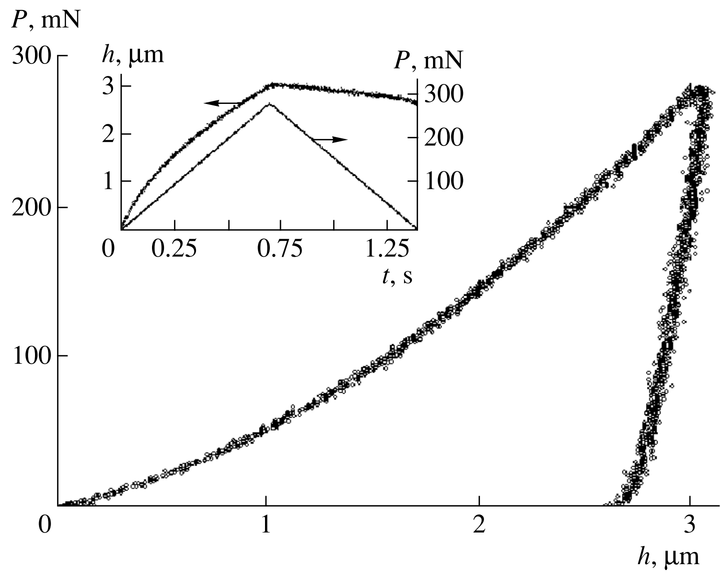

Fig. 1. Typical P–h diagram obtained under the indentation of the LiF crystals. The insert shows the $P(t)$ and $h(t)$ time dependences.

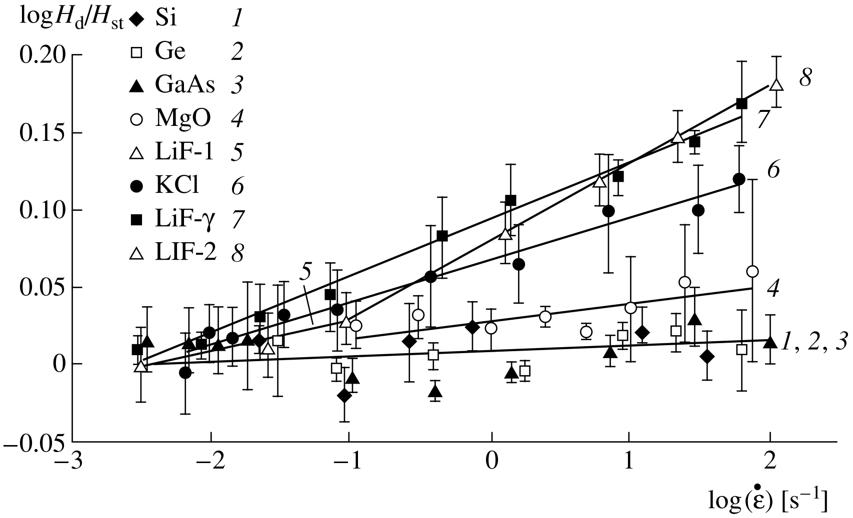

Fig. 2. Relative change in dynamic hardness, H_d/H_{st}, vs. the average strain rate $\dot{\varepsilon}$ under the indenter for the materials under investigation.

the log–log scale. It is seen that the strain-rate sensitivity is virtually absent in the Si, Ge, and GaAs covalent crystals. At the same time, H_d for soft ionic crystals such as KCl, LiF, and γ-irradiated LiF (at a dose of about 10^6 Gy) and metals (Al) increases noticeably with $\dot{\varepsilon}$. The strain-rate sensitivity of H_d for MgO crystals is very weak in the $\dot{\varepsilon}$ range under investigation. An interesting feature in the behavior of $H_d(\dot{\varepsilon})$ was observed in LiF. The slope for low strain rates was less than the slope in the $\dot{\varepsilon}$ range between 10^{-1} and 10^2 s^{-1} by a factor of 2.5.

Thus, the materials under investigation can be divided into two groups (Fig. 3). The strain-rate sensitivity of H_d for crystals with a high ratio of the quasi-static hardness H_{st} to the Young modulus E $\left(\frac{H_{st}}{E} \geq 0.04\right)$ was either absent or very low in the $\dot{\varepsilon}$ range under investigation. At the same time, crystals with $\frac{H_{st}}{E} \leq 0.015$ exhibit a strong dependence of H_d on $\dot{\varepsilon}$.

Now, we briefly discuss the results. In the framework of a simple phenomenological model, indentation can be considered as a relaxation process where external forces cause the formation and motion of structural defects (dislocations, interstitial sites, twins, nucleation centers of a new phase, etc.) tending to reduce the contact stresses. Under static conditions, the hardness H_{st} of a material is determined from the balance between applied forces and forces resisting the motion of defects—carriers of plastic deformation. If an applied force pulse is short, the finite rate of the generation and motion of defects can limit the relaxation depth of contact stresses so that the dynamic value H_d appears to be larger than H_{st}. In the general case, the dependence $H_d = f(\dot{\varepsilon})$ in the presence of a number of competing mechanisms can have the form schematically shown in Fig. 4. The horizontal sections correspond to the case where the rate of stress relaxation through the dominant mechanism in this $\dot{\varepsilon}$ range is higher than the loading rate. The inclined sections appear when the characteristic times of relaxation processes are comparable with a loading duration. This behavior is equivalent to the appearance of internal-friction peaks under these conditions. This circumstance (in combination with the sizes of the deformed zone) provides information about the nature and mobility of major carriers of plastic deformation. A change in the slope of the function $H_d(\dot{\varepsilon})$ (particularly, for LiF at $\dot{\varepsilon} \sim 10^{-1}$ s^{-1}) likely corresponds to the transition from one dominant mechanism of stress relaxation to another. The absence of the strain-rate dependence of H_d in a certain $\dot{\varepsilon}$ range means that the dominant stress-relaxation mechanism in this range is so efficient under these conditions that it ensures quasistatic conditions even for the highest strain rate in this range. However, this behavior does not exclude the existence and manifestation of the strain-rate dependences of H_d in other $\dot{\varepsilon}$ ranges.

Thus, plastic strain under the indenter is high, H_d for Si, Ge, and GaAs is independent of the strain rate, the number of formed dislocations is small, and their mobility at room temperature is extremely low. In our opinion, all these circumstances means that plastic relaxation in these materials is provided by processes that do not involve dislocations. In these processes, nonequilibrium point defects or nucleation centers of new phases induced by high contact pressures are formed and move from under the indenter. Numerical simulation by the methods of multiparticle molecular dynamics indicates that, under indentation, the activation energy of motion of interstitial atoms and small-atomic clusters can be much lower than that of motion of dislocations. Accordingly, the mobility of these atoms at low temperatures is higher than the mobility of dislocations [9, 10]. A number of independent data also testify to a significant role of nonequilibrium point defects in the mass transfer in the process of microindentation [11–15]. Thermoactivation analysis of the strain-rate dependences of H_d obtained for various testing temperatures will possibly determine more exactly what particular mechanisms are responsible for a certain type of stress relaxation under the indenter.

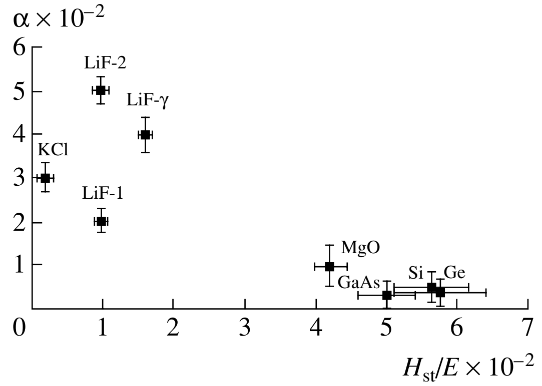

Fig. 3. Coefficient of the strain-rate sensitivity $\alpha = \frac{\log\left(\frac{H_d}{H_{st}}\right)}{\log\dot{\varepsilon}}$ vs. $\frac{H_{st}}{E}$ for the materials under consideration.

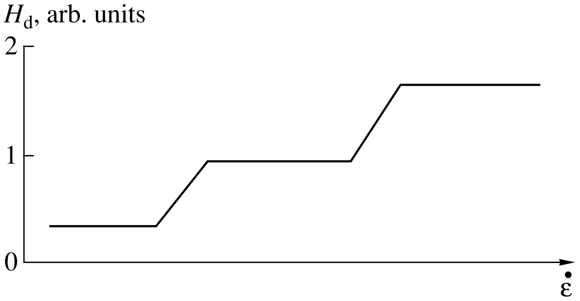

Fig. 4. Schematic plot of the function $H_d = f(\dot{\varepsilon})$ in the presence of several competing deformation mechanisms.

ACKNOWLEDGMENTS

This work was supported by the Russian Foundation for Basic Research (project nos. 01-02-16573 and 01-02-97006), the Ministry of Education of the Russian Federation (project no. E02-3.4-263), and the UK Royal Society.

We are grateful to M.M. Chaudhri and I. Lim (Cavendish Laboratory, Cambridge, UK) for their support, great interest, and stimulating discussions and to V.I. Ivolgin and V.V. Korenkov for assistance in the preparation of the instrumentation.

This work was performed at Tambov State University and Cavendish Laboratory, Cambridge, UK.

REFERENCES

1. M. A. Shtremel', *Strength of Alloys* (Mosk. Inst. Stali i Splavov, Moscow, 1997).
2. W. C. Oliver and G. M. Pharr, J. Mater. Res. **7** (6), 1564 (1992).

3. C. M. Li, Mater. Sci. Eng. A **322**, 23 (2002).
4. Yu. I. Golovin, A. I. Tyurin, and B. Ya. Farber, Philos. Mag. A **82** (10), 1857 (2002).
5. G. V. Dedkov, Usp. Fiz. Nauk **170** (6), 585 (2000) [Phys. Usp. **43**, 541 (2000)].
6. M. M. Chaudhri, J. K. Wells, and A. Stephens, Philos. Mag. A **43** (3), 643 (1981).
7. R. J. Anton and G. Subhash, Wear **239**, 27 (2000).
8. Yu. I. Golovin, A. I. Tyurin, and B. Ya. Farber, J. Mater. Sci. **37**, 895 (2002).
9. P. Zhao and Y. Shimomura, Comput. Mater. Sci. **14** (1), 84 (1999).
10. M. Koyanagi, T. Tsutsumi, K. Ohsawa, and E. Kuramoto, Comput. Mater. Sci. **14**, 103 (1999).
11. M. Sh. Akchurin and V. R. Regel, Chem. Rev. **23**, Part 2, 59 (1998).
12. Yu. I. Golovin and A. I. Tyurin, Pis'ma Zh. Éksp. Teor. Fiz. **60** (3), 722 (1994) [JETP Lett. **60**, 742 (1994)].
13. B. Ya. Farber, V. I. Orlov, V. I. Nikitenko, and A. N. Heuer, Philos. Mag. A **78** (3), 671 (1998).
14. V. N. Rozhanskii and M. A. Velednitskaya, Phys. Status Solidi A **8** (2), 551 (1971).
15. V. L. Indenbom, Pis'ma Zh. Éksp. Teor. Fiz. **12** (12), 526 (1970) [JETP Lett. **12**, 369 (1970)].

Translated by Yu. Vishnyakov

Doklady Physics, Vol. 48, No. 9, 2003, pp. 509–511. Translated from Doklady Akademii Nauk, Vol. 392, No. 1, 2003, pp. 59–62.

MECHANICS

On the Theory of Statically Definable Relationships and the Limiting State for Plastic Solids

D. D. Ivlev and Academician A. Yu. Ishlinskiĭ†

Received March 13, 2003

The statically definable states of plastic solids are considered as the states corresponding to the limiting values of the bearing strength and fracture.

1. We consider an elastoplastic beam that is fixed at both ends and loaded by a transverse force P (Fig. 1a). Figure 1b shows the schematic force diagram, where R_1 and R_2 are the reactions at the supports, M_1 and M_2 are the bending moments in the fixations, and M_3 is the bending moment in the section where the force P acts. The equilibrium equations have the form

$$R_1 + R_2 = P, \quad M_1 + M_3 - R_1 l_1 = 0, \quad M_2 + M_3 - R_2 l_2 = 0. \tag{1.1}$$

From Eqs. (1.1), it follows that

$$M_1 l_2 + M_2 l_1 + M_3(l_1 + l_2) = P l_1 l_2. \tag{1.2}$$

We consider the orthogonal space of generalized stresses M_1, M_2, and M_3 and denote the limiting values of bending moments as m_1, m_2, and m_3, respectively. The planes $M_i = m_i$ are called yield surfaces and form the yield surface restricting variations in M_i. Let us assume that $M_i \geq 0$. In this case, the bending moments vary within the limits

$$0 \leq M_i \leq m_i, \quad m_i - \text{const}, \tag{1.3}$$

where m_i is the constant.

Figure 2 shows the rectangular parallelepiped corresponding to inequalities (1.3) determining variations in the vector

$$\mathbf{M} = M_1\mathbf{i} + M_2\mathbf{j} + M_3\mathbf{k}. \tag{1.4}$$

Relationship (1.2) determines a plane translating in the space M_i with variation of the force P. The part of plane (1.2) inside the parallelepiped in Fig. 2 corresponds to the statically possible states of the beam. The real values of M_i for a given force P are determined by the relationships between stressed and strained states, beam shape, and boundary conditions.

When loading the beam, i.e., $dP > 0$, the process of modifying its state can be represented as follows. First, when $0 \leq M_i < m_i$, elastic deformation proceeds; further, one of the bending moments, e.g., M_1, attains the limiting value $M_1 = m_1$, a plastic hinge is formed, and the beam retains the bearing strength. With further loading, the second bending moment, e.g., M_2, reaches the limiting value $M_2 = m_2$, the second plastic hinge is formed, and the beam also retains the bearing strength. The beam loses the bearing strength when the third plastic hinge is formed for $M_3 = m_3$, the stressed state of the beam becomes statically definable, and, according to Eqs. (1.2) and (1.3), the force P attains the limiting value

$$P_{\lim} = \frac{1}{l_1 l_2}(m_1 l_2 + m_2 l_1 + m_3(l_1 + l_2)). \tag{1.5}$$

In this case, the beam acquires the kinematic freedom for deformation (Fig. 1c).

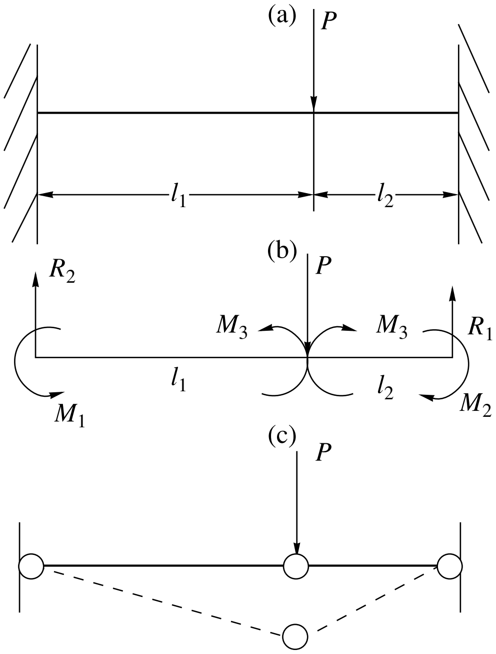

Fig. 1.

---

† Deceased.

Chuvash State University, Moskovskiĭ pr. 15, Cheboksary, 428015 Russia

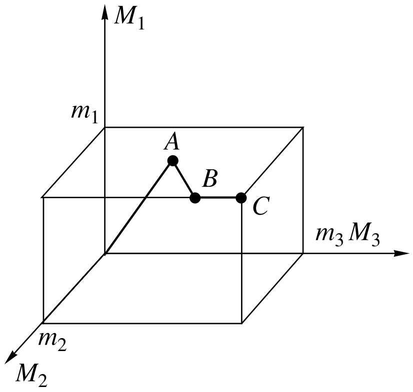

Fig. 2.

In the M_i space, loading corresponds to the attainment of the smooth yield surface $M_1 = m_1$ (the point A in Fig. 2) by the vector **M**. Further, the vector **M** moves in the yield surface $M_1 = m_1$ until singular points of the yield surface, i.e., the edge of intersection between two smooth yield surfaces $M_1 = m_1$ and $M_2 = m_2$ (the point B in Fig. 2). The bearing strength is lost when the vector **M** attains the limiting singular point $M_1 = m_1$, $M_2 = m_2$, and $M_3 = m_3$ that lies on the yield surface and corresponds to the intersection between three smooth yield surfaces (the point C in Fig. 2).

As long as the construction retains the state of static indefinability when the material properties (either elastic or others providing the coupling between stressed and strained states) play a role in deformation, the construction retains the bearing strength. The construction loses the bearing strength when it reaches the limit of retaining the statically indefinable state.

It should be noted that the limiting surfaces can generally be modified during loading depending on the variation in plastic strains, the history of loading, etc. This circumstance determines the singularity position corresponding to the state of static definability in the stress space (the point C in Fig. 2).

The above consideration can be extended to the behavior of an elastoplastic continuum.

2. We consider the relationships of perfect-plasticity theory. A 2D problem is described by the two equilibrium equations

$$\frac{\partial\sigma_x}{\partial x} + \frac{\partial\tau_{xy}}{\partial y} = 0, \quad \frac{\partial\tau_{xy}}{\partial x} + \frac{\partial\sigma_y}{\partial y} = 0 \qquad (2.1)$$

and the limiting-state condition

$$f(\sigma_x, \sigma_y, \tau_{xy}) = 0, \qquad (2.2)$$

where σ_x, σ_y, and τ_{xy} are the stress components in the Cartesian coordinate system xy.

The set of Eqs. (2.1) and (2.2) for the 2D problem is statically definable.

An axisymmetric problem is described by the two equilibrium equations

$$\begin{aligned} \frac{\partial\sigma_\rho}{\partial\rho} + \frac{\partial\tau_{\rho z}}{\partial z} + \frac{\sigma_\rho - \sigma_\theta}{\rho} &= 0, \\ \frac{\partial\tau_{\rho z}}{\partial\rho} + \frac{\partial\sigma_z}{\partial z} + \frac{\tau_{\rho z}}{\rho} &= 0, \end{aligned} \qquad (2.3)$$

where σ_ρ, σ_θ, σ_z, and $\tau_{\rho z}$ are the stress constants in the cylindrical coordinate system $\rho\theta z$.

With the single limiting relationship

$$f(\sigma_\rho, \sigma_\theta, \sigma_z, \tau_{\rho z}) = 0, \qquad (2.4)$$

three relationships (2.3) and (2.4) are statically indefinable with respect to the four stress components σ_ρ, σ_θ, σ_z, and $\tau_{\rho z}$.

The axisymmetric problem is statically definable in perfect-plasticity theory if two limiting relationships are specified:

$$f_1(\sigma_\rho, \sigma_\theta, \sigma_z, \tau_{\rho z}) = 0, \quad f_2(\sigma_\rho, \sigma_\theta, \sigma_z, \tau_{\rho z}) = 0. \qquad (2.5)$$

The properties of equations in statically definable relationships for the axisymmetric problem were investigated in [2].

A 3D problem is described by the three equilibrium equations

$$\begin{aligned} \frac{\partial\sigma_x}{\partial x} + \frac{\partial\tau_{xy}}{\partial y} + \frac{\partial\tau_{xz}}{\partial z} &= 0, \\ \frac{\partial\tau_{xy}}{\partial x} + \frac{\partial\sigma_y}{\partial y} + \frac{\partial\tau_{yz}}{\partial z} &= 0, \\ \frac{\partial\tau_{xz}}{\partial x} + \frac{\partial\tau_{yz}}{\partial y} + \frac{\partial\sigma_z}{\partial z} &= 0. \end{aligned} \qquad (2.6)$$

The relationships of elasticity theory represent a statically indefinable set of equations. The stress field satisfying equilibrium Eqs. (2.6) is statically possible.

If the stressed state meets the plasticity condition

$$f_1(\sigma_{ij}) = 0, \qquad (2.7)$$

according to [3], Eqs. (2.6) and (2.7) determine the plastic state of a material, and the set of four Eqs. (2.6) and (2.7) is statically indefinable.

If the stressed state meets two relationships

$$f_1(\sigma_{ij}) = 0, \quad f_2(\sigma_{ij}) = 0, \qquad (2.8)$$

according to [3], the relationships determine a developed plastic state, and set of Eqs. (2.6) and (2.8) is also statically indefinable.

The relationships of perfect-plasticity theory are statically definable if three plasticity conditions are met:

$$f_1(\sigma_{ij}) = 0, \quad f_2(\sigma_{ij}) = 0, \quad f_3(\sigma_{ij}) = 0. \tag{2.9}$$

For an isotropic material, three independent conditions

$$\begin{gathered} f_1(\sigma_1, \sigma_2, \sigma_3) = 0, \quad f_2(\sigma_1, \sigma_2, \sigma_3) = 0, \\ f_3(\sigma_1, \sigma_2, \sigma_3) = 0 \end{gathered} \tag{2.10}$$

lead to the stress field

$$\sigma_1 = \text{const}, \quad \sigma_2 = \text{const}, \quad \sigma_3 = \text{const} \tag{2.11}$$

and static definability exists under the full-plasticity condition [4]

$$\sigma_1 = \sigma_2, \quad \sigma_3 = \sigma_1 + 2k, \tag{2.12}$$

where k is the constant.

If conditions (2.12) are met, the following relationships are valid [3]:

$$\begin{gathered} \sigma_x = \sigma + \frac{2}{3}k + 2kn_1^2, \quad \tau_{xy} = 2kn_1n_2, \\ \sigma_y = \sigma + \frac{2}{3}k + 2kn_2^2, \quad \tau_{yz} = 2kn_2n_3, \\ \sigma_z = \sigma + \frac{2}{3}k + 2kn_3^2, \quad \tau_{xz} = 2kn_3n_1, \\ n_1^2 + n_2^2 + n_3^2 = 1, \end{gathered} \tag{2.13}$$

where n_1, n_2, and n_3 are the direction cosines for the third principal stress σ_3 in the space of principal stresses σ_1, σ_2, and σ_3.

Expressions (2.13) lead to the following three plasticity conditions determining the static definability of the relationships:

$$\left(\sigma_x - \sigma - \frac{2}{3}k\right)\left(\sigma_y - \sigma - \frac{2}{3}k\right) = \tau_{xy}^2 \quad (xyz) \tag{2.14}$$

or

$$\left(\sigma_x - \sigma - \frac{2}{3}k\right)\tau_{yz} = \tau_{xy}\tau_{xz} \quad (xyz). \tag{2.15}$$

The relationships for the statically definable problem in perfect-plasticity theory are generally represented in the form [4]

$$\begin{gathered} \sigma_x = \nu + \varphi_1(\sigma, n_1n_2n_3), \quad \tau_{xy} = \varphi_4(\sigma, n_1n_2n_3), \\ \sigma_y = \nu + \varphi_2(\sigma, n_1n_2n_3), \quad \tau_{yz} = \varphi_5(\sigma, n_1n_2n_3), \\ \sigma_z = \nu + \varphi_3(\sigma, n_1n_2n_3), \quad \tau_{xz} = \varphi_6(\sigma, n_1n_2n_3), \\ \sigma = \frac{1}{3}(\sigma_x + \sigma_y + \sigma_z), \quad n_1^2 + n_2^2 + n_3^2 = 1. \end{gathered} \tag{2.16}$$

Relationships (2.16) generally set the statically definable state for an anisotropic perfectly plastic solid.

The properties of the statically definable set of Eqs. (2.6) and (2.16) in perfect-plasticity theory are investigated for three independent functions φ_i [4] for

$$\begin{gathered} \varphi_1 = N_1^2, \quad \varphi_2 = N_2^2, \quad \varphi_3 = N_3^2, \\ \varphi_4 = N_1N_2, \quad \varphi_5 = N_2N_3, \quad \varphi_6 = N_1N_3 \end{gathered} \tag{2.17}$$

or

$$\begin{gathered} \varphi_1 = N^2\cos^2\theta_1, \quad \varphi_2 = N^2\cos^2\theta_2, \\ \varphi_3 = N^2\cos^2\theta_3, \quad \varphi_4 = N^2\cos^2\theta_1\cos\theta_2, \\ \varphi_5 = N^2\cos\theta_2\cos\theta_3, \quad \varphi_6 = N^2\cos\theta_1\cos\theta_3, \\ N^2 = N_1^2 + N_2^2 + N_3^2 = \varphi_1 + \varphi_2 + \varphi_3, \\ \cos^2\theta_1 + \cos^2\theta_2 + \cos^2\theta_3 = 1. \end{gathered} \tag{2.18}$$

The statically definable set of Eqs. (2.6), (2.16), and (2.18) is hyperbolic [4].

It should be noted that Eqs. (2.16)–(2.18) determine the equality between two principal stresses.

A loaded perfectly elastoplastic solid passes the stages of elastic and elastoplastic deformations and finally loses the bearing strength and fails.

An elastic solid is statically indefinable, stresses in it vary with modification of the strained state, and the equations describing the deformation process are elliptic.

For states characterized by plasticity conditions (2.7) and (2.8), static indefinability is retained, the equations of the elastoplastic state are elliptic [5, 6], and stresses vary due to varying strain.

A perfectly elastoplastic solid loses the bearing strength and fails if it reaches the statically definable state and acquires kinematic freedom for flow in a fixed stressed state determined by the limiting load. The equations describing the statically definable state of a perfectly plastic medium are hyperbolic. Therefore, the range of a plastic flow and fracture can be separated and a plastic material flows by sliding.

REFERENCES

1. W. Prager and Ph. Hodge, *Theory of Perfectly Plastic Solids* (Wiley, New York, 1951; Inostrannaya Literatura, Moscow, 1956).
2. D. D. Ivlev and T. N. Martynova, Dokl. Akad. Nauk SSSR **164**, 764 (1965) [Sov. Phys. Dokl. **10**, 991 (1966)].
3. D. D. Ivlev and A. Yu. Ishlinskiĭ, Dokl. Akad. Nauk **368**, 333 (1999) [Dokl. Phys. **44**, 642 (1999)].
4. A. Yu. Ishlinskiĭ and D. D. Ivlev, *Mathematical Theory of Plasticity* (Fizmatlit, Moscow, 2001).
5. T. Thomas, *Plastic Flow and Fracture in Solids* (Academic, New York, 1961; Mir, Moscow, 1964).
6. D. D. Ivlev and G. I. Bykovtsev, *Theory of Strengthening Plastic Body* (Nauka, Moscow, 1971).

Translated by V. Bukhanov

Doklady Physics, Vol. 48, No. 9, 2003, pp. 512–516. Translated from Doklady Akademii Nauk, Vol. 392, No. 2, 2003, pp. 185–189.
Original Russian Text Copyright © 2003 by V. Babeshko, O. Babeshko.

MECHANICS

Generalized Factorization in Boundary Value Problems in Multiply Connected Domains

Academician V. A. Babeshko and O. M. Babeshko

Received May 8, 2003

The generalized factorization method introduced in [1] is applied to boundary value problems in multiply connected domains with boundaries allowing the change of sign of the surface curvature. In [2], we used the classical, or projection, factorization method [3, 4], which is effective only for simply connected convex domains, where only areas of boundary flattening are possible. This method is based on the application of the exponential representation of the group of plane–parallel translations of two- or three-dimensional space. Generalized factorization is based on that representation of the group of arbitrary motions, which leads to Bessel or spherical functions [5, 6]. In this case, projections are carried out not on a plane and half-space as in classical factorization but on more complex domains such as circles, cylinders, and balls, which considerably extends the geometry of boundary value problems.

The properties of generalized factorization make it possible to overcome difficulties concerning a complex geometry of domains of boundary value problems, which, in particular, are multiply connected and have relief boundaries.

The method opens new possibilities of studying a number of multidimensional problems in complex domains in the presence of lines of change in the boundary conditions, i.e., mixed problems. It is specially adapted to the study of processes in complex-structure objects, in particular, physicomechanical, chemical, and seismological processes in lithospheric plates of the block structure, ecological problems in extended domains with relief boundaries, and bed streams on broken ground.

New relations describing the solutions of boundary value problems in the integral form admitting discretization, as well as normally solvable sets of integral equations for determining necessary auxiliary functions.

We consider a bounded, multiply connected, domain Ω with a composite, twice continuously differentiable, boundary Γ consisting of outer Γ_1 and inner Γ_2 parts. The outer part Γ_1 is the set of points that can be in contact with a plane under all possible rolling motions of the body on this plane, which does not cross the body at other points. Possible flattening areas of the boundary surface also belong to this set when the touching plane does not cross the boundary in other areas, while contact is allowable. The inner part Γ_2 includes all remaining set of the body boundary, including boundaries of internal cavities, boundaries of tunnels and holes piercing the body even if they have convexities, and boundary areas having at least one negative principal curvature. It is assumed that each point of Γ_2 can touch a sphere of a finite radius, which does not cross the body but can only touch it at other points. The multiply connected domain Ω is topologically homeomorphic (allows the deformation without beaks) to a three-dimensional ball with handles and internal ball cavities and is oriented manifold with the boundary.

Crack cavities with a zero gap between shores, which form vibration strength viruses [7], are disregarded in this case. Sets composing Γ_k can be disconnected and multiply connected.

In the specified domain, we consider the boundary value problem for the system of partial differential equations with constant coefficients:

$$\mathbf{Q}(\partial x_n, \partial x_k)\varphi = 0, \quad \mathbf{x} \in \Omega(R^3), \tag{1}$$

$$\mathbf{R}(\partial x_k)\varphi = \mathbf{f}, \quad \mathbf{x} \in \Gamma = \partial\Omega. \tag{2}$$

The operator $\mathbf{Q}$ is represented as the matrix

$$\mathbf{Q}(\partial x_n, \partial x_k) = \|a_{mrnk}\partial x_n \partial x_k + b_{mrk}\partial x_k + c_{mr}\|.$$

Here,

$$a_{mrnk} f_n f_k = \sum_{n=1}^{3}\sum_{k=1}^{3} a_{mrnk} f_n f_k,$$

$$\mathbf{R}(\partial x_k) = \|h_{mrk}\partial x_k + p_{mr}\|, \quad \partial x = \frac{\partial}{\partial x},$$

$$h_{mrk} = h_{mrk}(\Gamma),$$

Kuban State University, ul. Karla Libknekhta 149,
Krasnodar, 350640 Russia
e-mail: babeshko@kubsu.ru

1028-3358/03/4809-0512$24.00 © 2003 MAIK “Nauka/Interperiodica”

$$\varphi = \{\varphi_r\}, \quad r = 1, 2, \dots, M, \quad m = 1, 2, \dots, M,$$
$$\mathbf{f} = \{f_r\}, \quad \varphi(\mathbf{x}) = \varphi(x_1, x_2, x_3),$$
$$\mathbf{Q}(\alpha) \equiv \mathbf{Q}(-i\alpha_n, -i\alpha_k),$$
$$n, k = 1, 2, 3, \quad Q = \det\mathbf{Q}(\alpha),$$

where the summation over repeated subscripts is implied. For real α_k,

$$\det\|a_{mrnk}\alpha_n\alpha_k\| \neq 0.$$

In contrast to [2], there is no restriction on the operator $\mathbf{R}$, and the boundary conditions need not be natural. They must only satisfy the complimentarity condition for elliptic systems [8].

A boundary value problem is analyzed in spaces of slowly increasing generalized functions $\mathbf{H}_s(\Omega)$, including classical ones, which are introduced in terms of the norms

$$\|\varphi\|_s^2 = \sum\|\varphi_r\|_s^2, \quad \|\varphi_r\|_s^2 = \int\int\int_{-\infty}^{\infty}|F\varphi_r|^2(1+|\alpha|)^{2s}d\alpha,$$
$$r = 1, 2, \dots, M,$$
$$|\alpha|^2 = \alpha_1^2 + \alpha_2^2 + a_3^2, \quad d\alpha = d\alpha_1 d\alpha_2 d\alpha_3,$$
$$d\mathbf{x} = dx_1 dx_2 dx_3,$$
$$F\varphi_r = \int\int\int_{-\infty}^{\infty}\varphi_r(x)e^{i\langle\alpha,\, x\rangle}dx, \tag{3}$$
$$\varphi_r = \frac{1}{(2\pi)^3}\int\int\int_{-\infty}^{\infty}F\varphi_r e^{-i\langle\alpha,\, x\rangle}d\alpha,$$
$$\langle\alpha, \mathbf{x}\rangle = \alpha_1 x_1 + \alpha_2 x_2 + \alpha_3 x_3,$$
$$\mathbf{f} \in \mathbf{H}_\lambda(\Gamma), \quad \lambda > s + 0.5.$$

To analyze the boundary value problem, we introduce an exterior vector form $\omega(\alpha, x)$ whose components have the form

$$\omega_m(\alpha, x) = R_m dx_1 \wedge dx_2 + Q_m dx_1 \wedge dx_3 + P_m dx_2 \wedge dx_3,$$
$$P_m = \sum_r e^{i\langle\alpha,\, x\rangle}[a_{mr11}(\partial x_1\varphi_r - i\alpha_1\varphi_r) - a_{mr12}i\alpha_2\varphi_r + a_{mr13}\partial x_3\varphi_r + b_{mr1}\varphi_r],$$
$$Q_m = -\sum_r e^{i\langle\alpha,\, x\rangle}[a_{mr22}(\partial x_2\varphi_r - i\alpha_2\varphi_r) - a_{mr23}i\alpha_3\varphi_r + a_{mr12}\partial x_1\varphi_r + b_{mr2}\varphi_r], \tag{4}$$
$$R_m = \sum_r e^{i\langle\alpha,\, x\rangle}[a_{m33}(\partial x_3\varphi_r - i\alpha_3\varphi_r) - a_{mr13}i\alpha_1\varphi_r - a_{mr23}i\alpha_2\varphi_r + b_{mr3}\varphi_r].$$

Introducing topology generated by the Euclidean space, we consider the domain Ω as an oriented chain with the a boundary whose orientation is induced by the orientation of the domain [9].

Using the Stokes theorem in the domain Ω and assuming that the vector function φ satisfies the set of differential equations (1), we arrive at the expression

$$\varphi(\mathbf{x}) = \frac{1}{8\pi^3}\int\int\int_\sigma Q^{-1}(\alpha)\mathbf{D}(\alpha) \times \int\int_\Gamma e^{-i\langle\alpha,\, x\rangle}\omega(\alpha, \xi)d\alpha_1 \wedge d\alpha_2 \wedge d\alpha_3,$$
$$\mathbf{Q}^{-1}(\alpha) = Q^{-1}(\alpha)\mathbf{D}(\alpha), \quad \mathbf{D}(\alpha) = \mathbf{D}(\alpha_1, \alpha_2, \alpha_3),$$
$$\omega(\alpha, \xi) = \omega(\alpha_1, \alpha_2, \alpha_3, \xi), \quad \xi = \{\xi_1, \xi_2, \xi_3\}.$$

We recall that, similar to [2], the exterior form contains relations describing the specified boundary conditions and functions that must be determined or their normal derivatives with boundary values. When the combination of derivatives and functions in boundary conditions (2) differs from the natural combinations appearing in Eqs. (4), they are formed in Eqs. (4) by addition and subtraction of the necessary terms to obtain the left-hand sides of Eqs. (2) without change in ω.

In view of the specific character of the boundary Γ and taking into account the boundary parts Γ_1, where curvature is nonnegative, and Γ_2, where at least one principal curvature is negative, we denote areas swept by normal vectors to Γ_1 and Γ_2 beyond $\bar{\Omega}$ by $\Theta_1$and Θ_2, respectively. Thus, areas Θ_k adjoin Ω along the surfaces Γ_k and have nonzero thickness.

According to the factorization method [2], it is necessary to require that the right-hand side of the mentioned relation is equal to zero beyond the domain Ω; i.e.,

$$\varphi(x) = 0, \quad x \in R^3/\bar{\Omega}.$$

First, we consider the boundary part Γ_1. In this case, we obtain the condition

$$\varphi(\mathbf{x}) = \frac{1}{8\pi^3}\int\int\int_\sigma Q^{-1}(\alpha)\mathbf{D}(\alpha) \times \int\int_\Gamma e^{-i\langle\alpha,\, x\rangle}\omega(\alpha, \xi)d\alpha_1 \wedge d\alpha_2 \wedge d\alpha_3 = 0, \tag{5}$$
$$x \subset \Theta_1.$$

Using transformations made in [2] when factorizing with respect to the tangent plane to the boundary Γ_1 and calculating two-dimensional Leray residues, we arrive at the relations

$$\sum_{r=1}^{M}\iint_{\delta_r}\iint_{\Gamma}\frac{\mathbf{D}(\alpha)e^{-i\langle\alpha,\mathbf{x}\rangle_-}\omega(\alpha_1,\alpha_2,\overset{-}{\alpha}_{3r},\xi)}{\partial\alpha_3 Q(\alpha_1,\alpha_2,\overset{-}{\alpha}_{3r})}d\alpha_1\wedge d\alpha_2\equiv 0, \tag{6}$$

$$\mathbf{x}\subset\Theta_1,\quad \operatorname{Im}\overset{-}{\alpha}_{3r}(\alpha_1,\alpha_2)<0,$$

$$\langle\alpha,\mathbf{x}\rangle_{\pm} = \alpha_1x_1+\alpha_2x_2+\overset{\pm}{\alpha}_3x_3.$$

Here, δ_r are two-dimensional cycles not homologous to zero and we assume, as in [2], that the zero set $\alpha_3 = \overset{\pm}{\alpha}_{3r}(\alpha_1, \alpha_2)$ of the function $Q(\alpha)$ has a codimension of 1 and the same multiplicity. For other characteristics of the zero set, it is necessary to analyze more complex multidimensional residues, which requires study of homology groups on multidimensional complex manifolds [9, 10].

Following [2], from the last relations, the first set of equations is constructed in the form

$$\iint_{\Gamma}\mathbf{D}(\alpha_1,\alpha_2,\overset{-}{\alpha}_{3r})\omega(\alpha_1,\alpha_2,\overset{-}{\alpha}_{3r},\xi) = 0, \tag{7}$$

$$r = 1, 2, \ldots, M,\quad -\infty<\alpha_1,\alpha_2<\infty.$$

The derivation of this set, as well as transformations made for its regularization, is described in detail in [2]. We only remind note that the relation is satisfied on the elements of a decomposition of unity for each local coordinate system induced at the boundary Γ_1 by the coordinate systems of the inner neighborhoods of the topological structure of the domain Ω with the conservation of the orientation.

We now consider the area Θ_2, which is the area swept by outer normal vectors to the boundary Γ_2 beyond Ω. Let us apply generalized factorization [1] to separate classes of functions with a support in $\overline{\Omega}$. Using notation from [1], and omitting cumbersome manipulations, we can represent Eqs. (5) in the form

$$\iint_{\Gamma}\mathbf{D}_k^0(\gamma_1,\gamma_2,\overset{+\cdot}{\gamma}_{3r\cdot})\{e^{i\langle\alpha(\gamma),\xi(\eta)\rangle_+}\}_k^+$$

$$\times\,\omega^0(\gamma_1,\gamma_2,\overset{+}{\gamma}_{3r},\eta) = 0,$$

$$r = 1, 2, \ldots, M,\quad k = 0, 1, 2, \ldots,$$

$$\gamma_3 = \overset{+}{\gamma}_{3r}(\gamma_1,\gamma_2),\quad \operatorname{Im}\overset{+}{\gamma}_{3r}(\gamma_1,\gamma_2)>0, \tag{8}$$

$$\mathbf{D}_{2k}^0(\gamma_1,\gamma_2,\gamma_3) = \mathbf{D}^0(\gamma_1,\gamma_2,\gamma_3)Q^0(\gamma_1,\gamma_2,-\gamma_3)$$

$$+\,\mathbf{D}^0(\gamma_1,\gamma_2,-\gamma_3)Q^0(\gamma_1,\gamma_2,\gamma_3),$$

$$\mathbf{D}_{2k+1}^0(\gamma_1,\gamma_2,\gamma_3) = \mathbf{D}^0(\gamma_1,\gamma_2,\gamma_3)Q^0(\gamma_1,\gamma_2,-\gamma_3)$$

$$-\,\mathbf{D}^0(\gamma_1,\gamma_2,-\gamma_3)Q^0(\gamma_1,\gamma_2,\gamma_3);$$

where $\gamma_3 = \overset{+}{\gamma}_{3r\cdot}(\gamma_1, \gamma_2)$ and $\gamma_3 = \overset{-}{\gamma}_{3r}(\gamma_1, \gamma_2)$ are the zero sets of the function $Q^0(\gamma_1, \gamma_2, \gamma_3)\ Q^0(\gamma_1, \gamma_2, -\gamma_3)$ in the new coordinates

$$\alpha = \alpha(\gamma),\quad \gamma = \{\gamma_1,\gamma_2,\gamma_3\},\quad \xi = \xi(\eta),$$

$$\eta = \{\eta_1,\eta_2,\eta_3\}$$

subscript 0 refers to the functions of these new coordinates, and

$$\{e^{i\langle\alpha(\gamma),\xi(\eta)\rangle}\}_k^+ = \left(\frac{1}{2\pi i}\int_{-\infty+i0}^{\infty+i0}\frac{e^{i\langle\alpha(\gamma),\xi(\eta)\rangle}}{\gamma_3-\overset{+}{\gamma}_3}d\gamma_3\right)_k, \tag{9}$$

$$\operatorname{Im}\overset{+}{\gamma}_3>0$$

according to the application procedure of generalized factorization [1].

Depending on the representation of the space-transformation group determined by the geometry of the local area of the boundary Γ_2 of the domain Ω, relation (9) generates special functions that are components of the group representation [5, 6]. The subscript is the number of that component of the representation vector of the taken transformation group which that is retained after factorization. In particular, for the rotation group of a sphere in the three-dimensional space,

$$\alpha_1 = \gamma_3\sin\gamma_1\cos\gamma_2,\quad \alpha_2 = \gamma_3\sin\gamma_1\sin\gamma_2, \tag{10}$$

$$\alpha_3 = \gamma_3\cos\gamma_1.$$

Bessel functions of half-integer orders and spherical functions arise. For the rotation of a circle on a plane, which corresponds to problems on a plane or problems for cylindrical domains,

$$\alpha_1 = \gamma_3\cos\gamma_2,\quad \alpha_2 = \gamma_3\sin\gamma_2,\quad \alpha_3 = \gamma_1.$$

Bessel functions of integer orders and trigonometric functions arise.

Exterior forms under coordinate transformations are multiplied by the corresponding Jacobian.

We emphasize that the origins of old and new coordinates need not coincide with each other.

Note 1. Classical factorization is a particular case of generalized factorization. Classical factorization provides projectors onto half-spaces separated by a plane. This factorization is generated by the additive group of the space translation parallel to the factorization plane.

Its representations are specified by exponentials. As was mentioned above, generalized factorization provides projectors on complex-geometry domains different from half-spaces. These domains can be separated by complex surfaces. Coordinate surfaces formed by transformation groups can be the representations of these domains. For motion groups of the three-dimensional space, in particular, for the rotation group, these are spheres, cylinders, and disks.

In the limit of infinite radii γ_3 in the boundary area Γ_1 in the representation of the last groups, demarcating surfaces degenerate to the plane corresponding to classical factorization. In addition, Bessel and spherical functions go over to exponentials with an increase in arguments.

This note explains why generalized factorization provides more possibilities for analysis of boundary value problems in domains with a complex boundary. Indeed, if classical factorization is applicable to a domain, generalized factorization is also applicable. The counter statement is not always true.

If the boundary value problem that is analyzed by applying generalized factorization is formulated more generally than in [2], one can prove that the sets of integral equations (7) and (8) reduce generally to normally solvable sets of second-kind integral equations rather than to Fredholm (zero index) equations. They can be regularized by the procedures applied in [2] with additional determination of the kernel and cokernel of the operator, which have a definite physical meaning.

Thus, the sets of integral equations (7) and (8) reduce to the set of integral equations of the form

$$(\mathbf{I} + \mathbf{A})\mathbf{g} = \mathbf{B}\mathbf{f}. \qquad (11)$$

The vector function **g** is sought in the same spaces as in [2].

According to the above discussion, the number of independent equations in set (11) can be equal to, lower than, or larger than the number of unknowns.

As will be proved below, boundary conditions in Eqs. (1) are satisfied under relations (11).

Note 2. As follows from the above discussion, the method is applicable to the set of differential equations (1) of any finite order.

Some phenomena, such as an increase in seismicity, multicomponent pollution of the environment with impurities chemically reacting in the atmosphere, and pollutions caused by inundations flushing surface ground layers, are multifactor and are described by many coupled partial differential equations and coupled boundary conditions [11–15].

The normal solvability of the operator on the left-hand side of Eqs. (11) and appearance of the defect numbers, kernel, and cokernel of this operator are the manifestations of specific physical effects, such as localizations, resonances, and inconsistencies of different-type boundary conditions of different types, which are determined by physical processes. In view of this circumstance, the method proposed above is also a convenient tool for the analytical analysis of such problems.

Note 3. The choice of local coordinate systems for an approximate solution of the boundary value problem is determined by the requirement of a higher -order contact of the approximating surface with the boundary Γ. In particular, for the boundary part Γ_1 with nonnegative curvature, a Cartesian local coordinate system is appropriate at flattening points as in [2]. It can be also used at positive-curvature points. However, a local coordinate system whose coordinate surface touches the convex element of the surface Γ_1 is more appropriate at these points. For the boundary part Γ_2 with negative curvature, it is appropriate to select transformation groups such that their representations provide coordinate surfaces touching the negative-curvature surface element. This can be sometimes be achieved by a change of the coordinate origin of the transformations of the same group.

ACKNOWLEDGMENTS

This work was supported by the Ministry of Education of the Russian Federation (project nos. E02-4.0-190, Z/N-241, 379, 380, GN-374), the R2003YuG Program, the Russian Foundation for Basic Research (project nos. 03-01-96537, 03-01-96527, 03-01-96519, 03-01-96584), the “Integratsiya” Program (project no. B0121), and the US Civilian Research and Development Foundation for the Independent States of the Former Soviet Union (grant no. REC-004).

REFERENCES

1. V. A. Babeshko, *Generalized Factorization Method in Spatial Dynamic Mixed Problems of Elasticity Theory* (Nauka, Moscow, 1984).
2. V. A. Babeshko and O. M. Babeshko, Dokl. Akad. Nauk **389**, 184 (2003) [Dokl. Phys. **48**, 134 (2003)].
3. I. Ts. Gokhberg and I. A. Fel’dman, *Projection Methods of Solution of Wiener-Hopf Equations* (Akad. Nauk Mold. SSR, Kishinev, 1967).
4. B. Noble, *Methods Based on the Wiener-Hopf Technique for the Solution of Partial Differential Equations* (Pergamon Press, Oxford, 1958; Inostrannaya Literatura, Moscow, 1962).
5. N. Ya. Vilenkin, *Special Functions and the Theory of Group Representations* (Am. Math. Soc., Providence, R.A., 1968; Nauka, Moscow, 1991).
6. I. M. Gel’fand, M. I. Graev, and N. Ya. Vilenkin, *Integral Geometry and Representation Theory* (Fizmatgiz, Moscow, 1962; Academic, New York, 1966).
7. V. A. Babeshko, A. V. Pavlova, S. V. Ratner, and R. Vil’yams, Dokl. Akad. Nauk **382**, 625 (2002) [Dokl. Phys. **47**, 141 (2002)].

8. S. Agmon, A. Douglis, and L. Nirenberg, *Estimates Near the Boundary for Solution of Elliptic Partial Differential Equations Satisfying General Boundary Conditions* (New York, 1959; Inostrannaya Literatura, Moscow, 1962).
9. B. V. Shabat, *Introduction to the Complex Analyses* (Nauka, Moscow, 1985).
10. V. S. Vladimirov, *Methods of the Theory of Functions of Many Complex Variables* (Nauka, Moscow, 1964; MIT Press, Cambridge, Mass., 1966).
11. M. A. Sadovskiĭ, L. S. Bolkhovitinov, and V. F. Pisarenko, *Deformation of Geophysical Environment and Seismic Process* (Nauka, Moscow, 1987).
12. W. Nowacki, *Electromagnetic Effects in Solids* (PWN, Warsaw, 1983; Mir, Moscow, 1986).
13. V. M. Sorokin and G. V. Fedorovich, *Physics of Slow MHD-Waves in Ionospheric Plasma* (Énergoizdat, Moscow, 1982).
14. G. V. Vaĭsblat and S. A. Petrova, in *Problems of Climatology and Atmosphere Pollution* (Gidrometeoizdat, Moscow, 1980).
15. A. M. Nikanorov, *Gidrokhimiya* (Gidrometeoizdat, St. Petersburg, 2001).

Translated by R. Tyapaev

Doklady Physics, Vol. 48, No. 9, 2003, pp. 517–521. Translated from Doklady Akademii Nauk, Vol. 392, No. 2, 2003, pp. 190–194.
Original Russian Text Copyright © 2003 by Voropayeva, Moshkin, Chernykh.

MECHANICS

Internal Waves Generated by Turbulent Wakes in a Stably Stratified Medium

O. F. Voropayeva,* N. P. Moshkin, and G. G. Chernykh*****

Presented by Academician Yu.I. Shokin February 26, 2003

Received March 17, 2003

Turbulent wakes are known to generate internal waves in stratified media [1–5]. For a relatively weak stratification, a turbulent wake first evolves almost similarly to that in a homogeneous fluid and expands symmetrically. However, buoyancy forces hinder the vertical turbulent diffusion; therefore, the wake flattens at large distances from the body and ceases to grow in the vertical direction. Since the fluid density is distributed more uniformly within the wake than outside it due to the turbulent mixing, the buoyancy forces tend to reconstruct the previous state of the stable stratification. As a result, convective flows intensely generating internal waves arise in the plane perpendicular to the wake axis [2]. Investigations of turbulent wakes and internal waves induced by them are reviewed in [6–8].

Analysis of numerical simulations of the dynamics of internal waves generated by turbulent wakes shows that waves induced by turbulent wakes behind self-propelled bodies were considered in detail both for a linearly stratified fluid [2, 7, 8] and for pycnocline [6]. At the same time, internal waves in wakes behind towed bodies have not been adequately studied [9, 10].

In this study, we describe our numerical model of internal waves generated by turbulent wakes in a stably stratified medium and compare the parameters of the internal waves induced by turbulent wakes behind towed bodies and self-propelled bodies.

1. FORMULATION OF THE PROBLEM

To describe the flow in the far turbulent wake behind a body of revolution in a stably stratified medium, we use the following parabolized set of averaged equations of motion, incompressibility, and continuity in the Oberbeck–Boussinesq approximation:

$$U_0\frac{\partial U_{\mathrm{d}}}{\partial x} + V\frac{\partial U_{\mathrm{d}}}{\partial y} + W\frac{\partial U_{\mathrm{d}}}{\partial z} = \frac{\partial}{\partial z}\langle u'v'\rangle + \frac{\partial}{\partial z}\langle u'w'\rangle, \quad (1)$$

$$U_0\frac{\partial V}{\partial x} + V\frac{\partial V}{\partial y} + W\frac{\partial V}{\partial z} = -\frac{1}{\rho_0}\frac{\partial\langle p_1\rangle}{\partial y} - \frac{\partial}{\partial y}\langle v'^2\rangle - \frac{\partial}{\partial z}\langle v'w'\rangle, \quad (2)$$

$$U_0\frac{\partial W}{\partial x} + V\frac{\partial W}{\partial y} + W\frac{\partial W}{\partial z} = -\frac{1}{\rho_0}\frac{\partial\langle p_1\rangle}{\partial z} - \frac{\partial}{\partial y}\langle v'w'\rangle - \frac{\partial}{\partial z}\langle w'^2\rangle - g\frac{\langle\rho_1\rangle}{\rho_0}, \quad (3)$$

$$U_0\frac{\partial\langle\rho_1\rangle}{\partial x} + V\frac{\partial\langle\rho_1\rangle}{\partial y} + W\frac{\partial\langle\rho_1\rangle}{\partial z} + W\frac{d\rho_s}{dz} = -\frac{\partial}{\partial y}\langle v'\rho'\rangle - \frac{\partial}{\partial z}\langle w'\rho'\rangle, \quad (4)$$

$$\frac{\partial V}{\partial y} + \frac{\partial W}{\partial z} = 0. \quad (5)$$

Here, U_0 is the velocity of the unperturbed fluid; $U_{\mathrm{d}} = U_0 - U$ is the defect of the averaged longitudinal component of the velocity; $U = U_1$, $V = U_2$, and $W = U_3$ are, respectively, the x, y, and z components of the averaged velocity; p_1 is the deviation of pressure from the hydrostatic pressure induced by the stratification ρ_{s}; g is the acceleration of gravity; $\langle\rho_1\rangle$ is the averaged defect of density, where $\rho_1 = \rho - \rho_{\mathrm{s}}$; $\rho_{\mathrm{s}} = \rho_{\mathrm{s}}(z)$ is the density of unperturbed fluid: $\frac{d\rho_{\mathrm{s}}}{dz} \le 0$ (stable stratification); $\rho_0 = \rho_{\mathrm{s}}(0)$; the prime denotes pulsation components; and the angle brackets mean averaging. The coordinate system is connected with the moving body so that the velocity of the body is equal to $-U_0$, and the z axis is directed upwards opposite to gravity. The fluid density is con-

---

Institute of Computational Technologies,
Siberian Division, Russian Academy of Sciences,
pr. Akademika Lavrent’eva 6,
Novosibirsk, 630090 Russia
Suranaree University of Technology, School of Mathematics,
Institute of Science,
Nakhom Ratchasima, 30000 Thailand
* *e-mail: vorop@lchd.ict.nsc.ru*
** *e-mail: moshkin@math.sut.ac.th*
*** *chernykh@lchd.ict.nsc.ru*

1028-3358/03/4809-0517$24.00 © 2003 MAIK “Nauka/Interperiodica”

sidered as a linear function of temperature, and stratification is assumed to be weak. The terms with molecular viscosity and diffusion in Eqs. (1)–(4) and a value of $\frac{\partial U}{\partial x}$ in Eq. (5) are assumed small and rejected as in [6–8].

The set of Eqs. (1)–(5) is unclosed. To close it, we use the modified e–ε model of turbulence, where unknown Reynolds stresses $\langle u_i'^2 \rangle$ $(i = 1, 2, 3)$, $\langle u'v' \rangle = \langle u_1' v_2' \rangle$, and $\langle u'w' \rangle = \langle u_1' u_3' \rangle$, the turbulent fluxes, and the variance of fluctuations of the density field are determined from the algebraic relationships [11]

$$\frac{\langle u_i'u_j' \rangle}{e} = \frac{2}{3}\delta_{ij} + \frac{1-c_2}{c_1}\left(\frac{P_{ij}}{\varepsilon} - \frac{2}{3}\delta_{ij}\frac{P}{\varepsilon}\right) + \frac{1-c_3}{c_1}\left(\frac{G_{ij}}{\varepsilon} - \frac{2}{3}\delta_{ij}\frac{G}{\varepsilon}\right), \tag{6}$$

$$P_{ij} = -\left\{\langle u_i'u_k' \rangle \frac{\partial U_j}{\partial x_k} + \langle u_j'u_k' \rangle \frac{\partial U_i}{\partial x_k}\right\}, \tag{7}$$

$$G_{ij} = \frac{1}{\rho_0}(\langle u_i'\rho' \rangle g_i + \langle u_j'\rho' \rangle g_i), \quad i, j, k = 1, 2, 3,$$

$$\mathbf{g} = (g_1, g_2, g_3) = (0, 0, -g), \quad 2P = P_{ii},$$
$$2G = G_{ii},$$

$$-\langle u'\rho' \rangle = \frac{e}{c_{1\mathrm{T}}\varepsilon}\left[\langle u'w' \rangle \frac{\partial\langle\rho\rangle}{\partial z} + (1 - c_{2\mathrm{T}})\langle w'\rho' \rangle \frac{\partial U}{\partial z}\right], \tag{8}$$

$$-\langle v'\rho' \rangle = \frac{\langle v'^2 \rangle}{c_{1\mathrm{T}}}\frac{e}{\varepsilon}\frac{\partial\langle\rho\rangle}{\partial y}, \tag{9}$$

$$-\langle w'\rho' \rangle = \frac{e}{c_{1\mathrm{T}}\varepsilon}\left[\langle w'^2 \rangle \frac{\partial\langle\rho\rangle}{\partial z} + (1 - c_{2\mathrm{T}})\frac{g}{\rho_0}\langle \rho'^2 \rangle\right], \tag{10}$$

$$\langle \rho'^2 \rangle = -\frac{2}{c_{\mathrm{T}}}\frac{e}{\varepsilon}\langle w'\rho' \rangle \frac{\partial\langle\rho\rangle}{\partial z}. \tag{11}$$

From now on, summation over repeating subscripts is implied. The turbulence energy e, dissipation rate ε, and Reynolds shear stress $\langle v'w' \rangle$ are determined from the differential equations

$$U_0\frac{\partial e}{\partial x} + V\frac{\partial e}{\partial y} + W\frac{\partial e}{\partial z} = \frac{\partial}{\partial y}K_{\mathrm{e}y}\frac{\partial e}{\partial y} + \frac{\partial}{\partial z}K_{\mathrm{e}z}\frac{\partial e}{\partial z} + P + G - \varepsilon, \tag{12}$$

$$U_0\frac{\partial \varepsilon}{\partial x} + V\frac{\partial \varepsilon}{\partial y} + W\frac{\partial \varepsilon}{\partial z} = \frac{\partial}{\partial y}K_{\varepsilon y}\frac{\partial \varepsilon}{\partial y} + \frac{\partial}{\partial z}K_{\varepsilon z}\frac{\partial \varepsilon}{\partial z} + c_{\varepsilon 1}\frac{\varepsilon}{e}(P + G) - c_{\varepsilon 2}\frac{\varepsilon^2}{e}, \tag{13}$$

$$U_0\frac{\partial\langle v'w' \rangle}{\partial x} + V\frac{\partial\langle v'w' \rangle}{\partial y} + W\frac{\partial\langle v'w' \rangle}{\partial z} = \frac{\partial}{\partial y}K_{\mathrm{e}y}\frac{\partial\langle v'w' \rangle}{\partial y} + \frac{\partial}{\partial z}K_{\mathrm{e}z}\frac{\partial\langle v'w' \rangle}{\partial z} + (1 - c_2)P_{23} + (1 - c_2)G_{23} - c_1\frac{\varepsilon}{e}\langle v'w' \rangle. \tag{14}$$

The turbulent viscosity coefficients are determined from Eq. (6) by taking into account the features of the wake under consideration:

$$K_{\mathrm{e}y} = \frac{1-c_2}{c_1}\frac{e\langle v'^2 \rangle}{\varepsilon}, \quad K_{\varepsilon y} = \frac{K_{\mathrm{e}y}}{\sigma},$$

$$K_{\mathrm{e}z} = \frac{\left[(1-c_2)e\langle w'^2 \rangle - \frac{(1-c_3)(1-c_{2T})}{c_{1\mathrm{T}}}\frac{g}{\rho_0}\frac{e^2}{\varepsilon}\langle w'\rho' \rangle\right]}{c_1\varepsilon\left(1 - \frac{(1-c_3)}{c_1 c_{1\mathrm{T}}}\frac{g}{\rho_0}\frac{e^2}{\varepsilon^2}\frac{\partial\langle\rho\rangle}{\partial z}\right)}, \quad K_{\varepsilon z} = \frac{K_{\mathrm{e}z}}{\sigma}.$$

In this case,

$$-\langle u'v' \rangle = K_{\mathrm{e}y}\frac{\partial U}{\partial y}, \quad -\langle u'w' \rangle = K_{\mathrm{e}z}\frac{\partial U}{\partial z}.$$

The empirical constants were taken as [11] $c_1 = 2.2$, $c_2 = c_3 = 0.55$, $c_{1\mathrm{T}} = 3.2$, $c_{2\mathrm{T}} = 0.5$, $c_{\mathrm{T}} = 1.25$, $c_{\varepsilon 1} = 1.45$, $c_{\varepsilon 2} = 1.9$, $c_{\mathrm{s}} = 0.22$, and $\sigma = 1.3$. The above mathematical model is used because it is simply realizable, while it includes the anisotropy of the characteristics of turbulence in the wake in a stably stratified fluid. In addition, contrary to the model used in [9, 10], this model satisfactorily describes the turbulent flow in the wake behind a self-propelled body not only in the linearly stratified medium [7], but also in pycnocline [6].

The marching variable x in Eqs. (1)–(4) and (12)–(14) plays the role of time: $t = x/U_0$. At the distance x_0 from the body, we set the initial conditions consistent with the experimental data on the evolution of turbulent wakes in a homogeneous fluid [12, 13]. We set the unperturbed-flow conditions as the boundary conditions at large distances from the wake axis (in the plane orthogonal to the direction of the body motion).

The variables in the problem reduce to the dimensionless form with the body diameter D and free-stream velocity U_0 as the scales of length and velocity, respectively (asterisk denotes dimensionless values). In this case, the characteristic parameters of the wake in a stratified fluid—the density Froude number $\mathrm{F_D}$ and Väisälä–Brunt period T—are determined as follows:

$$\mathrm{F_D} = \frac{U_0 T}{D}, \quad T = \frac{2\pi}{\sqrt{ag}}; \quad a = -\frac{1}{\rho_0}\frac{d\rho_s}{dz}, \quad z = 0.$$

The finite difference calculation algorithm is based on the method of splitting in terms of spatial variables; the detailed description of this algorithm was given in [6, 7].

The mathematical model was tested in the series of numerical calculations, whose results were compared with the experimental data [12, 13] on the degeneration of wakes behind self-propelled bodies and towed bodies in homogeneous and linearly stratified media ($\mathrm{F_D} = 31$). The axial values obtained for both the defect of the averaged-velocity longitudinal component and the turbulence energy agree with experimental data. As an example, we compare (Fig. 1) the calculated and measured values of $U_\mathrm{D}^* = \dfrac{U_\mathrm{D}}{U_0} = \dfrac{U_\mathrm{d}(x, 0, 0)}{U_0}$ for a momentumless wake.

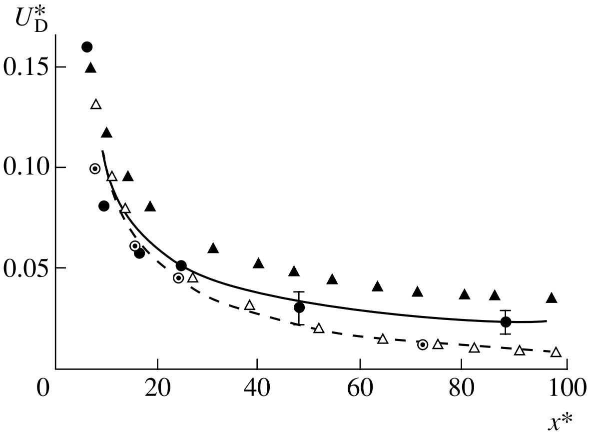

Fig. 1. Defect of the longitudinal averaged-velocity component vs. the distance from the body in the homogeneous liquid (open circles are the experimental data, open triangles are the calculations from [13], and the dashed lines are our calculations) and in the linearly stratified fluid (closed circles are the experimental data, closed triangles are the calculations [13], and the solid lines are our calculations for $\mathrm{F_D} = 31$).

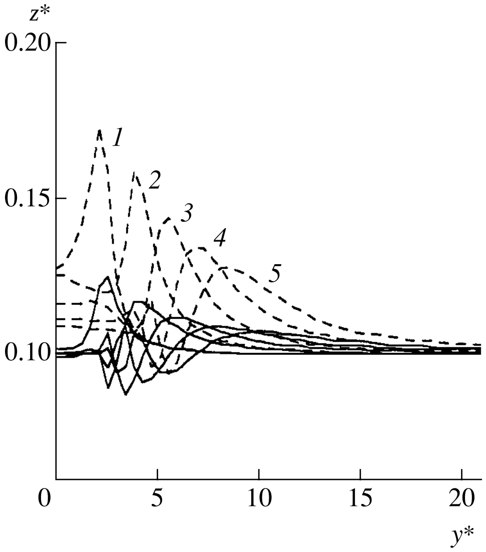

Fig. 2. Density profiles $\rho_0 - \langle\rho\rangle = \rho_0 - \rho_s\,(0.1D)$; $\rho_s = \rho_0(1 - az)$; $y^* = \dfrac{y}{D}$, and $z^* = \dfrac{z}{D}$ for the time $t/T =$ (*1*) 1, (*2*) 2, (*3*) 3, (*4*) 4, and (*5*) 5. The solid and dashed lines correspond to the self-propelled body and a towed body, respectively.

2. RESULTS OF CALCULATION

To analyze the internal waves generated by turbulent wakes in a stably stratified medium, we performed the numerical experiments with the Froude number $\mathrm{F_D} = 565$ corresponding to the conditions of one of the laboratory experiments in [12].

The pattern of internal waves obtained in the calculations is illustrated by the time evolution of density profiles (Figs. 2, 3). In Fig. 2, we compare internal waves induced by turbulent wakes behind self-propelled bodies and towed bodies in the linearly stratified medium. Since similarity in the density Froude number [7] takes place for the linear stratification, the result obtained is valid for an arbitrary sufficiently large Froude number. It is seen that the amplitude of internal waves generated in the wake behind the towed body is much higher than that for the waves in the wake behind a self-propelled body.

A similar behavior is also observed in the medium with nonlinear stratification. As an example, we consider the evolution of a turbulent wake in the pycnocline when turbulent wakes induce solitary internal waves, whose amplitudes are much larger than those for the linear stratification [4, 6]. Figure 3 shows the density profiles calculated for the pycnocline for various times (we chose the same level as in Fig. 2). It is seen that the difference in internal-wave amplitudes behind self-propelled bodies and towed bodies is also very large in this case. The ratio of internal-wave amplitudes for $F_\mathrm{D} = 280$, as well as the ratio obtained in the calculations with other nonlinear density distributions in an unperturbed fluid, is also close to that shown in Fig. 3.

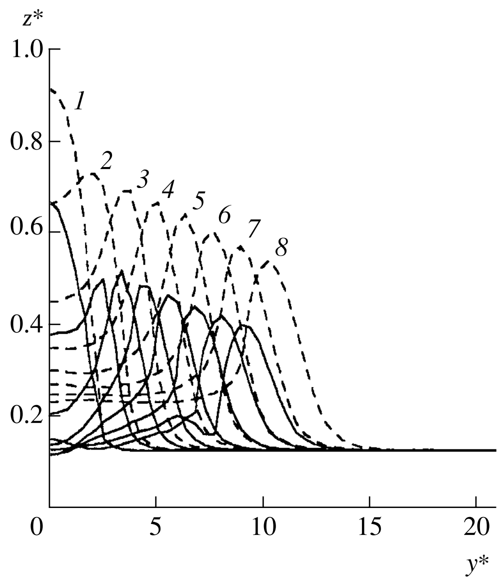

Fig. 3. Density profiles $\rho_0 - \langle\rho\rangle = \rho_0 - \rho_s$ (0.1*D*) in the pycnocline $\{\rho_s = \rho_0 (1 - a\beta\tanh\left(\frac{z}{\beta}\right), \beta = 0.15D\}$ for the time *t*/*T* = (*1*) 1, (*2*) 2, (*3*) 3, (*4*) 4, (*5*) 5, (*6*) 6, (*7*) 7, and (*8*) 8. The solid and dashed lines correspond to the self-propelled body and towed body, respectively.

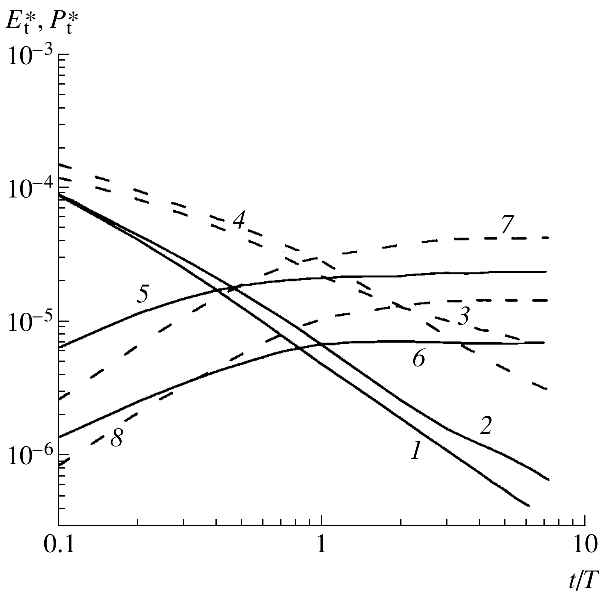

Fig. 4. Time dependence of the (*1*–*4*) total turbulence energy E_t^* and (*5*–*8*) total internal-wave energy P_t^*. Curves *1*, *3*, *5*, and *7* correspond to linear stratification, and curves *2*, *4*, *6*, and *8* corresponds to pycnocline. The solid and dashed lines are for the self-propelled body and towed body, respectively.

Thus, the calculations show that the turbulent wake behind a towed body generates internal waves of a much larger amplitude than that for the case of a self-propelled body. This fact can be explained by substantial distinctions in the evolution of axisymmetric turbulent wakes behind towed bodies and self-propelled bodies in a homogeneous fluid (see, e.g., [14]). In particular, the self-similar wake behind a towed body is characterized by the degeneration laws:

$$e_0(x) = e(x, 0, 0) \sim x^{-4/3}, \quad U_d(x, 0, 0) \sim x^{-2/3}, \quad l(x) \sim x^{1/3},$$

where $l(x)$ is the characteristic wake size. For the self-similar wake behind a self-propelled body, we have

$$e_0(x) \sim x^{-1.5}, \quad U_d(x, 0, 0) \sim x^{-1.5}, \quad l(x) \sim x^{1/4}.$$

Such different behaviors of the characteristics of these wakes are caused by their significantly different structures. In the wake behind the towed body, the generation of the turbulence energy due to gradients in the averaged flow is substantial. In the momentumless wake, the virtually shear-free flow mode [15] is realized at distances as short as about 10*D*. Since the turbulent wake in a stratified medium at the initial stage is developed as in a homogeneous fluid, turbulence in the wake behind the towed body mixes a large fluid mass. In this case, gravity initiates the generation of internal waves of a larger amplitude than that in the wake behind the self-propelled body. This statement is illustrated in Fig. 4, where we show the time dependence of the dimensionless total turbulence energy $E_t^*(t)$ and total internal-wave energy $P_t^*(t)$:

$$E_t^*(t) = \iint_0^{\infty} e^* dy^* dz^*,$$

$$P_t^*(t) = \iint_0^{\infty} \left(\frac{V^{*2} + W^{*2}}{2} + \frac{4\pi^2}{F_D^2} \langle \rho_1 \rangle^* z^* \right) dy^* dz^*.$$

The principal results of this study are as follows. We developed the numerical model of internal waves generated by turbulent wakes in a stably stratified medium. The turbulent wake behind a towed body was shown to generate internal waves of a substantially larger amplitude than that behind a self-propelled body.

ACKNOWLEDGMENTS

This work was supported by the Russian Foundation for Basic Research (project no. 01-01-00783) and the Russian Academy of Sciences, Siberian Division (integration project no. 2000-1).

REFERENCES

1. A. H. Schooley and R. W. Stewart, J. Fluid Mech. **15**, Part 1, 83 (1963).
2. O. F. Vasil'ev, B. G. Kuznetsov, Yu. M. Lytkin, and G. G. Chernykh, Izv. Akad. Nauk SSSR, Mekh. Zhidk. Gaza, No. 3, 45 (1974).

3. A. M. Trokhan and Yu. D. Chashechkin, in *Short Texts of Reports of 7th All-Union Symposium on Diffraction and Propagation of Waves, Rostov-on-Don, 1977* (Akad. Nauk SSSR, Moscow, 1977), Vol. 3, p. 186.
4. H. E. Gilreath and A. Brandt, AIAA Pap. **1704**, 12 (1983).
5. Yu. D. Chashechkin, in *Preprints of 4th International Symposium on Stratified Flows, June 29-July 2, Grenoble, 1994*, Vol. 2, Sess. B4, No. 29, p. 6 (1994).
6. O. F. Voropayeva and G. G. Chernykh, Prikl. Mekh. Tekh. Fiz. **38** (3), 69 (1997).
7. G. G. Chernykh and O. F. Voropayeva, Comput. Fluids **28**, 281 (1999).
8. O. F. Voropayeva and G. G. Chernykh, Mat. Model. **10** (6), 75 (1998).
9. N. P. Moshkin, N. N. Fedorova, and G. G. Chernykh, Vych. Tekhnol. **1** (1), 70 (1992).
10. O. F. Voropayeva, N. P. Moshkin, and G. G. Chernykh, Mat. Model. **12** (10), 77 (2000).
11. W. Rodi, J. Geophys. Res. **92**, 5305 (1987).
12. J. T. Lin and Y. H. Pao, Annu. Rev. Fluid Mech. **11**, 317 (1979).
13. S. Hassid, J. Hydronaut. **14** (1), 25 (1980).
14. V. A. Gorodtsov, Izv. Akad. Nauk SSSR, Ser. Mekh. Zhidk. Gaza, No. 1, 43 (1979).
15. N. V. Aleksenko and V. A. Kostomakha, Prikl. Mekh. Tekh. Fiz., No. 1, 65 (1987).

Translated by V. Bukhanov

Doklady Physics, Vol. 48, No. 9, 2003, pp. 522–527. Translated from Doklady Akademii Nauk, Vol. 392, No. 2, 2003, pp. 195–200.

MECHANICS

Refined Equations of the Average Bending of Three-Layer Shells and Shear Forms of Stability Loss

V. N. Paĭmushin* and V. I. Shalashilin**

Presented by Academician I.F. Obraztsov March 14, 2003

Received March 25, 2003

It is found that stability equations derived in [1, 2] and used in [3] contain only minor parametric terms for description and determination of shear forms of stability loss. The principal cause responsible for these forms of stability loss in the absence of subcritical shear stresses in a filler is the appearance of subcritical transverse compressive stresses. In view of this circumstance, refined geometrically nonlinear equations are constructed for thin three-layer shells with a transversally soft filler. These equations are based on the use of the classical theory of the average bending for outer layers and the linear approximation of transverse displacements for the filler. In contrast to all known variants of the theory of layered shells that are based on the models mentioned above, the derived equations allow the finiteness of the shear strains in the filler, which are caused by possible large mutual tangential displacements of outer layers under their average bending.

Disregarding deformation parametric terms, we derive the linearized stability equations, which are used to obtain the refined solution of the problem of the shear form of stability loss of a three-layered ring at external pressure. It is shown that this form of stability loss can also be realized in the presence of internal pressure. Moreover, it is shown that the shear form of stability loss is realized in the axial direction of the three-layer cylinder shell under the corresponding conditions at the ends in the presence of external or internal pressure.

1. REFINED GEOMETRICALLY NONLINEAR THEORY OF THIN THREE-LAYER SHELLS WITH A TRANSVERSALLY SOFT FILLER

Let the middle surface σ of the filler be attributed to arbitrary curvilinear coordinates x^i and $\mathbf{r}_i = \dfrac{\partial \mathbf{r}}{\partial x^i}$ be the basis vectors on σ. In what follows, we take

$$\mathbf{r}_i^{(k)} = \frac{\partial \mathbf{r}^{(k)}}{\partial x^i} = \frac{\partial}{\partial x^i}[\mathbf{r} - \delta_{(k)}(h + H_{(k)})\mathbf{m}] \approx \mathbf{r}_i,$$

where $2h_{(k)}$ are the thicknesses of the ($k = 1$) lower and ($k = 2$) upper carrier layers, $2h$ is the filler thickness, the unit vector $\mathbf{m}$ normal to σ, together with the vectors $\mathbf{r}_i$, forms the right-hand basis, and $\delta_{(1)} = -\delta_{(2)} = 1$. Similar to [4], the mechanics of the deformation of carrier layers are described in the classical nonlinear theory of average bending, where displacements and shear strains are determined by the formulas

$$\mathbf{U}^{z(k)} = \mathbf{u}^{(k)} + z_{(k)}\mathbf{\Omega}_{(k)} = u_i^{(k)}\mathbf{r}^i + w^{(k)}\mathbf{m} - z_{(k)}\omega_i^{(k)}\mathbf{r}^i, \quad -h_{(k)} \le z_{(k)} \le h_{(k)}, \tag{1.1}$$

$$\varepsilon_{is}^{z(k)} = \varepsilon_{is}^{(k)} + z_{(k)}\chi_{is}^{(k)}, \tag{1.2}$$

where

$$2\varepsilon_{is}^{(k)} = e_{is}^{(k)} + e_{si}^{(k)} + \omega_i^{(k)}\omega_s^{(k)}, \quad 2\chi_{is}^{(k)} = -\nabla_i\omega_s^{(k)} - \nabla_s\omega_i^{(k)}, \tag{1.3}$$

$$e_{is}^{(k)} = \nabla_i u_s^{(k)} - b_{is}w^{(k)}, \quad \omega_i^{(k)} = \nabla_i w^{(k)} + b_i^s u_s^{(k)}. \tag{1.4}$$

Here, ∇_i is the covariant derivative with respect to the metric $a_{is} = \mathbf{r}_i\mathbf{r}_s$ and b_{is} are the covariant components of the second metric tensor on σ.

In the Timoshenko model with allowance for transverse compression, the displacement vector at an arbitrary filler point that was spaced from σ by z before deformation is represented in the form

$$\mathbf{U}^z = \mathbf{u} + z\boldsymbol{\gamma} = (u_i - z\gamma_i)\mathbf{r}^i + (w + z\gamma)\mathbf{m}, \quad -h \le z \le h, \tag{1.5}$$

which is widely used in the mechanics of three- and multilayer shells [4]. In the framework of these representations, transverse compressive strains ε_{33} and transverse shear strains $2\varepsilon_{i3}$, which are constant over thick-

---

* *Research Centre of Dynamics and Strength, Kazan State Technical University, Kazan, Tatarstan, 420111 Russia*

** *Moscow State Aviation Institute (University of Aerospace Technology), Volokolamskoe sh. 4, Moscow, 125080 Russia*

ness, for arbitrary displacements are determined by the formulas [5]

$$\begin{aligned} 2\varepsilon_{i3} &= \omega_i(1+\gamma) + \gamma^s(\delta_{is} + e_{is}), \\ 2\varepsilon_{33} &= 2\gamma + \gamma_i\gamma^i + \gamma^2, \end{aligned} \tag{1.6}$$

where $\omega_i = \nabla_i w + b_i^s u_s$, $e_{is} = \nabla_i u_s - b_{is} w$.

Then, we consider that the filler of the three-layer shell undergoes transverse strains limited by the estimates $2\varepsilon_{i3} \approx \sqrt{\varepsilon}$ and $\varepsilon_{33} \approx \varepsilon$, where ε is much less than unity, for small strains of the middle surface σ of the filler under medium bending, i.e., for $e_{is} \approx \varepsilon$ and $\omega_i \approx \sqrt{\varepsilon}$. Such a form of the strain state of the three-layer shell is possible under its medium bending and when carrier layers can be mutually displaced in the tangential directions under the restrictions $2\varepsilon_{i3} \approx \sqrt{\varepsilon}$. The estimates $2\varepsilon_{i3} \approx \sqrt{\varepsilon}$ and $\varepsilon_{33} \approx \varepsilon$ can be satisfied if γ_i and γ entering into the formula

$$2\varepsilon_{i3} \approx \omega_i + \gamma_i, \quad \varepsilon_{33} \approx \gamma + \underline{\frac{1}{2}\gamma_i\gamma^i}, \tag{1.7}$$

satisfy the inequalities $\gamma \le \varepsilon$ and $\gamma_i \le \sqrt{\varepsilon}$ under which Eqs. (1.7) have the above simple form.

In the framework of models used for the filler and carrier layers, it is sufficient to satisfy the conditions of layer-displacement matching

$$\bar{U}^{z(k)}(z_{(k)} = \delta_{(k)}h_{(k)}) = \bar{U}^z(z = -\delta_{(k)}h).$$

Substituting Eqs. (1.1) and (1.5) into these conditions and taking $u_i^{(k)}$ and $w^{(k)}$ as desired unknown functions, we arrive at the relations

$$\begin{aligned} w &= \frac{1}{2}(w^{(1)} + w^{(2)}), \\ u_i &= \frac{1}{2}(u_i^{(1)} + u_i^{(2)} - h_{(1)}\omega_i^{(1)} + h_{(2)}\omega_i^{(2)}), \end{aligned} \tag{1.8}$$

$$\begin{aligned} \gamma &= \frac{1}{2h}(w^{(2)} - w^{(1)}), \\ \gamma_i &= \frac{1}{2h}(u_i^{(2)} - u_i^{(1)} + h_{(1)}\omega_i^{(1)} + h_{(2)}\omega_i^{(2)}). \end{aligned} \tag{1.9}$$

Using Eq. (1.9), we represent Eqs. (1.6) in the form

$$\begin{aligned} 2\varepsilon_{i3} &= C_{(1)}\omega_i^{(1)} + C_{(2)}\omega_i^{(2)} + \frac{1}{2h}(u_i^{(2)} - u_i^{(1)}), \\ \varepsilon_{33} &= \frac{1}{2}(w^{(2)} - w^{(2)}) + \frac{1}{2}\gamma_i\gamma^i, \end{aligned} \tag{1.10}$$

where $\left(C_{(k)} = \frac{1}{2}\left(1 + \frac{h_{(k)}}{h}\right)\right)$.

To derive the equilibrium equations and boundary conditions, we take the Lagrange variational equation

$$\delta A - \delta U = \delta A - \delta U_{(3)} - \sum_{k=1}^{2} \delta U_{(k)} = 0, \tag{1.11}$$

where δA is the variation of the work of the external forces and $\delta U_{(3)}$ and $\delta U_{(k)}$ are the variations in the deformation potential energies of the filler and carrier layers, respectively. Assuming that the filler is transversally soft [4], we consider that only carrier layers are subjected to external forces and introduce the vectors of given forces and moments

$$\begin{aligned} \mathbf{\Phi}^{(k)} &= \Phi_n^{(k)}\mathbf{n} + \Phi_{n\tau}^{(k)}\boldsymbol{\tau} + \Phi_m^{(k)}\mathbf{m}, \\ \bar{L}^{(k)} &= L_{n\tau}^{(k)}\mathbf{n} + L_n^{(k)}\boldsymbol{\tau}, \end{aligned}$$

applied to the boundary lines of the middle surfaces of external layers $\sigma_{(k)}$. We also introduce the vectors of given surface forces and moments

$$\mathbf{X}^{(k)} = X_{(k)}^i\mathbf{r}_i + X_{(k)}^3\mathbf{m}, \quad \mathbf{M}_{(k)} = M_{(k)}^i\mathbf{r}_i,$$

applied to the points of the surfaces $\sigma_{(k)}$. Here, the unit normal $\mathbf{n}$ and tangential $\boldsymbol{\tau}$ vectors to the contour C of the surface σ are decomposed into basis vectors $\mathbf{r}_i$ and $\mathbf{r}^i$ as $\mathbf{n} = n^i\mathbf{r}_i = n_i\mathbf{r}^i$, $\boldsymbol{\tau} = \boldsymbol{\tau}^i\mathbf{r}_i = \tau_i\mathbf{r}^i$. The variation of the work of the indicated external forces along the corresponding displacements, as well as the expression for $\delta U_{(k)}$, was presented in [1], and

$$\delta U_{(3)} = \iint_\sigma \int_{-h}^{h} (2\sigma^{i3}\varepsilon_{i3} + \sigma^{33}\delta\varepsilon_{33})\,d\sigma dz$$

for the transversally soft filler. Substituting Eqs. (1.7) into the last relation and using Eqs. (1.8) and (1.9), we obtain

$$\begin{aligned} \delta U_{(3)} &= \iint_\sigma [T^{i3}(\delta\gamma_i + \delta\omega_i) + T^{33}(\delta\gamma + \gamma^i\delta\gamma_i)]\,d\sigma \\ &= \iint_\sigma \sum_{k=1}^{2}\Big[-\frac{\delta_{(k)}}{2h}(T^{i3} + T^{33}\gamma^i)\delta u_i^{(k)} \\ &+ \Big(T^{i3}C_{(k)} + \frac{h_{(k)}}{2h}T^{33}\gamma^i\Big)\delta\omega_i^{(k)} - \frac{\delta_{(k)}}{2h}T^{33}\delta\omega_{(k)}\Big]\delta\sigma, \end{aligned} \tag{1.12}$$

where $T^{i3} = 2h\sigma^{i3}$ and $T^{33} = 2h\sigma^{33}$.

When using Eq. (1.12) and corresponding results from [1], variational equation (1.11) after traditional transformations with the use of Eqs. (1.3) and (1.4) provides the set of six nonlinear differential equilibrium equations

$$f^i_{(k)} = \nabla_s T^{is}_{(k)} - S^i_{(k)} b^i_j + \delta_{(k)} \frac{T^{i3} + T^{33}\gamma^i}{2h} + X^i_{(k)} = 0, \qquad (1.13)$$

$$f^3_{(k)} = \nabla_i S^i_{(k)} + T^{is}_{(k)} b_{is} + \frac{\delta_{(k)} T^{33}}{2h} + X^3_{(k)} = 0, \qquad (1.14)$$

where

$$S^i_{(k)} = \nabla_s M^{is}_{(k)} + T^{is}_{(k)} \omega^{(k)}_s + \frac{T^{i3}}{2} + h_{(k)} \frac{T^{i3} + T^{33}\gamma^i}{2h} + M^i_{(k)}, \qquad (1.15)$$

as well as the static boundary conditions in the contour lines of carrier layers.

We note that the shear form of stability loss is determined in Eq. (1.13) by the terms $\frac{T^{i3} + T^{33}\gamma^i}{2h} = \sigma^{i3} + \sigma^{33}\gamma^i$, where the terms $\sigma^{33}\gamma^i$, which appear due to retaining of terms $\frac{\gamma_i \gamma^i}{2}$ in Eq. (1.7), are important.

Using the old notation for increments of introduced functions, we linearize the composed nonlinear equilibrium equations near a certain solution $u^{(k)0}_i$, $w^0_{(k)}$, $T^{ij}_{(k)0}$, $M^{ij}_{(k)0}$, T^{i3}_0, and T^{33}_0. Assuming that the shell is stressed but unstrained until the loss of stability, we arrive at the following set of linearized stability equations:

$$f^i_{(k)} = \nabla_s T^{is}_{(k)} - b^i_j \left(\nabla_s M^{js}_{(k)} + T^{js}_{(k)0} \omega^{(k)}_s + \frac{T^{j3}}{2} \right) + \delta_{(k)} \frac{T^{i3} + T^{33}_0 \gamma^i}{2h} = 0, \qquad (1.16)$$

$$f^3_{(k)} = \nabla_i S^i_{(k)} + T^{is}_{(k)} b_{is} + \delta_{(k)} \frac{T^{33}}{2h} = 0, \qquad (1.17)$$

where

$$S^i_{(k)} = \nabla_s M^{is}_{(k)} - T^{is}_{(k)0} \omega^{(k)}_s + \frac{T^{i3}}{2} + h_{(k)} \frac{T^{i3} + T^{33}_0 \gamma^i}{2h} + M^i_{(k)} \qquad (1.18)$$

in contrast to Eq. (1.15).

2. SHEAR FORM OF STABILITY LOSS IN A THREE-LAYER RING IN THE CIRCLE DIRECTION

We consider a three-layer ring that has a symmetric thickness structure and is in an axisymmetric stress–strain state. Let $2t$ be the thickness of the outer layers, R is the radius of the middle surface of the filler as related to the circle coordinate $x^2 = \theta$, G_{23} is the transverse shear shift modulus of the filler, and $B = 2Et$ and $D = \frac{2t^3 E}{3}$ are the stiffnesses of carrier layers. In this notation and in terms of the physical components of the corresponding vectors and tensors, neutral-equilibrium equations (1.16) and (1.17) are represented in the form

$$\frac{B}{R} \frac{d}{d\theta} \left(\frac{du^{(k)}_2}{d\theta} + w^{(k)} \right) + \delta_{(k)} R (q_2 + \sigma^0_{33} \gamma_2) + S^{(k)}_2 = 0, \qquad (2.1)$$

$$\frac{dS^{(k)}_2}{d\theta} - \frac{B}{R} \left(\frac{du^{(k)}_2}{d\theta} + w^{(k)} \right) + \frac{\delta_{(k)} E_3 R}{2h} (w^{(2)} - w^{(1)}) = 0, \qquad (2.2)$$

$$\sigma_{23} = q_2 = \frac{1}{2h} G_{23} [u^{(2)}_2 - u^{(1)}_2 + (t + h)(\omega^{(1)}_2 + \omega^{(2)}_2)], \qquad (2.3)$$

$$S^{(k)}_2 = -\frac{D}{R^2} \frac{d^2 \omega^{(k)}_2}{d\theta^2} + T^{(k)0}_{22} \omega^{(k)}_2 + (t + h) q_2 + t \sigma^0_{33} \gamma_2, \qquad (2.4)$$

$$\omega^{(k)}_2 = \frac{1}{R} \left(\frac{dw^{(k)}}{d\theta} - u^{(k)}_2 \right), \quad \gamma_2 = \frac{1}{2h} [u^{(2)}_2 - u^{(1)}_2 + t(\omega^{(1)}_2 + \omega^{(2)}_2)] \qquad (2.5)$$

because the undistorted stress–strain state is axisymmetric.

2.1. External Pressure Effect

In Eqs. (2.1) and (2.4), subcritical forces in carrier layers $T^{(k)0}_{22}$ and transverse normal stress σ^0_{33} in the filler at the external pressure $X^{(2)}_3 = -p$, when $X^{(1)}_3 = 0$, are determined by formulas [3, 6]

$$T^{(1)0}_{22} = -\frac{\chi R p}{1 + 2\chi}, \quad T^{(2)0}_{22} = -\frac{(1 + \chi) R p}{1 + 2\chi}, \qquad (2.6)$$

$$\sigma^0_{33} = -\frac{\chi p}{1 + 2\chi}, \qquad (2.7)$$

within the accepted accuracy of the constructed equations. Here, $\chi = \dfrac{E_3R^2}{2Bh}$ is the dimensionless parameter determining the transverse compression.

We represent the unknown functions appearing in Eqs. (2.1)–(2.5) in the form

$$\{w^{(k)}, u_2^{(k)}, q_2\}$$
$$= \{W_n^{(k)}, V_n^{(k)}, Q_n\}\{\sin n\theta, \cos n\theta, \cos n\theta\}^T, \quad (2.8)$$

where $n = 0, 1, 2, \ldots$ are the numbers of half-wavelengths of stability loss. Each number corresponds to a certain branching point of solutions of the original set of constructed nonlinear equations from its linear solution (2.6) and (2.7).

Here we consider the solution for $n = 0$, which describes, as was shown in [3], the shear form of stability loss of the ring for uniform external pressure. Such forms of stability loss, as well as the forms of free and natural oscillations of the three-layer elements of constructions, are accompanied by zero change in the parameters of their stress–strain state. Therefore, setting $\dfrac{d}{d\theta} = 0$ in all equations and relations (2.1)–(2.5), we arrive at the equations

$$-w^{(k)} + \delta_{(k)}\chi(w^{(2)} - w^{(1)}) = 0, \quad (2.9)$$

$$\delta_{(k)}Rq_2^* + T_{22}^{(k)0}\omega_2^{(k)} + hq_2 + tq_2^*$$
$$\approx \delta_{(k)}Rq_2^* + T_{22}^{(k)0}\omega_2^{(k)} + hq_2 = 0, \quad (2.10)$$

where

$$\omega_2^{(k)} = -\frac{u_2^{(k)}}{R}, \quad q_2 = \frac{1}{2h}G_{23}(u_2^{(2)} - u_2^{(1)}), \quad (2.11)$$

$$q_2^* = q_2 + \sigma_{33}^0\gamma_2$$
$$= q_2 + \sigma_{33}^0[u_2^{(2)} - u_2^{(1)} + t(\omega_2^{(1)} + \omega_2^{(2)})]$$
$$\approx \frac{1}{2h}(G_{23} + \sigma_{33}^0)(u_2^{(2)} - u_2^{(1)})$$

with the accuracy $1 + \dfrac{t+h}{R} \approx 1$ and $1 + \dfrac{t}{R} \approx 1$.

The set of Eqs. (2.9) has only trivial solution $w^{(k)} \equiv 0$, and, using Eqs. (2.11) and introducing the notation

$$\alpha = \frac{1}{2h}R^2(G_{23} + \sigma_{33}^0), \quad \beta = \frac{G_{23}R}{2}, \quad (2.12)$$

Eqs. (2.10) reduce to the form

$$(\alpha - \beta - T_{22}^{(1)0})u_2^{(1)} + (-\alpha + \beta)u_2^{(2)} = 0,$$
$$(-\alpha + \beta)u_2^{(1)} + (\alpha + \beta - T_{22}^{(2)})u_2^{(2)} = 0.$$

The condition that these equations have nontrivial solutions provides the formula

$$\alpha = -\beta\frac{T_{22}^{(1)0} - T_{22}^{(2)0}}{T_{22}^{(1)0} + T_{22}^{(2)0}}. \quad (2.13)$$

Substituting Eqs. (2.6) and (2.12) into this formula and taking into account Eq. (2.7), we obtain

$$p_* = \frac{G_{23}(1 + 2\chi)}{\chi} \quad (2.14)$$

with the accuracy $1 = h_0 = 1 + \dfrac{h}{R} \approx 1$. We call it the formula for determining the critical external pressure at which shear stability loss occurs in the three-layer ring, which was described and analyzed (incorrectly, as will be noted below) in [3].

2.2. Internal-Pressure Effect

When the three-layer ring is subjected to internal pressure $X_3^{(1)} = p$ and $X_3^{(2)} = 0$, subcritical ring forces in carrier layers are easily shown to be tensile and determined by the formulas

$$T_{22}^{(2)0} = \frac{\chi Rp}{1 + 2\chi}, \quad T_{22}^{(1)0} = \frac{(1 + \chi)Rp}{1 + 2\chi}, \quad (2.15)$$

while the filler is under compression and the stress σ_{33}^0 in it is also described by Eq. (2.7). Substituting Eqs. (2.12) and (2.15) into Eq. (2.13) and using Eq. (2.7), we arrive at formula (2.14) for p_*. Thus, the shear form of stability loss of the three-layer ring is also possible at internal pressure when the compressive stress in the filler is equal to G_{23}; i.e., $\sigma_{33}^0 = -G_{23}$. In this case, the bending form of stability loss, which was studied in detail in [6] in the presence of external pressure, is however impossible.

2.3. Analysis of the Shear Form of Stability Loss

In the framework of the representation of the displacement vector in the filler in form (1.6) with accuracy $\delta_i^s - zb_i^s \approx \delta_i^s$, the basis vectors in the strain state of the filler are equal to

$$\boldsymbol{\rho}_i^* = \frac{\partial(\mathbf{r} + z\mathbf{m} + \mathbf{u} + z\boldsymbol{\gamma})}{\partial x^i} = \mathbf{r}_i^* + z\boldsymbol{\gamma}_i,$$

$$\boldsymbol{\rho}_3^* = \frac{\partial(\mathbf{r} + z\mathbf{m} + \mathbf{u} + z\boldsymbol{\gamma})}{\partial z} = \mathbf{m} + \boldsymbol{\gamma},$$

where

$$\boldsymbol{\gamma}_i = \frac{\partial\boldsymbol{\gamma}}{\partial x^i}, \quad \mathbf{r}_i^* = \frac{\partial\mathbf{r}^*}{\partial x^i} = \frac{\partial(\mathbf{r} + \mathbf{u})}{\partial x^i}.$$

The stress vector $\boldsymbol{\sigma}^3$ acting on a z = const area of the filler in its strain state can be written in the form $\boldsymbol{\sigma}^3 = \sigma^{i3}\boldsymbol{\rho}_i^* + \sigma^{33}\boldsymbol{\rho}_3^*$, which can be simplified as $\boldsymbol{\sigma}^3 \approx \sigma^{i3}\mathbf{r}_i^* + \sigma^{33}(\mathbf{m} + \boldsymbol{\gamma})$ in view of the accepted model. Since $\mathbf{r}_i^* = \mathbf{r}_i + \omega_i\mathbf{m}$ for the middle bending of the shell [5], we have

$$\begin{aligned}\boldsymbol{\sigma}^3 &= \sigma^{i3}(\mathbf{r}_i + \omega_i\mathbf{m}) + \sigma^{33}(\mathbf{m} + \gamma^i\mathbf{r}_i)\\ &= (\sigma^{i3} + \sigma^{33}\gamma^i)\mathbf{r}_i + (\sigma^{i3} + \sigma^{33}\omega_i)\mathbf{m}.\end{aligned} \tag{2.16}$$

From Eq. (2.16), the tangential components σ_*^{i3} of the vector $\boldsymbol{\sigma}^3$ in the unstrained basis $\mathbf{r}_i$, $\mathbf{m}$ are determined by the formula

$$\sigma_*^{i3} = \sigma^{i3} + \sigma^{33}\gamma^i. \tag{2.17}$$

These stresses normalized to the forces $T^{i3} + T^{33}\gamma^i$ enter both into the equilibrium equations for all forces applied to carrier layers in the projections on the basis vectors $\mathbf{r}_i$ [Eqs. (1.13)] and into Eqs. (1.15), which present the equations of moment equilibrium for composite elements of carrier layers consisting of the elements of carrier layers with thicknesses $2h_{(k)}$ and filler of the thickness h. Expression (2.17) for the three-layer ring after linearization near the solution given by Eqs. (2.6) and (2.7) takes the form

$$\sigma_{23}^* = q_2^* \approx \frac{1}{2h}(G_{23} + \sigma_{33}^0)(u_2^{(2)} - u_2^{(1)}).$$

Here, it is seen that, if $\sigma_{33}^0 = -G_{23}$, then $q_2^* = 0$ and $u_2^{(2)} - u_2^{(1)}$ is indefinite; i.e., the set of adjoining equilibrium states appears. In other words, the filler loses stability, and carrier layers can turn with respect to each other as rigid bodies; i.e., shear stability loss for the ring occurs. In this case, the filler acts on carrier layers with zero forces q_2^* both before and at the time of stability loss.

Thus, the three-layer ring becomes unstable against shear in the case under consideration at transverse compression when the stress σ_{33}^0 is equal to $-G_{23}$.

3. NECESSARY ACCURACY OF CONSTRUCTION OF NONLINEAR AND LINEARIZED EQUATIONS OF THE THEORY OF THREE-LAYER SHELLS FOR ANALYSIS OF SHEAR FORMS OF STABILITY LOSS

If all strain components of the filler are small, i.e., if $2\varepsilon_{i3} \approx \varepsilon$ and $\varepsilon_{33} \approx \varepsilon$, Eqs. (1.7) can be written in the form $2\varepsilon_{i3} = \omega_i + \gamma_i$ and $\varepsilon_{33} = \gamma = \dfrac{w^{(2)} - w^{(1)}}{2h}$. Using them, we again arrive at Eqs. (1.13) and (1.14), where

$$S_{(k)}^i = \nabla_s M_{(k)}^{is} + T_{(k)}^{is}\omega_s^{(k)} + C_{(k)}T^{i3} + M_{(k)}^i$$

contrary to Eq. (1.15).

In application to three-layer shells, the equations thus derived are fully equivalent both to equations from [1] and to similar equations of the theory of layered shells, which are constructed under the assumption of smallness of strains $2\varepsilon_{i3} \approx \varepsilon$ and $\varepsilon_{33} \approx \varepsilon$ in the majority of other works. These equations lead to the equations

$$\delta_{(k)}Rq_2 + T_{22}^{(k)0}\,\omega_2^{(k)} + hq_2 = 0,\ q_2 \approx \frac{1}{2h}G_{23}(u_2^{(2)} - u_2^{(1)})$$

for analysis of the shear form of stability loss of the three-layer ring. Contrary to Eqs. (2.10), the latter equations do not contain the terms $\sigma_{33}^0\gamma_2$. Under the accepted accuracy $1 + h_0 \approx 1$ and in view of Eq. (2.6), these equations lead to the formula [3]

$$p_* = \frac{2}{h_0}G_{23}\left\{1 + \frac{1}{4\chi(1 + \chi)}\right\},$$

which overestimates the critical load of the shear form of stability loss of the three-layer ring by a factor of $1/h_0$ as compared to Eq. (2.14).

Thus, analysis of the above results and results obtained in [3] shows that, to construct two-dimensional geometrically nonlinear equations for description of shear forms of stability loss in the theory of three-layer (generally multilayer) elements of constructions, one must consider finite transverse shear strains of the filler, finite rotation angles of fibers, which are normal to its middle surface before deformation. In the variant proposed in this work, this requirement reduces to the retaining of underlined terms in Eqs. (1.7), which leads to the appearance of terms $T^{33}\gamma^i$ in Eqs. (1.13) and expressions (1.15).

4. SHEAR FORM OF STABILITY LOSS OF A THREE-LAYER CYLINDER SHELL IN THE AXIAL DIRECTION

As was shown in [7], among all forms of free oscillations in three-layer shells, two uncoupled forms that are possible in the absence of restrictions on mutual tangential displacements on the shell contour, i.e., when $u_2^{(2)} - u_2^{(1)} \neq 0$, stand out. They are realized in the shell under zero variability of the parameters of the stress–strain state in directions x^i only due to mutual displacements of outer layers as rigid bodies. By analogy with the forms of oscillations in the cylinder shell under external or internal pressure and above conditions at boundary cuts, the shear form of stability loss must be realized not only in the circular direction, which is studied in Section 2, but also in the axial direction. Indeed, taking zero variability of all functions appearing in the equations for the perturbed state of the cylinder shell in the directions θ and $x^1 = x$, we arrive not only at the problem analyzed in Section 2 but also at the equation $T^{13} + T_0^{33}\gamma^i = 0$. In view of formulas $\sigma^{13} = \dfrac{T^{13}}{2h}$ and $\sigma_0^{33} = \sigma_{33}^0 = \dfrac{T_0^{33}}{2h}$ and kinematic relations $2\varepsilon_{13} = \dfrac{u_1^{(2)} - u_1^{(1)}}{2h}$ and $\gamma^1 = \gamma_1 = \dfrac{u_1^{(2)} - u_1^{(1)}}{2h}$, this equation reduces to the form

$$\frac{1}{2h}(G_{13} + \sigma_{33}^0)(u_2^{(2)} - u_2^{(1)}) = 0.$$

This equation, along with Eq. (2.7), provides the formula

$$p_* = \frac{G_{13}(1+\chi)}{\chi}.$$

Comparison of this formula with formula (2.15) shows that, for the isotropic filler ($G_{13} = G_{23} = G_3$), the critical pressures (external or internal) at which the three-layer cylinder shell loses stability through shear in circular and axial directions coincide with each other with accepted accuracy $1 + h_0 \approx 1$.

ACKNOWLEDGMENTS

This work was supported by the Russian Foundation for Basic Research (project nos. 03-01-00535a).

REFERENCES

1. V. A. Ivanov and V. N. Paĭmushin, Izv. Vyssh. Uchebn. Zaved., Mat., No. 11, 29 (1994).
2. V. N. Paĭmushin and S. N. Bobrov, Mekh. Kompoz. Mater. (Rizh. Politekh. Inst.) **36** (1), 95 (2000).
3. V. N. Paĭmushin, Dokl. Akad. Nauk **378**, 58 (2001) [Dokl. Phys. **46**, 346 (2001)].
4. V. V. Bolotin and Yu. N. Novichkov, *Mechanics of Multilayer Constructions* (Mashinostroenie, Moscow, 1980).
5. K. Z. Galimov, V. N. Paĭmushin, and I. G. Teregulov, *Foundations of Nonlinear Theory of Shells* (Fén, Kazan, 1996).
6. V. N. Paĭmushin, V. A. Ivanov, S. N. Bobrov, and T. V. Polyakova, Mekh. Kompoz. Mater. (Rizh. Politekh. Inst.) **36** (3), 317 (2000).
7. V. N. Paĭmushin, Mekh. Kompoz. Mater. (Rizh. Politekh. Inst.) **37** (3), 289 (2001).

Translated by R. Tyapaev

Doklady Physics, Vol. 48, No. 9, 2003, pp. 528–532. Translated from Doklady Akademii Nauk, Vol. 392, No. 3, 2003, pp. 340–345.
Original Russian Text Copyright © 2003 by Vigdorovich.

MECHANICS

Similarity Laws for the Velocity and Temperature Profiles in the Wall Region of a Turbulent Boundary Layer with Injection and Suction

I. I. Vigdorovich

Presented by Academician G.G. Chernyĭ May 5, 2003

Received May 7, 2003

The presence of a finite number of determining parameters of the problem indicates that the turbulent shear stress is a universal function of the average-velocity gradient and the turbulent heat flux is a universal function of the average-velocity gradient and average-temperature gradient in the wall region of a turbulent boundary layer. This circumstance, along with dimensionality reasons, makes it possible to reduce the equations of momentum and heat transfer to first-order ordinary differential equations for velocity and temperature profiles, which can be easily analyzed in general form. As a result, similarity laws for velocity and temperature, which generalize the known logarithmic distributions to the case of injection and suction, are obtained.

The approach proposed in this work has considerable advantages over the classical method [1], where dynamic equations are not used, and extends the set of wall-turbulence problems, whose similarity laws can be obtained without the formulation of special closing hypothesis.

1. We consider a flow of an incompressible heat-conducting fluid in the wall region of a turbulent boundary layer on a smooth permeable surface. The velocity of injection or suction is considered to be directed along the normal to the wall. In the thin wall region, the transverse gradients of average parameters are much larger than the longitudinal gradients. Therefore, the transfer of momentum and heat in the first approximation is described by the known equations

$$-\langle u'v'\rangle + \nu\frac{du}{dy} = \frac{\tau_w}{\rho} + v_w u, \tag{1.1}$$

$$-\langle \theta'v'\rangle + \chi\frac{d\theta}{dy} = -j_w + v_w(\theta - \theta_w). \tag{1.2}$$

Here, u is the longitudinal component of the average velocity, θ is the average temperature, y is the distance from the wall, ν is the kinematic viscosity, χ is the molecular diffusivity, and v_w, θ_w, τ_w, and j_w are the wall values of the transverse velocity, temperature, shear stress, and temperature flux, respectively.

Temperature is considered as a passive parameter that does not affect flow dynamics. Therefore, Eq. (1.2) in the corresponding notation is the transfer equation for a passive parameter.

Equations (1.1) and (1.2) describe a turbulent flow along an infinite plane, where the transverse velocity and pressure are constant, and other parameters depend only on the distance from the plane. For this flow,

$$\frac{du}{dy} = F_1\left(y, \nu, v_w, \frac{\tau_w}{\rho}\right), \tag{1.3}$$

$$\langle u'v'\rangle = F_2\left(y, \nu, v_w, \frac{\tau_w}{\rho}\right), \tag{1.4}$$

$$\frac{d\theta}{dy} = F_3\left(y, \nu, \chi, v_w, \frac{\tau_w}{\rho}, j_w\right), \tag{1.5}$$

$$\langle \theta'v'\rangle = F_4\left(y, \nu, \chi, v_w, \frac{\tau_w}{\rho}, j_w\right), \tag{1.6}$$

where $F_1, \ldots, F_4$ are certain universal functions. Thus, we assume that the quantities under consideration in the wall region are independent of external parameters of the boundary layer and are completely determined by the conditions on the wall and physical constants of the fluid.

Expressing τ_w/ρ from Eq. (1.3) and j_w from Eq. (1.5) and substituting them into Eqs. (1.4) and (1.6), we arrive at the relations

$$\begin{gathered}\langle u'v'\rangle = G_1\left(y, \nu, v_w, \frac{du}{dy}\right),\\ \langle \theta'v'\rangle = G_2\left(y, \nu, \chi, v_w, \frac{du}{dy}, \frac{d\theta}{dy}\right).\end{gathered} \tag{1.7}$$

Applying the dimensional analysis to functional relations (1.7) and taking into account that a special dimension can be used for temperature as a passive

---

Central Institute of Aviation Motors,
ul. Aviamotornaya 2, Moscow, 111116 Russia

parameter, we obtain

$$\langle u'v'\rangle = -\left(y\frac{du}{dy}\right)^2 S(\mathrm{R}, \beta),$$

$$\langle \theta' v'\rangle = -y^2\frac{d\theta}{dy}\frac{du}{dy}T(\mathrm{R}, \mathrm{Pe}, \beta), \qquad (1.8)$$

$$\mathrm{R} = \frac{y^2}{\nu}\frac{du}{dy}, \quad \mathrm{Pe} = \frac{y^2}{\chi}\frac{du}{dy}, \quad \beta = \frac{v_\mathrm{w}}{R}\frac{dy}{du}.$$

Here, the local Reynolds number R is the characteristic turbulent-to-molecular viscosity ratio and the local Péclet number Pe is the turbulent-to-molecular diffusivity ratio. Let us assume that functions S and T are continuous in their domain of definition, have partial derivatives with respect to all arguments, and satisfy the conditions $S(\infty, 0) \neq 0$, $T(\infty, \infty, 0) \neq 0$.

In the wall variables

$$y_+ = \frac{y}{\nu}\sqrt{\frac{\tau_\mathrm{w}}{\rho}}, \quad u_+ = u\sqrt{\frac{\rho}{\tau_\mathrm{w}}},$$

$$v_+ = v_\mathrm{w}\sqrt{\frac{\rho}{\tau_\mathrm{w}}}, \quad \theta_+ = \frac{\theta_\mathrm{w} - \theta}{j_\mathrm{w}}\sqrt{\frac{\tau_\mathrm{w}}{\rho}}$$

Eqs. (1.1) and (1.2) in view of Eq. (1.8) take the form

$$\left(y_+\frac{du_+}{dy_+}\right)^2 S(\mathrm{R}, \beta) + \frac{du_+}{dy_+} = 1 + v_+u_+, \quad u_+(0) = 0, \qquad (1.9)$$

$$y_+^2\frac{d\theta_+}{dy_+}\frac{du_+}{dy_+}T(\mathrm{R}, \mathrm{Pr}\mathrm{R}, \beta) + \frac{1}{\mathrm{Pr}}\frac{d\theta_+}{dy_+} = 1 + v_+\theta_+, \qquad (1.10)$$

where

$$\theta_+(0) = 0,$$

$$\mathrm{R} = y_+^2\frac{du_+}{dy_+}, \quad \beta = \frac{v_+}{Ry_+}\frac{dy_+}{du_+},$$

and $\mathrm{Pr} = \frac{\nu}{\chi}$ is the molecular Prandtl number.

Thus, the problem reduces to analysis of ordinary differential equation (1.9) for the velocity profile. According to Eq. (1.10), the temperature profile is specified by the integral

$$\ln(1 + v_+\theta_+) = \int\limits_0^{y_+}\frac{\mathrm{Pr}\, v_+ dy_+}{1 + \mathrm{Pr}\mathrm{R}T(\mathrm{R}, \mathrm{Pr}\mathrm{R}, \beta)}. \qquad (1.11)$$

2. For an impermeable wall ($v_+ = 0$), Eq. (1.9) has the solution in the closed form

$$u_+ = \int\limits_0^R\frac{dR}{\sqrt{\mathrm{R}^2S(\mathrm{R}, 0) + \mathrm{R}}} - \frac{\mathrm{R}}{\sqrt{\mathrm{R}^2S(\mathrm{R}, 0) + \mathrm{R}}}, \qquad (2.1)$$

$$y_+ = \sqrt{\mathrm{R}^2S(\mathrm{R}, 0) + \mathrm{R}}, \quad 0 \le \mathrm{R} < \infty,$$

and integral (1.11) takes the form

$$\theta_+ = \int\limits_0^\mathrm{R}\frac{\mathrm{Pr}d\sqrt{\mathrm{R}^2S(\mathrm{R}, 0) + \mathrm{R}}}{1 + \mathrm{Pr}\mathrm{R}\,T(\mathrm{R}, \mathrm{Pr}\mathrm{R}, 0)}. \qquad (2.2)$$

It follows from Eqs. (2.1) and (2.2) and from conditions for the functions S and T that velocity and temperature have logarithmic asymptotic behavior in the outer part of the wall region:

$$u_+ = \frac{1}{\kappa}(\ln y_+ + C_0) + O(y_+^{-\alpha}), \qquad (2.3)$$

$$\theta_+ = \frac{\mathrm{Pr_t}}{\kappa}[\ln y_+ + B(\mathrm{Pr})] + O(y_+^{-\alpha}), \quad \alpha > 0,$$
$$\kappa = \sqrt{S(\infty, 0)}, \quad \mathrm{Pr_t} = \frac{S(\infty, 0)}{T(\infty, \infty, 0)}, \quad y_+ \longrightarrow \infty. \qquad (2.4)$$

The values of von Karman's constant κ, the constant C_0, and turbulent Prandtl number $\mathrm{Pr_t}$ in the logarithmic region must be determined from experiments.

The asymptotic behavior of the function $B(\mathrm{Pr})$ appearing in Eq. (2.4) for small and large molecular Prandtl number can be obtained from integral representation (2.2). In the first case,

$$B(\mathrm{Pr}) = \ln\mathrm{Pr} + b_1 + \ldots, \quad \mathrm{Pr} \to 0,$$

where

$$b_1 = \int\limits_0^1\frac{T(\infty, \infty, 0)d\mathrm{Pe}}{1 + \mathrm{Pe}\,T(\infty, \mathrm{Pe}, 0)} \qquad (2.5)$$

$$-\int\limits_1^\infty\frac{[1 + \mathrm{Pe}(T(\infty, \mathrm{Pe}, 0) - T(\infty, \infty, 0))]d\mathrm{Pe}}{\mathrm{Pe}[1 + \mathrm{Pe}\,T(\infty, \mathrm{Pe}, 0)]} - \ln\kappa.$$

Assuming as in [2] that the turbulent diffusivity is independent of χ (function T is independent of the Péclet number), the calculation of integrals (2.5) yields $b_1 = \ln\left(\frac{\kappa}{\mathrm{Pr_t}}\right)$, which is less than the value proposed in [2] by one unit.

To analyze the other limiting case, we take $T(\mathrm{R}, \mathrm{Pr}\mathrm{R}, 0) = k(\mathrm{Pr})\sqrt{\mathrm{R}} + \ldots$ for $\mathrm{R} \longrightarrow 0$ according to the known estimate $\langle\theta' v'\rangle = O(y^3)$ for $y \longrightarrow 0$. Then, the leading term of the asymptotic expansion for $B(\mathrm{Pr})$ has the form

$$B(\mathrm{Pr}) = b_2\mathrm{Pr}^{2/3} + \ldots, \quad \mathrm{Pr} \longrightarrow \infty,$$

$$b_2 = \frac{\kappa}{\mathrm{Pr_t}}\int\limits_0^\infty\frac{dx}{1 + k(\infty)x^3} = \frac{2\pi\sqrt{3}\kappa}{9\mathrm{Pr}_t k^{1/3}(\infty)}.$$

An approximate formula yielding close values for the coefficient b_2 was proposed in [2].

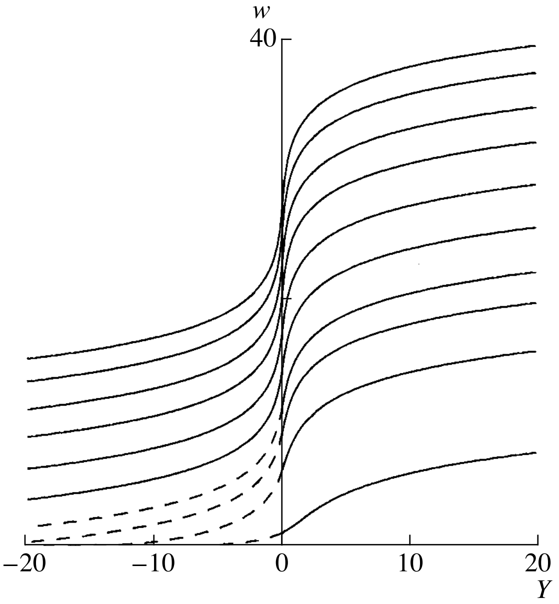

Qualitative pattern of the integral curves of Eq. (3.2) in the upper half-plane.

3. In the general case of nonzero transverse velocity on the wall, introducing the new variables

$$y = \frac{y v_w}{\nu} = v_+ y_+, \quad w = \frac{2}{v_+}\sqrt{1 + v_+ u_+}, \qquad (3.1)$$

we obtain the equation

$$\left(Y\frac{dw}{dY}\right)^2 S(\mathrm{R}, \beta) + \frac{2}{w}\frac{dw}{dY} = 1, \quad w(0) = \frac{2}{v_+}, \qquad (3.2)$$

where

$$\mathrm{R} = \frac{Y^2 w}{2}\frac{dw}{dY}, \quad \beta = \frac{2}{\mathrm{R}Yw}\frac{dY}{dw}.$$

Variables are taken (3.1) so that Eq. (3.2) does not contain the parameter v_+.

The integral curves of Eq. (3.2) are symmetric with respect to the abscissa axis. Therefore, it is sufficient to analyze their behavior in the upper half-plane. The figure shows the qualitative pattern of integral curves [solutions of Eq. (3.2) are constructed for $S = \kappa^2$]. Negative and positive Y values correspond to suction and injection, respectively. Along each curve, w increases from 0 to $+\infty$.

The second-quadrant parts of integral curves along which the variable Y varies from $-\infty$ to zero correspond to the total velocity profiles in the asymptotic boundary layer with suction. This one-dimensional flow, where all average parameters depend only on the distance from the wall, is exactly described by Eq. (1.1) when the boundary condition $u = U_c$ for velocity is imposed in the inflow at $y = \infty$. For this flow, it is obvious that $v_+ = -\sqrt{-\frac{v_w}{U_c}}$. Thus, v_+ for the asymptotic boundary layer is small. This condition is also valid for the general suction case, because velocity u_+ is high at the external boundary of the wall region and the right-hand side of Eq. (1.9) is positive. Therefore, according to initial condition (3.2), only integral curves crossing the ordinate axis at sufficiently large w values are physically meaningful (physically meaningless parts of integral curves are shown in the figure by dashed lines). The velocity profile in the wall region of the boundary layer with suction is generally described by parts of integral curves corresponding to large w values.

All integral curves are physically meaningful in the first quadrant. Small $w(0)$ values correspond to strong injection, i.e., to large v_+ values.

The asymptotic representation of the velocity profile in the outer part of the wall region, where the viscous term and $1/R$-order quantities in Eq. (1.9) can be ignored, has the form

$$\frac{2}{v_+}\left(\sqrt{1 + v_+ u_+} - 1\right) = \frac{1}{\kappa}[\ln y_+ + C(v_+)] + O(y_+^{-\alpha}), \qquad (3.3)$$
$$\alpha > 0, \quad y_+ \to \infty.$$

Here, $C(v_+)$ is a certain universal function. For the injection and suction cases, Eq. (3.3) presents the asymptotic behavior of the solution of Eq. (1.9) for $y_+ \longrightarrow \infty$ and the intermediate asymptotic function corresponding to the outer part the wall region, respectively. Relation (3.3) is a generalization of the logarithmic law for the velocity profile to the injection and suction case and must coincide with Eq. (2.3) for $v_+ = 0$; therefore, $C(0) = C_0$.

The asymptotic representation (3.3) was first found in [3, 4] on the basis of the Prandtl mixing-length formula.

The calculation of integral (1.11) for large y_+ in view of Eq. (3.3) yields

$$\frac{2}{v_+}\left[(1 + v_+\theta_+)^{\frac{1}{2\mathrm{Pr}_t}} - 1\right] + \frac{1}{\kappa}D(v_+, \mathrm{Pr})(1 + v_+\theta_+)^{\frac{1}{2\mathrm{Pr}_t}} \qquad (3.4)$$
$$= \frac{1}{\kappa}[\ln y_+ + C(v_+)] + O(y_+^{-\alpha}), \quad y_+ \longrightarrow \infty,$$

where $D(v_+, \mathrm{Pr})$ is a certain function. Relation (3.4) for $v_+ = 0$ must coincide with Eq. (2.4). Therefore, $D(0, \mathrm{Pr}) = C_0 - B(\mathrm{Pr})$.

Relation (3.3) well describes the experimental velocity profiles with injection and suction (see, e.g., [5]). It is difficult to test similarity law (3.4) by analyzing the temperature profile, because experimental data on the temperature profile in the boundary layer on a permeable surface are virtually absent.

According to Eq. (1.8), the turbulent Prandtl number in the logarithmic region is independent of the transverse velocity on the wall, which is corroborated by experimental observations [6].

4. Applying the method of matched asymptotic expansions [7] to Eq. (3.2), we now analyze the asymptotic structure of the velocity and temperature profiles for large v_+ values. In this case, four characteristic subregions are formed in the wall region.

Subregion I, where $Y = O(1)$, adjoins the wall. Here, the turbulent shear stress can be disregarded in Eq. (3.2), and the leading term of the solution coincides with that for the pure laminar flow:

$$w = \frac{2}{v_+}e^{\frac{Y}{2}} + O(v_+^{-4}),$$
$$\ln(1 + v_+\theta_+) = \Pr Y + O(v_+^{-3}). \tag{4.1}$$

The solution in subregion II lying above is sought in the form

$$Y = M + Y_2, \quad w = \frac{W_2(Y_2)}{M} + \ldots,$$
$$Y_2 = O(1), \quad M \longrightarrow \infty. \tag{4.2}$$

The substitution of Eq. (4.2) into Eq. (3.2) and the passage to the limit $M \longrightarrow \infty$ and $Y_2 = O(1)$ provide

$$\left(\frac{dW_2}{dY_2}\right)^2 S(\mathrm{R}, \infty) + \frac{2}{W_2}\frac{dW_2}{dY_2} = 1, \quad \mathrm{R} = \frac{W_2}{2}\frac{dW_2}{dY_2}. \tag{4.3}$$

Thus, the turbulent and laminar components of shear stress in this subregion are of the same order of magnitude. Asymptotically matching expansions (4.1) and (4.2), we determine the initial condition for Eq. (4.3) and the parameter M:

$$W_2 \longrightarrow 2e^{\frac{Y_2}{2}}, \quad Y_2 \longrightarrow -\infty; \quad Me^{\frac{M}{2}} = v_+. \tag{4.4}$$

From Eq. (4.3) and with account of initial condition (4.4), we obtain the solution in the parametric form

$$Y_2 = \ln\mathrm{R} + \mathrm{R}S(\mathrm{R}, \infty) + \int_0^{\mathrm{R}} S(\mathrm{R}, \infty)d\mathrm{R},$$
$$W_2 = 2\sqrt{\mathrm{R}^2 S(\mathrm{R}, \infty) + \mathrm{R}}, \quad 0 < \mathrm{R} < \infty. \tag{4.5}$$

The temperature profile in subregion II is written as

$$\ln(1 + v_+\theta_+)$$
$$= \Pr Y^* + \int_{Y^* - M}^{Y_2} \frac{\Pr dY_2}{1 + \Pr\mathrm{R}\,T(\mathrm{R}, \Pr\mathrm{R}, \infty)}, \tag{4.6}$$
$$Y^* = O(1).$$

Substituting Eq. (4.5) into integral (4.6) and passing to the limit $M \longrightarrow \infty$, we arrive at the relation

$$\ln(1 + v_+\theta_+)$$
$$= \Pr M + \Pr\int_0^{\mathrm{R}} \frac{\mathrm{R}dS(\mathrm{R}, \infty) + 2S(\mathrm{R}, \infty)d\mathrm{R}}{1 + \Pr\mathrm{R}\,T(\mathrm{R}, \Pr\mathrm{R}, \infty)}$$
$$+ \Pr\int_1^{\mathrm{R}} \frac{d\mathrm{R}}{\mathrm{R}[1 + \Pr\mathrm{R}\,T(\mathrm{R}, \Pr\mathrm{R}, \infty)]}$$
$$- \Pr^2\int_0^1 \frac{T(\mathrm{R}, \Pr\mathrm{R}, \infty)d\mathrm{R}}{1 + \Pr\mathrm{R}\,T(\mathrm{R}, \Pr\mathrm{R}, \infty)}.$$

Therefore, letting R go to ∞, we obtain

$$\ln(1 + v_+\theta_+) = 2b\ln Y_2 + \Pr M + a_2(\Pr) + \ldots \tag{4.7}$$

for the outer boundary of subregion II, where

$$b = \frac{S(\infty, \infty)}{T(\infty, \infty, \infty)}, \quad Y_2 \longrightarrow \infty$$

and the function $a_2(\Pr)$ can be expressed in terms of integrals of S and T.

In subregion III,

$$Y = M + \sqrt{M}Y_3, \quad w = \frac{W_3(Y_3)}{\sqrt{M}} + \ldots,$$
$$\frac{1}{Y_3} = O(1), \quad Y_3 O(1).$$

After the passage to the limit $M \longrightarrow \infty$, $\frac{1}{Y_3} = O(1)$, and $Y_3 = O(1)$, only the turbulent component of the shear stress retains in Eq. (3.2):

$$\left(\frac{dW_3}{dY_3}\right)^2 S(\infty, \beta) = 1, \quad \beta = \left(\frac{2}{W_3}\frac{dY_3}{dW_3}\right)^2. \tag{4.8}$$

The solution that satisfies Eq. (4.8) and matches the solution in subregion II has the form

$$Y_3 = \frac{S(\infty, \beta)}{\sqrt{\beta}} + \int_\beta^\infty \frac{S(\infty, \beta)d\beta}{2\beta^{3/2}},$$
$$W_3 = 2\sqrt{\frac{S(\infty, \beta)}{\beta}}, \quad 0 < \beta < \infty. \tag{4.9}$$

In subregion III, the integral

$$I_3 = \int_{Y_2/\sqrt{M}}^{Y_3} \frac{\sqrt{\beta}dY_3}{T(\infty, \infty, \beta)}$$

is added to Eq. (4.6) for the temperature profile. Substituting Eq. (4.9) into this integral and passing to the limit

$M \to \infty$, we arrive at the relation

$$I_3 = b[\ln M - 2\ln Y_2 + 2\ln(2S(\infty, \infty))]$$

$$+ \int_\beta^1 \frac{S(\infty, \beta)d\beta}{\beta T(\infty, \infty, \beta)} - \int_\beta^\infty \frac{dS(\infty, \beta)}{T(\infty, \infty, \beta)}$$

$$+ \int_1^\infty \frac{[S(\infty, \beta) - bT(\infty, \infty, \beta)]d\beta}{\beta T(\infty, \infty, \beta)}.$$

Summing this expression with asymptotic function (4.7) and passing to the limit $\beta \longrightarrow 0$, we arrive at the relation

$$\ln(1 + \nu_+\theta_+) = 2\mathrm{Pr}_t \ln Y_3 + \mathrm{Pr}M + b\ln M$$
$$+ a_2(\mathrm{Pr}) + a_3 + \ldots, \quad Y_3 \longrightarrow \infty, \tag{4.10}$$

for the outer boundary of subregion III. Here, the constant a_3 is also expressed in terms of integrals of functions S and T.

In outer subregion IV,

$$Y = MY_4, \quad w = W_4(Y_4) + \ldots, \quad \frac{1}{Y_4} = O(1),$$
$$\left(\frac{dW_4}{d\ln Y_4}\right)^2 S(\infty, 0) = 1. \tag{4.11}$$

The solution that satisfies Eq. (4.11) and matches the solution in subregion III has the form

$$W_4 = \frac{1}{\kappa}\ln Y_4. \tag{4.12}$$

Comparing Eqs. (4.12) and (3.3), we obtain the asymptotic representation

$$C(\nu_+) = \frac{M}{2} + \ldots, \quad \nu_+ \longrightarrow \infty, \quad M + 2\ln M = 2\ln \nu_+$$

of the function $C(\nu_+)$.

To determine the temperature profile in outer subregion IV, asymptotic representation (4.10) must be complemented by the integral

$$I_4 = \int_{1 + Y_3/\sqrt{M}}^{Y_4} \frac{2\mathrm{Pr}_t dY_4}{Y_4^2 \ln Y_4}.$$

As a result, we obtain the expression

$$\ln(1 + \nu_+\theta_+) = 2\mathrm{Pr}_t \ln\ln Y_4 + \mathrm{Pr}M$$
$$+ (b + \mathrm{Pr}_t)\ln M + a_2(\mathrm{Pr}) + a_3.$$

Comparing this expression with Eq. (3.4), we arrive at the asymptotic representation

$$D(\nu_+, \mathrm{Pr})$$
$$= \exp\left\{-\frac{1}{2\mathrm{Pr}_t}[\mathrm{Pr}M + (\mathrm{Pr}_t + b)\ln M + a_2(\mathrm{Pr}) + a_3]\right\}$$
$$- \frac{2\kappa}{M}e^{-\frac{M}{2}} + \ldots, \quad \nu_+ \longrightarrow \infty.$$

Therefore, this function tends to zero for large ν_+ values.

Thus, we consider the problem formulation based on dynamic equations, the usual assumption that the flow in the wall region is independent of the external parameters of the boundary layer, and the requirement of the continuity of functions S and T specifying the turbulent shear stress and temperature flux. Without any hypothesis about the particular mechanisms of turbulent exchange, we obtain similarity laws for the velocity and temperature profiles and asymptotic representations of the universal functions C and D appearing in these laws.

REFERENCES

1. C. B. Millikan, in *Proceedings of 5th International Congress on Applied Mechanics* (Wiley, New York, 1939), p. 386.
2. B. A. Kader and A. M. Yaglom, Itogi Nauki Tekh., Ser. Mekh. Zhidk. Gaza **15**, 81 (1980).
3. T. N. Stevenson, CoA Rep. Aero., No. 166 (1963); R. J. Aeronaut. Soc. **68** (642), 431 (1964).
4. T. N. Stevenson, AIAA J. **6** (3), 533 (1968).
5. I. I. Vigdorovich, Izv. Akad. Nauk, Ser. Mekh. Zhidk. Gaza, No. 4, 78 (2002).
6. R. L. Simpson, R. J. Moffat, and D. G. Whitten, Int. J. Heat Mass Transf. **13** (1), 125 (1970).
7. M. D. Van Dyke, *Perturbation Methods in Fluid Mechanics* (Academic, New York, 1964; Mir, Moscow, 1967).

Translated by R. Tyapaev

Doklady Physics, Vol. 48, No. 9, 2003, pp. 533–536. Translated from Doklady Akademii Nauk, Vol. 392, No. 3, 2003, pp. 346–349.
Original Russian Text Copyright © 2003 by Chernyshov.

MECHANICS

Dynamic Problems for an Elastic Triangular Bar under Plane Deformation

A. D. Chernyshov

Presented by Academician E.I. Shemyakin June 4, 2003

Received June 5, 2003

Using a special ξ-variable procedure, two exact solutions of the problem of vibrations of an elastic bar with a triangular cross-section under plane deformation were obtained in the closed form. In the first case, the normal displacement and the shear stress were set at the bar boundary. In the second case, the tangential displacement and the normal stress were given. The resonance frequencies were found, and the displacement field, as well as volume and shear strains, was analyzed.

At present, only several exact solutions have been obtained for 2D dynamic problems of the theory of elasticity for unlimited regions. For limited regions, the number of exact solutions are even fewer. Here, we point to the solutions obtained in [1, 2]. Functionally invariant solutions were considered in [3], where the Smirnov–Sobolev procedure was used. The Laplace transform and the multiple Fourier coordinate transform, as well as the Kupradze fundamental solution, were used in [4]. Below, the exact solutions were obtained using special ξ variables, which were previously used in the dynamic problem of the motion of a viscous fluid in a triangular pipe [5].

For plane deformation, we write the equations of motion for elastic-medium points in the Lagrange variables [1]:

$$\begin{aligned}(\lambda + 2\mu)u_{xx} + (\lambda + \mu)v_{xy} + \mu u_{yy} + \tilde{G}_1 &= \rho u_{tt},\\ (\lambda + 2\mu)v_{yy} + (\lambda + \mu)u_{xy} + \mu v_{xx} + \tilde{G}_2 &= \rho u_{tt}.\end{aligned} \qquad (1)$$

We consider the problem of harmonic vibrations without initial conditions when the boundary conditions at the bar boundary Γ, whose cross section Ω is a regular triangle with the height h, are set in the form

$$u_n|_\Gamma = u_0 \cos\omega t, \quad \tau_n|_\Gamma = \tau_0 \cos\omega t, \qquad (2)$$

where u_n is the normal displacement and τ_n is the shear stress at the bar boundary. The solution of the problem is sought in the form

$$u = U(x, y)\cos\omega t, \quad v = V(x, y)\cos\omega t. \qquad (3)$$

Substituting Eqs. (3) into Eqs. (1) and (2), we arrive at the following problem for the amplitudes U and V:

$$\begin{aligned}(\lambda + 2\mu)U_{xx} + (\lambda + \mu)V_{xy} + \mu U_{yy} + \rho\omega^2 U &= 0,\\ (\lambda + 2\mu)V_{yy} + (\lambda + \mu)U_{xy} + \mu V_{xx} + \rho\omega^2 V &= 0,\end{aligned} \qquad (4)$$

$$(Un_x + Vn_y)_\Gamma = u_0, \quad \gamma_n|_\Gamma = \frac{\tau_0}{2\mu}, \qquad (5)$$

where (n_x, n_y) is the inward unit normal to the boundary Γ and γ_n is the shear strain for points of this boundary. Hereafter, the quantities U and V are called displacements, although the true displacements can be obtained by multiplying them by $\cos\omega t$. The same terms are used for strains and stresses. In this formulation, it is possible to find exact solutions. To this end, we consider an auxiliary problem. Let U and V depend only on the coordinate x. In this case, the partial solutions of set (4) have the form

$$\begin{aligned}&U_1 = \cos ax, \quad U_2 = \sin ax,\\ &V_1 = \cos bx, \quad V_2 = \sin bx,\\ &a^2 = \frac{\rho\omega^2}{\lambda + 2\mu}, \quad b^2 = \frac{\rho\omega^2}{\mu}.\end{aligned} \qquad (6)$$

We introduce the three variables

$$\xi_i = (\mathbf{r} - \mathbf{r}_i)\mathbf{n}_i, \quad i = 1, 2, 3. \qquad (7)$$

Here, $\mathbf{n}_i$ are the inward unit normals to the sides of the triangle Ω, $\mathbf{r}_i$ are the radius vectors of its vertices, and $\mathbf{r}$ is the radius vector of an arbitrary point in the region Ω. The variables ξ_i and the normals $\mathbf{n}_i$ have the following properties, which will be often used:

$$\mathbf{n}_1 + \mathbf{n}_2 + \mathbf{n}_3 = 0, \quad \mathbf{n}_1\mathbf{n}_2 = \mathbf{n}_1\mathbf{n}_3 = \mathbf{n}_2\mathbf{n}_3 = -\frac{1}{2}; \qquad (8)$$

$$\mathbf{n}_1 \times \mathbf{n}_2 = \mathbf{n}_2 \times \mathbf{n}_3 = \mathbf{n}_3 \times \mathbf{n}_1 = \frac{\sqrt{3}}{2}; \qquad (9)$$

Voronezh State Technological Academy,
Voronezh, 394000 Russia

$$\xi_1 + \xi_2 + \xi_3 = h.$$

$$\text{For } F = F(\xi_i),\quad F_x = F'(\xi_i)n_{ix},$$

$$F_y = F'(\xi_i)n_{iy}, \tag{10}$$

$$F_{xx} = F''(\xi_i)n_{ix}^2,\quad F_{xy} = F''(\xi_i)n_{ix}n_{iy},$$

$$F_{yy} = F''(\xi_i)n_{iy}^2.$$

We denote $n_{ix} = \cos\theta_i$ and $n_{iy} = \sin\theta_i$. In this case, θ_i is the angle between the normal $\mathbf{n}_i$ to the straight line $\xi_i = \text{const}$ and the x axis. Taking into account that the vector components (U, V) transform according to the known law under rotation and using Eqs. (6), we can write the following partial solution of set (4):

$$\begin{aligned} U = {} & (A\cos a\xi_1 + B\sin a\xi_1)n_{1x} \\ & + (A\cos a\xi_2 + B\sin a\xi_2)n_{2x} \\ & + (A\cos a\xi_3 + B\sin a\xi_3)n_{3x} \\ & - (C\cos b\xi_1 + D\sin b\xi_1)n_{1y} \\ & - (C\cos b\xi_2 + D\sin b\xi_2)n_{2y} \\ & - (C\cos b\xi_3 + D\sin b\xi_3)n_{3y}, \\ V = {} & (A\cos a\xi_1 + B\sin a\xi_1)n_{1y} \\ & + (A\cos a\xi_2 + B\sin a\xi_2)n_{2y} \\ & + (A\cos a\xi_3 + B\sin a\xi_3)n_{3y} \\ & + (C\cos b\xi_1 + D\sin b\xi_1)n_{1x} \\ & + (C\cos b\xi_2 + D\sin b\xi_2)n_{2x} \\ & + (C\cos b\xi_3 + D\sin b\xi_3)n_{3x}. \end{aligned} \tag{11}$$

Indeed, the substitution of Eqs. (11) into Eqs. (4) yields the identities. The variables ξ_i enter equivalently into the expressions for U and V, while the constants A, B, C, and D can be found from the two boundary conditions specified by Eqs. (5). Since solution (11) depends identically on the variables ξ_1, ξ_2, and ξ_3, conditions (5) on any side of the triangle lead to the same result. For definiteness, we apply the first boundary condition from (5) to the side $\xi_3 = 0$. In this case, we replace $\xi_2 = h - \xi_1$ in view of properties (10):

$$\begin{aligned} u_0 = {} & (Un_{3x} + Vn_{3y})_{\xi_3 = 0} \\ = {} & (A\cos a\xi_1 + B\sin a\xi_1)n_{1x}n_{3x} \\ & + [A\cos a(h-\xi_1) + B\sin a(h-\xi_1)]n_{2x}n_{3x} \\ & + An_{3x}^2 - Cn_{3x}n_{3y} - (C\cos b\xi_1 + D\sin b\xi_1)n_{1y}n_{3x} \\ & - [C\cos b(h-\xi_1) + D\sin b(h-\xi_1)]n_{2x}n_{3x} \\ & + (A\cos a\xi_1 + B\sin a\xi_1)n_{1y}n_{3y} \\ & + [A\cos a(h-\xi_1) + B\sin a(h-\xi_1)]n_{2x}n_{3y} \\ & + An_{3y}^2 + Cn_{3x}n_{3y} + (C\cos b\xi_1 + D\sin b\xi_1)n_{1x}n_{3y} \\ & + [C\cos b(h-\xi_1) + D\sin b(h-\xi_1)]n_{2x}n_{3y}. \end{aligned} \tag{12}$$

The left-hand side of this equality is independent of ξ_1; therefore, the coefficients of cosines and sines on the right-hand side must be equal to zero:

$$\begin{aligned} & An_{1x}n_{3x} + (A\cos ah + B\sin ah)n_{2x}n_{3x} + An_{1y}n_{3y} \\ & \quad + (A\cos ah + B\sin ah)n_{2y}n_{3y} = 0, \\ & Bn_{1x}n_{3x} + (A\sin ah - B\cos ah)n_{2x}n_{3x} + Bn_{1y}n_{3y} \\ & \quad + (A\sin ah - B\cos ah)n_{2y}n_{3y} = 0, \\ & -Cn_{1y}n_{3x} - (C\cos bh + D\sin bh)n_{2y}n_{3x} \\ & \quad + Cn_{1x}n_{3y} + (C\cos bh + D\sin bh)n_{2x}n_{3y} = 0, \\ & -(C\sin bh - D\cos bh)n_{2y}n_{3x} + Dn_{1x}n_{3y} \\ & \quad - Dn_{1y}n_{3x} + (C\sin bh - D\cos bh)n_{2x}n_{3y} = 0. \end{aligned} \tag{13}$$

In view of properties (8) and (9), set (13) is simplified as

$$\begin{aligned} A(1 + \cos ah) + B\sin ah &= 0, \\ B(1 - \cos ah) + A\sin ah &= 0, \\ C(1 - \cos bh) - D\sin bh &= 0, \\ D(1 + \cos bh) - C\sin bh &= 0. \end{aligned}$$

Therefore, we find

$$\begin{aligned} A &= A_0\sin a\frac{h}{2},\quad B = -A_0\cos a\frac{h}{2}, \\ C &= C_0\cos b\frac{h}{2},\quad D = C_0\sin b\frac{h}{2}. \end{aligned} \tag{14}$$

Now, from Eqs. (12) and (14) we obtain

$$A_0 = u_0\left(\sin a\frac{h}{2}\right)^{-1},\quad A = u_0,\quad B = -u_0\cot a\frac{h}{2}. \tag{15}$$

Another unknown constant C_0 is determined using the second boundary condition from Eqs. (5) for the shear strain. On the sides of the triangle, the normal displacement component $u_{n_3} = u_0$ is constant. Therefore, the shear γ is determined from the expression

$$2\gamma|_{\xi_3 = 0} = \left(\frac{\partial u_{\tau_3}}{\partial n_3} + \frac{\partial u_{n_3}}{\partial \tau_3}\right)_{\xi_3 = 0} = \left.\frac{\partial u_{\tau_3}}{\partial n_3}\right|_{\xi_3 = 0}. \tag{16}$$

We specify the unit tangential vectors $\boldsymbol{\tau}_i$ on the sides of the triangle in terms of the components of normals $\mathbf{n}_i$: $\boldsymbol{\tau}_i = (n_{iy}, -n_{ix})$. In this case, the tangential displacement u_{τ_3} is determined as

$$u_{\tau_3} = U\tau_{3x} + V\tau_{3y} = -Vn_{3x} + Un_{3y}.$$

Substituting u_{τ_3} into Eq. (16), we find

$$C_0 = -\tau_0\left(\mu b \sin b\frac{h}{2}\right)^{-1}. \qquad (17)$$

After simplifications by means of Eqs. (14) and (15), solution (11) of the problem reduces to the form

$$\begin{aligned}
U = {} & A_0\left[n_{1x}\sin a\left(\frac{h}{2}-\xi_1\right)+n_{2x}\sin a\left(\frac{h}{2}-\xi_2\right)\right. \\
& \left.+ n_{3x}\sin a\left(\frac{h}{2}-\xi_3\right)\right] - C_0\left[n_{1y}\cos b\left(\frac{h}{2}-\xi_1\right)\right. \\
& \left.+ n_{2y}\cos b\left(\frac{h}{2}-\xi_2\right)+n_{3y}\cos b\left(\frac{h}{2}-\xi_3\right)\right], \\
V = {} & A_0\left[n_{1y}\sin a\left(\frac{h}{2}-\xi_1\right)+n_{2y}\sin a\left(\frac{h}{2}-\xi_2\right)\right. \\
& \left.+ n_{3y}\sin a\left(\frac{h}{2}-\xi_3\right)\right] + C_0\left[n_{1x}\cos b\left(\frac{h}{2}-\xi_1\right)\right. \\
& \left.+ n_{2x}\cos b\left(\frac{h}{2}-\xi_2\right)+n_{3x}\cos b\left(\frac{h}{2}-\xi_3\right)\right], \\
A_0 = {} & u_0\left(\sin a\frac{h}{2}\right)^{-1}, \quad C_0 = -\tau_0\left(\mu b\sin b\frac{h}{2}\right)^{-1}, \\
A_0 = {} & u_0\left(\sin a\frac{h}{2}\right)^{-1}, \quad C_0 = -\tau_0\left(\mu b\sin b\frac{h}{2}\right)^{-1}.
\end{aligned} \qquad (18)$$

The resonance frequencies ω^* can be found from the conditions $\sin\frac{ah}{2} = 0$ and $\sin\frac{bh}{2} = 0$, under which solution (18) does not exist:

$$\omega_1^* = 2k\frac{\pi}{h}\sqrt{\frac{\lambda+2\mu}{\rho}}, \quad \omega_2^* = 2k\frac{\pi}{h}\sqrt{\frac{\mu}{\rho}}, \quad k = 1, 2, \ldots. \qquad (19)$$

Using the found displacements, we calculate strains and stresses:

$$\begin{aligned}
e_x = U_x = {} & -aA_0\left[n_{1x}^2\cos a\left(\frac{h}{2}-\xi_1\right)+n_{2x}^2\cos a\left(\frac{h}{2}-\xi_2\right)\right. \\
& \left.+ n_{3x}^2\cos a\left(\frac{h}{2}-\xi_3\right)\right] - bC_0\left[n_{1x}n_{1y}\sin b\left(\frac{h}{2}-\xi_1\right)\right. \\
& \left.+ n_{2x}n_{2y}\sin b\left(\frac{h}{2}-\xi_2\right)+n_{3x}n_{3y}\sin b\left(\frac{h}{2}-\xi_3\right)\right], \\
e_y = V_y = {} & -aA_0\left[n_{1y}^2\cos a\left(\frac{h}{2}-\xi_1\right)+n_{2y}^2\cos a\left(\frac{h}{2}-\xi_2\right)\right. \\
& \left.+ n_{3y}^2\cos a\left(\frac{h}{2}-\xi_3\right)\right] + bC_0\left[n_{1x}n_{1y}\sin b\left(\frac{h}{2}-\xi_1\right)\right. \\
& \left.+ n_{2x}n_{2y}\sin b\left(\frac{h}{2}-\xi_2\right)+n_{3x}n_{3y}\sin b\left(\frac{h}{2}-\xi_3\right)\right], \\
e_{xy} = {} & \frac{1}{2}(U_y+V_x) = -aA_0\left[n_{1x}n_{1y}\cos a\left(\frac{h}{2}-\xi_1\right)\right. \\
& \left.+ n_{2x}n_{2y}\cos a\left(\frac{h}{2}-\xi_2\right)+n_{3x}n_{3y}\cos a\left(\frac{h}{2}-\xi_3\right)\right] \\
& + \frac{1}{2}bC_0\left[(n_{1x}^2-n_{1y}^2)\sin b\left(\frac{h}{2}-\xi_1\right)\right. \\
& \left.+ (n_{2x}^2-n_{2y}^2)\sin b\left(\frac{h}{2}-\xi_2\right)+(n_{3x}^2-n_{3y}^2)\sin b\left(\frac{h}{2}-\xi_3\right)\right], \\
& \sigma_{xy} = 2\mu e_{xy}, \quad \sigma_x = (\lambda+2\mu)e_x+\lambda e_y, \\
& \sigma_y = (\lambda+2\mu)e_y+\lambda e_x.
\end{aligned} \qquad (20)$$

In particular, it follows from Eqs. (18) and (20) that the vertices of the triangle displace along the respective heights by $2u_0$, and the displacements are equal to zero, i.e., $U = V = 0$, at the triangle center. The volume compression $(e_x + e_y)$ takes the characteristic magnitudes

$$(e_x+e_y) = -3aA_0\cos a\frac{h}{2}$$

at the vertices of the triangle,

$$(e_x+e_y) = -3aA_0\cos a\frac{h}{6}$$

at its center, and

$$(e_x+e_y) = -aA_0\left(2+\cos a\frac{h}{2}\right)$$

at the middles of its sides.

Problem (1) of vibrations of an elastic triangular bar has one more exact solution for the boundary conditions

$$u_\tau|_\Gamma = u_{\tau 0}\cos\omega t, \quad \sigma_n|_\Gamma = \sigma_{n0}\cos\omega t. \qquad (21)$$

Making the same manipulations as when obtaining solution (18), we arrive at the exact solution in the form

$$\begin{aligned}
U = {} & A_0\left[n_{1x}\cos a\left(\frac{h}{2}-\xi_1\right)+n_{2x}\cos a\left(\frac{h}{2}-\xi_2\right)\right. \\
& \left.+ n_{3x}\cos a\left(\frac{h}{2}-\xi_3\right)\right] - C_0\left[n_{1y}\sin b\left(\frac{h}{2}-\xi_1\right)\right. \\
& \left.+ n_{2y}\sin b\left(\frac{h}{2}-\xi_2\right)+n_{3y}\sin b\left(\frac{h}{2}-\xi_3\right)\right], \\
V = {} & A_0\left[n_{1y}\cos a\left(\frac{h}{2}-\xi_1\right)+n_{2y}\cos a\left(\frac{h}{2}-\xi_2\right)\right.
\end{aligned} \qquad (22)$$

$$+ n_{3y}\cos a\left(\frac{h}{2}-\xi_3\right)\Big] + C_0\Big[n_{1x}\sin b\left(\frac{h}{2}-\xi_1\right)$$

$$+ n_{2x}\sin b\left(\frac{h}{2}-\xi_2\right) + n_{3x}\sin b\left(\frac{h}{2}-\xi_3\right)\Big].$$

The constants A_0 and C_0 are determined from boundary conditions (21):

$$A_0 = \sigma_{n0}\left[a(\lambda+2\mu)\sin a\frac{h}{2}\right]^{-1},$$
$$C_0 = u_{\tau 0}\left(\sin b\frac{h}{2}\right)^{-1}. \qquad (23)$$

The resonance frequencies ω^* found from Eqs. (23) have form (19), as in the preceding problem. Using Eqs. (22), we calculate the strain-tensor components:

$$e_x = aA_0\Big[n_{1x}^2\sin a\left(\frac{h}{2}-\xi_1\right) + n_{2x}^2\sin a\left(\frac{h}{2}-\xi_2\right)$$

$$+ n_{3x}^2\sin a\left(\frac{h}{2}-\xi_3\right)\Big] + bC_0\Big[n_{1x}n_{1y}\cos b\left(\frac{h}{2}-\xi_1\right)$$

$$+ n_{2x}n_{2y}\cos b\left(\frac{h}{2}-\xi_2\right) + n_{3x}n_{3y}\cos b\left(\frac{h}{2}-\xi_3\right)\Big],$$

$$e_y = aA_0\Big[n_{1y}^2\sin a\left(\frac{h}{2}-\xi_1\right) + n_{2y}^2\sin a\left(\frac{h}{2}-\xi_2\right)$$

$$+ n_{3y}^2\sin a\left(\frac{h}{2}-\xi_3\right)\Big] - bC_0\Big[n_{1x}n_{1y}\cos b\left(\frac{h}{2}-\xi_1\right) \qquad (24)$$

$$+ n_{2x}n_{2y}\cos b\left(\frac{h}{2}-\xi_2\right) + n_{3x}n_{3y}\cos b\left(\frac{h}{2}-\xi_3\right)\Big],$$

$$e_{xy} = aA_0\Big[n_{1x}n_{1y}\sin a\left(\frac{h}{2}-\xi_1\right) + n_{2x}n_{2y}\sin a\left(\frac{h}{2}-\xi_2\right)$$

$$+ n_{3x}n_{3y}\sin a\left(\frac{h}{2}-\xi_3\right)\Big] + \frac{1}{2}bC_0\Big[(n_{1y}^2-n_{1x}^2)\cos b\left(\frac{h}{2}-\xi_1\right)$$

$$+ (n_{2x}^2-n_{2y}^2)\cos b\left(\frac{h}{2}-\xi_2\right) + (n_{3y}^2-n_{3x}^2)\cos b\left(\frac{h}{2}-\xi_3\right)\Big].$$

In this problem, the vertices of the triangle displace in parallel to the opposite sides by $2u_{\tau 0}$, and the displacements are equal to zero, i.e., $U = V = 0$, at its center. The three-dimensional compression at the vertices and at the sides of the triangle is identical and equal to

$$(e_x + e_y) = aA_0\sin a\frac{h}{2},$$

while it is three times as large at its center.

REFERENCES

1. E. I. Shemyakin, *Introduction to the Theory of Elasticity* (Mosk. Gos. Univ., Moscow, 1993).
2. J. D. Cole and J. H. Huth, J. Appl. Mech. **25**, 433 (1958).
3. I. O. Osipov, Izv. Akad. Nauk, Mekh. Tverd. Tela, No. 3, 78 (2002).
4. G. Yu. Ermolenko and S. A. Yushkov, Prikl. Mat. Mekh. **62** (4), 715 (1998).
5. A. D. Chernyshov, Izv. Akad. Nauk, Ser. Mekh. Zhidk. Gaza, No. 5, 199 (1998).

Translated by V. Bukhanov